Calculation of static and dynamical properties of giant magnetic molecules using DMRG

Dissertation

zur Erlangung des Grades eines
Doktors der Naturwissenschaften

vorgelegt von

Jörg Ummethum

im Juli 2012

Gutachter:
Prof. Dr. Jürgen Schnack
Prof. Dr. Peter Reimann

Printed on permanent paper ∞ ISO 9706

Contents

1. Introduction

In 1993, Sessoli *et al.* discovered that the molecule Mn_{12} shows a slow relaxation of the magnetization and a hysteresis loop of molecular origin at sufficiently low temperatures [1]. This discovery gave rise to the hope that it might be possible to use such molecules for high-density information storage devices and led to an increased interest in the investigation of magnetic molecules [2]. Magnetic molecules have already been investigated before the 1990s, but to this day Mn_{12} remains the most famous molecule [3]. Mn_{12} is a so-called single-molecule magnet. Antiferromagnetic molecules with non-magnetic ground states are another class of magnetic molecules being the subject of extensive theoretical and experimental investigations, and there exist some highly symmetric and truly giant molecules such as $Mo_{72}Fe_{30}$ [4], which has a diameter of about 2.5 nm and is thus called a "mesoscopic system". Mesoscopic magnetic molecules offer the possibility to study the region between microscopic and macroscopic systems.

Magnetic molecules are in most cases modeled using simple spin Hamiltonians. The calculation of thermodynamic expectation values or energy spectra of spin Hamiltonians is often hindered by a too large Hilbert space dimension which grows exponentially with the number of spins. Analytical solutions are only possible for very small or few special systems so that numerical methods or (semi-)classical approximations are often necessary. Several quasi-exact numerical methods exist that can be applied to spin Hamiltonians. However, large antiferromagnetic and geometrically frustrated magnetic molecules such as $Mo_{72}Fe_{30}$ ($N = 30$ spins with $s = 5/2$) are extremely challenging since the prohibitively large Hilbert space excludes exact diagonalization methods and the geometrical frustration leads to severe problems for Quantum Monte Carlo methods.

In this work, density matrix renormalization group (DMRG) techniques [5, 6] are applied to very large spin systems such as $Mo_{72}Fe_{30}$. These advanced numerical techniques rely on an efficient truncation of the Hilbert space and allow us to obtain information on the low-energy spectrum that are currently not accessible by other methods. Although DMRG can in principle be applied to arbitrary spin systems, it is most accurate for one-dimensional systems and for the calculation of ground state properties. In the field of one-dimensional or quasi-one-dimensional systems, DMRG has become a standard numerical technique. However, this method is only very rarely applied to magnetic molecules. Since in most magnetic molecules the spins are not arranged one-dimensionally, it is a priori not clear how accurate DMRG

is for these systems and the accuracy needs to be checked carefully. We use DMRG and DDMRG (dynamical DMRG [7, 8]) to calculate static and dynamical properties of icosidodecahedral spin systems (including $Mo_{72}Fe_{30}$ with a Hilbert space dimension of the order of 10^{23}) and the ring molecule Fe_{18} [9, 10] (Hilbert space dimension of the order of 10^{14}) based on the full Heisenberg Hamiltonian. Up to now these systems have mostly been treated with classical or semi-classical methods such as spin-wave theory [11, 12] or classical Monte Carlo [4, 13–15], or on the basis of simplified Hamiltonians which result from the so-called rotational band approximation [4, 10, 16–18]. An exception is the icosidodecahedron with $s = 1/2$ which can still be treated using quasi-exact Lanczos techniques [19–22]. Quantum Monte Carlo calculations on the icosidodecahedron can only be performed at high temperatures due to the negative-sign problem [23, 24].

DMRG and DDMRG allow us to obtain detailed information on the low-energy spectrum and, moreover, yield transition matrix elements which are related to the simulation of inelastic neutron scattering (INS) spectra. We compare our data for the molecule Fe_{18} with experimental results [25], and for one parameter set we obtain a very good agreement between all theoretical and experimental data. In our calculations for the icosidodecahedral spin systems with spin quantum numbers up to $s = 5/2$ we focus on features that are typical for geometrically frustrated spin systems [26], and we study the transition to the classical (i.e., $s \to \infty$) regime. We furthermore test the accuracy of DMRG throughout this work.

This thesis is organized as follows: In chapter 2 an introduction to magnetic molecules and spin Hamiltonians is given. In chapter 3 the DMRG technique and the extension to calculate dynamical properties (DDMRG) are introduced, and the program that was developed for this thesis is described. In chapter 4 the (DMRG) results for antiferromagnetic icosidodecahedral systems are presented. We have focused on the calculation of zero-temperature magnetization curves for different spin quantum numbers and compare the results with the predictions of the classical (i.e., $s \to \infty$) and the rotational band approximation. Furthermore, the accuracy of the DMRG method when applied to these systems is tested and a dynamical correlation function for the $s = 1/2$ case is calculated using DDMRG. In chapter 5 we investigate antiferromagnetic spin rings with a focus on the 18-membered ring-like molecule Fe_{18}. We have used DMRG and DDMRG to calculate (zero-temperature) inelastic neutron scattering (INS) cross sections and magnetization curves for several parameter sets and compare the results with experimental data [25] for Fe_{18} in this chapter. We also check the accuracy of the rotational band approximation and spin-wave theory for spin rings (as a function of the number of spins and the individual spin quantum number) in that chapter. In chapter 6 the main results of this work are summarized and conclusions are drawn.

2. Theoretical background: Magnetic molecules and spin Hamiltonians

2.1. Introduction

Magnetic molecules are chemical compounds that contain several interacting magnetic ions, in most cases transition metal or rare earth ions. The number of magnetic centers in such a molecule can be as large as 84 [27]. However, the usual number is of the order of 10. Interactions within such a molecule are usually much stronger than interactions between different molecules so that measurements of magnetic properties performed on macroscopic samples, i.e., crystals or powders, reflect the properties of a single molecule [28]. Up to now, there exists an abundance of different magnetic molecules with a large variety of geometries such as dimers [29], icosidodecahedra [4], rings [10,30] (see Fig. 2.1), or tetrahedra [31]. Magnetic molecules show many fascinating effects, e.g., quantum steps of the magnetization [30], hysteresis loops [1], quantum tunneling of the magnetization [32], or quantum phase interference [10, 33]. Potential applications of magnetic molecules are, e.g., high-density information storage [2], quantum computing [34], or magnetic refrigeration [35,36].

Magnetic molecules are also interesting because they show in some aspects classical behavior and in some aspects quantum mechanical behavior so that the transition from the classical to the quantum world can be studied [4, 13, 37–39].

The magnetic properties of these molecules can in most cases be well described by spin Hamiltonians like the Heisenberg model with additional anisotropic terms and Zeeman interaction. In the following sections, an introduction to spin Hamiltonians and techniques to deal with such models is given.

2.2. Spin Hamiltonian of magnetic molecules

The magnetic properties of magnetic molecules originate in most cases from the spins of the unpaired electrons of the magnetic centers and very often the magnetic properties can be described by simple spin Hamiltonians [3]. A spin Hamiltonian is, of course, not an exact description of the entire system. From the theoretical point of view, the possibly complicated chemical structure is boiled down to a spin lattice, modeling the spins of the magnetic ions and interactions between them (cf. Fig. 2.1). The parameters of the spin Hamiltonian are usually not known and have

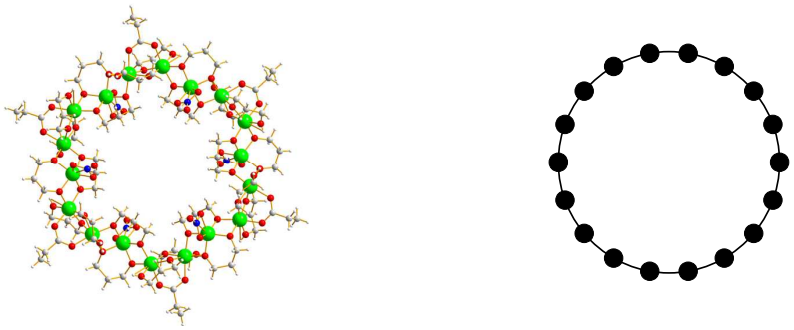

Figure 2.1.: Left: Fe_{18} molecule [25]. Right: Structure of the underlying spin system. The black circles denote the spins and the black lines the interaction paths.

to be determined by a comparison with experimental data. For a system containing N spins, the most general (zero-field) spin Hamiltonian that contains only two-spin terms can be written as [40, 41]

$$H_{\text{spin}} = H_{\text{Heisenberg}} + H_{\text{antisymmetric}} + H_{\text{anisotropic}} \,, \tag{2.1}$$

where

$$H_{\text{Heisenberg}} = \sum_{i<j} J_{ij} \vec{s}_i \cdot \vec{s}_j \tag{2.2}$$

denotes the isotropic Heisenberg Hamiltonian[1] with $J_{ij} = J_{ji}$ and

$$H_{\text{antisymmetric}} = \sum_{i,j} \vec{d}_{ij} \cdot (\vec{s}_i \times \vec{s}_j) \,, \tag{2.3}$$

$$H_{\text{anisotropic}} = \sum_{i,j} \vec{s}_i \cdot \mathbf{D}_{ij} \vec{s}_j \,. \tag{2.4}$$

$\vec{d}_{ij}$ is an antisymmetric vector and $\mathbf{D}_{ij}$ denotes a traceless symmetric tensor [40]. $\vec{s}_i$ denotes the vector operator for spin i. If $J_{ij} > 0$, the interaction between the spins $\vec{s}_i$ and $\vec{s}_j$ is antiferromagnetic and if $J_{ij} < 0$, the interaction is ferromagnetic. Higher-order interaction terms can be biquadratic terms [42] or higher-order anisotropy terms [3]. The microscopic origin of all these interaction terms is rather complicated (see, e.g., [40]) and will not be discussed further. However, the most obvious interaction term, the magnetic dipole-dipole interaction, very often plays no role and can in many cases be neglected. Instead, so-called "exchange interactions" (which lead to the terms $J_{ij}\vec{s}_i \cdot \vec{s}_j$) are dominant [3]. The ab initio calculation of

[1] When we use the term "Heisenberg system" in the following, we always mean a Heisenberg Hamiltonian which has the form (2.2).

the spin Hamiltonian parameters is very difficult and often not very accurate, see, e.g., Refs. [43, 44]. Spin Hamiltonians are usually used as an ansatz with unknown parameters. Experiences with similar systems, magneto-structural considerations, experimental data, and the symmetry of the molecule are used to choose a suitable ansatz. The magnetic parameters have to be determined by comparing with experimental data, such as inelastic neutron scattering spectra or magnetization curves.

In many cases, the dominant contributions to the spin Hamiltonian are the Heisenberg Hamiltonian and the $i = j$ terms of $H_{\text{anisotropic}}$. The coupling matrix J_{ij} often has a form with $J_{ij} = J$ if the spins at positions i and j are nearest neighbors and $J_{ij} = 0$ otherwise. In addition, for many systems a simple uniaxial single-ion anisotropy of the form $\sum_i D_i (s_i^z)^2$ is sufficient [3, 39], so that we arrive at the simplified Hamiltonian

$$H = H_{\text{Heisenberg}} + H_{\text{single-ion}} \,, \tag{2.5}$$

with

$$H_{\text{single-ion}} = \sum_i D_i (s_i^z)^2 \,. \tag{2.6}$$

Furthermore, for many systems the isotropic Heisenberg term dominates over the anisotropy term which can then be regarded as a perturbation [28, 39]. Typical values for J are of the order of 10 K (≈ 1 meV).

If a magnetic field $\vec{B}$ is applied to the molecule, an additional Zeeman interaction of the form

$$H_{\text{Zeeman}} = \sum_i g_i \mu_B \vec{B} \cdot \vec{s}_i \tag{2.7}$$

has to be added to the spin Hamiltonian. μ_B is the Bohr magneton and g_i denotes the spectroscopic splitting factors (usually ≈ 2) of the individual spins. In general, it is also possible to have a tensor instead of scalars g_i. This might be needed for the description of some systems [3]. However, we only use the simple version with g_i being a scalar and having the same value for all i.

In the following, we mainly use the simple Heisenberg Hamiltonian with an additional Zeeman term to calculate properties of magnetic systems. Furthermore, only antiferromagnetic systems ($J_{ij} \geq 0$) with all spins having the same quantum number $s_i = s$ are investigated. The influence of a small anisotropy is discussed in one of the later chapters (see Sec. 5.3.3).

2.2.1. Classical spin systems, bipartiteness, and geometrical frustration

In this subsection, some terms that are used in this and later chapters are introduced.

Although spins are quantum mechanical objects, the concept of *classical spin systems* is sometimes helpful and can serve as an approximation for the quantum mechanical problem. If we have a quantum mechanical Heisenberg Hamiltonian $H_{\text{Heisenberg}}$, the corresponding classical Hamilton function is obtained by replacing the vector operators $\vec{s}_i$ by classical vectors $\sqrt{s_i(s_i+1)}\vec{e}_i$, where $\vec{e}_i$ denotes a unit vector [45, 46]. The "classical limit" is approached for $s \to \infty$ and the classical system is expected to be a good approximation for large s values [13,47]. The scaling with $\sqrt{s(s+1)}$ is in some sense not optimal, since it leads to a wrong saturation magnetization for any finite s. The classical systems are in most cases much easier to handle than the quantum systems and standard numerical methods such as classical Monte Carlo can be used [13, 46].

We define a *bipartite* Heisenberg system in the following way: If it is possible to divide the lattice (defined by the coupling matrix J_{ij}) into two sublattices A and B such that $J_{i_A j_A} = 0$ for all spins on sublattice A, $J_{i_B j_B} = 0$ for all spins on sublattice B, and $J_{i_A j_B} \geq 0$ for spins on different sublattices, the system is called bipartite. Bipartiteness thus means that only spins on different sublattices interact. For bipartite systems the ground state of the classical Heisenberg system is very simple. Let N_b be the number of bonds and $J_{ij} = J$ for every bond. Then the ground state is a simple Néel state with all spin vectors on the same sublattice being parallel and the spin vectors on the different sublattices pointing in opposite directions. In this way it is possible to simultaneously minimize all bond energies, and the ground state energy is $E_0^{\text{classical}} = -JN_b s(s+1)$.

In the context of classical spin systems it is possible to introduce the term *geometrical frustration* [48, 49]. If we have a Heisenberg Hamiltonian with an interaction matrix J_{ij} and it is not possible to find a ground state for the corresponding classical system such that all bond energies are simultaneously minimized, the system is called frustrated. An example for geometrical frustration is the antiferromagnetic Heisenberg triangle with

$$H_{\text{triangle}} = J(\vec{s}_1 \cdot \vec{s}_2 + \vec{s}_2 \cdot \vec{s}_3 + \vec{s}_3 \cdot \vec{s}_1)\,. \tag{2.8}$$

It is clearly not possible to find a classical spin configuration that minimizes all bond energies (see Fig. 2.2), and hence the system is frustrated.

2.2.2. Basis and good quantum numbers

The comparison of theory (based on a spin Hamiltonian) to experiment (in the form of experimental data) requires in many cases the calculation of several or all eigenvalues and the corresponding eigenvectors of the Hamiltonian that is used as an ansatz. If an analytical calculation is not possible, one has to resort to approximations or numerical techniques. All these numerical techniques require the Hamiltonian to be represented by a matrix, and in order to represent it by a matrix, a basis has to be

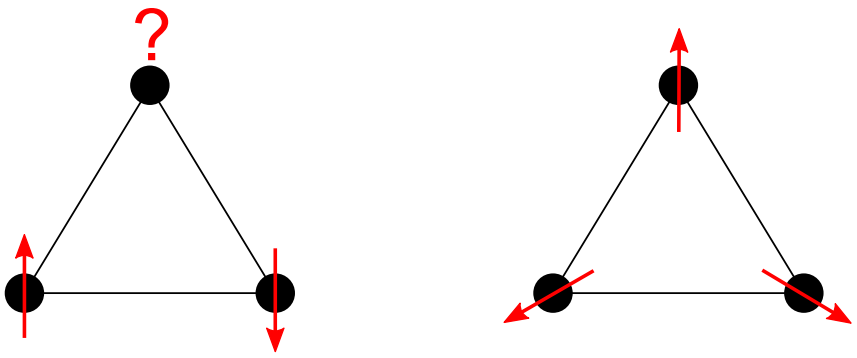

Figure 2.2.: Illustration of geometrical frustration for the antiferromagnetic Heisenberg triangle. Left: It is not possible to find a classical "up-down" configuration where all bond energies are minimized. Right: One of the possible classical ground state configurations. The angle between adjacent spins is 120° and thus the bond energy is not $-Js(s+1)$ as would be the case for an unfrustrated system [26].

chosen. The basis dimension for a cluster consisting of N spins (each having the spin quantum number s) is $(2s+1)^N$. The choice of basis depends on which symmetries shall be exploited. The Heisenberg Hamiltonian $H_{\text{Heisenberg}}$ is isotropic and has SU(2) symmetry. It commutes with all components of the total spin $\vec{S} \equiv \sum_i \vec{s}_i$, i.e., $[H, \vec{S}] = 0$. Furthermore, the square of the total spin, $\vec{S}^2$, commutes with the z component of the total spin, $S^z \equiv \sum_i s_i^z$, i.e., $[\vec{S}^2, S^z] = 0$ [50]. Therefore it is possible to find simultaneous eigenstates of $H_{\text{Heisenberg}}$, $\vec{S}^2$, and S^z. We denote the eigenstates of $\vec{S}^2$ and S^z as $|SM\alpha\rangle$, so that $\vec{S}^2|SM\alpha\rangle = S(S+1)|SM\alpha\rangle$ and $S^z|SM\alpha\rangle = M|SM\alpha\rangle$.[2] α denotes intermediate quantum numbers that result from the coupling of the individual spins to the total spin. This basis is called "vector-coupling basis" [51].

The matrix elements $\langle SM\alpha|H_{\text{Heisenberg}}|S'M'\alpha'\rangle$ are zero for $M \neq M'$ or $S \neq S'$ so that the representation of $H_{\text{Heisenberg}}$ in this basis has a special block form. Exploiting point-group symmetries leads to even smaller blocks [51]. The diagonalization can then be performed separately on each block. Having small effective matrix sizes is highly desirable for all numerical diagonalization techniques. Also, since the energy eigenvalues for Heisenberg systems are degenerate with respect to M [52], not all eigenspaces of S^z have to be considered. However, employing the vector-coupling basis is rather complicated, especially for numerical techniques such as DMRG (cf. [53, 54]).

Another possible basis is the simple product basis. If $\{|s_i m_i\rangle\}$ denotes the local basis for spin i with $s_i^z|s_i m_i\rangle = m_i|s_i m_i\rangle$, the product basis (for a system of N

[2] Natural units are used, i.e., $\hbar$ is absorbed into the respective units.

spins with each spin having quantum number s) is given by $\{|m_1 m_2 \dots m_N\rangle\} \equiv \{|s_1 m_1\rangle|s_2 m_2\rangle \cdots |s_N m_N\rangle\}$. These product states are not eigenstates of $\vec{S}^2$ but still eigenstates of S^z:

$$S^z|m_1 m_2 \dots m_N\rangle = M|m_1 m_2 \dots m_N\rangle \ , \quad M = \sum_i m_i \, . \tag{2.9}$$

If one sorts the product states according to their M quantum numbers, the Hamiltonian can be represented by a matrix in block form, where each block corresponds to a subspace with a specific M quantum number. Furthermore, if one rewrites the Heisenberg Hamiltonian as

$$H_{\text{Heisenberg}} = \sum_{i<j} J_{ij} \left\{ s_i^z s_j^z + \frac{1}{2}(s_i^+ s_j^- + s_i^- s_j^+) \right\} \ , \tag{2.10}$$

the matrix elements in the product basis can easily be calculated, since [50]

$$s_i^z|m_1 m_2 \dots m_N\rangle = m_i|m_1 m_2 \dots m_N\rangle \tag{2.11}$$

and

$$s_i^{+/-}|m_1 m_2 \dots m_N\rangle = \sqrt{s(s+1) - m_i(m_i \pm 1)}|m_1 m_2 \dots m_i \pm 1 \dots m_N\rangle \, . \tag{2.12}$$

For the vector-coupling basis, the calculation of matrix elements is more complicated and requires rewriting the Hamiltonian using irreducible tensor operators (ITOs) [51]. Also, point group symmetries such as cyclic invariance can more easily be exploited within the product basis [55]. The S quantum number of the resulting eigenvalues can very often still be deduced from the degeneracy with respect to M. The commutation relation $[H_{\text{Heisenberg}}, \vec{S}] = 0$ has the consequence that all energy eigenvalues are $(2S+1)$-fold degenerate with respect to M [52]. Every eigenstate has a representative in the $M = 0$ subspace (if Ns is an integer) so that the ground state can always be calculated in this subspace. This degeneracy is lifted if a Zeeman term is present. The Zeeman interaction Hamiltonian is diagonal in both bases and leads to an additional contribution of $g\mu_B BM$ to the energy of a state with quantum number M.

Once the matrix representation of the Hamiltonian has been set up, the goal is to calculate eigenvalues and eigenvectors. In the following some numerical methods to treat spin Hamiltonians are described.

The idea of *complete exact diagonalization* is to calculate all eigenvalues and – if needed – all eigenvectors of the Hamiltonian. This means that the matrix representation of the Hamiltonian, $\mathbf{H}$, has to be transformed to diagonal form. There exist standard algorithms and implementations that can be used for this task. If

symmetries are exploited, the Hamilton matrix **H** can be transformed into a block-diagonal form. These blocks can then be diagonalized separately. Since the Hilbert space dimension of a spin system with N spins with quantum number s is $(2s+1)^N$, it is clear that at some point complete exact diagonalization cannot be used anymore. Today, complex matrices with dimensions up to $\mathcal{O}(10^5)$ can be completely diagonalized [56]. However, such a calculation takes a very long time (of the order of days).

There also exist numerical methods such as the Lanczos algorithm [57] which allow for the calculation of several extremal eigenvalues and the corresponding eigenvectors. Since these methods are virtually numerically exact, they are also included in the class of the *exact diagonalization* methods. The great advantage of, e.g., the Lanczos method is, that one only needs the matrix-vector product (apart from simple vector operations) and that the matrix does not need to be explicitly stored in the RAM. With the Lanczos algorithm, eigenvalues and eigenvectors of matrices with dimensions of the order $\mathcal{O}(10^{11})$ can be calculated [55]. However, very large systems such as the previously mentioned Fe_{18} and $Mo_{72}Fe_{30}$ still cannot be treated with exact diagonalization methods. DMRG effectively reduces the matrix dimension so that very large systems can be treated using this method.

Quantum Monte Carlo methods such as the stochastic series expansion [58] allow for an approximate, but very accurate calculation of thermodynamic expectation values of very large *unfrustrated* spin systems. Properties of frustrated systems can, however, only be calculated in the high-temperature regime, cf. Ref. [59].

2.2.3. Spectra of antiferromagnetic spin Hamiltonians

In this subsection, we discuss typical properties of the spectra of (isotropic) antiferromagnetic Heisenberg systems. The effect of a small anisotropy will be discussed later in Sec. 5.3.3. As a first example we calculate the spectrum of an exactly solvable system, the antiferromagnetic Heisenberg square with the Hamiltonian

$$H_{\text{square}} = J(\vec{s}_1 \cdot \vec{s}_2 + \vec{s}_2 \cdot \vec{s}_3 + \vec{s}_3 \cdot \vec{s}_4 + \vec{s}_4 \cdot \vec{s}_1)\,, \tag{2.13}$$

with all spins having the quantum number s. Alternatively, this system can be regarded as a spin ring with four spins. Fig. 2.3 shows a schematic representation of the system.

We can now rewrite this Hamiltonian using $\vec{S}_{13} \equiv \vec{s}_1 + \vec{s}_3$, $\vec{S}_{24} \equiv \vec{s}_2 + \vec{s}_4$, and the total spin $\vec{S} \equiv \vec{S}_{13} + \vec{S}_{24}$:

$$H_{\text{square}} = \frac{J}{2}(\vec{S}^2 - \vec{S}_{13}^2 - \vec{S}_{24}^2)\,. \tag{2.14}$$

One can see that the vector coupling states $|S_{13}S_{24}SM\rangle$[3] are eigenstates of this

[3] S_{13} and S_{24} are intermediate quantum numbers for this system that were summarized by α in

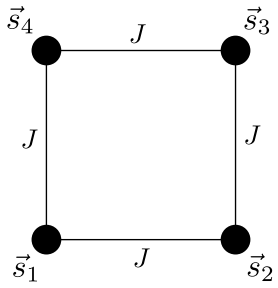

Figure 2.3.: Schematic representation of the antiferromagnetic Heisenberg square. The circles denote the individual spins and the lines denote the interactions between the spins.

Hamiltonian. The energy eigenvalues are:

$$E(S, S_{13}, S_{24}) = \frac{J}{2}(S(S+1) - S_{13}(S_{13}+1) - S_{24}(S_{24}+1)) \,, \tag{2.15}$$

with $S_{13}, S_{24} \in \{0, 1, \ldots, 2s\}$ and $S \in \{|S_{13} - S_{24}|, |S_{13} - S_{24}| + 1, \ldots, S_{13} + S_{24}\}$. An example of the complete spectrum is shown in Fig. 2.4.

This spectrum has some properties that are typical for many antiferromagnetic Heisenberg systems. In the following, we discuss some aspects. We always assume that we have an even number of spins that all have the same quantum number s.

Ordering of energy levels and ground state spin quantum number

Lieb and Mattis have rigorously proved in 1962 for antiferromagnetic Heisenberg systems which fulfill condition (2.16) that the ground state is a singlet (i.e., $S = 0$) and that the minimal energies in the S subspaces, denoted as $E_{\min}(S)$, obey $E_{\min}(S) < E_{\min}(S+1)$ [52]. This behavior can also be seen in Fig. 2.4. The condition is that the system can be divided into two sublattices A and B with a constant $g^2 \geq 0$ such that for all lattice positions

$$J_{i_A j_A} \leq g^2 \,, \quad J_{i_B j_B} \leq g^2 \,, \text{and} \quad J_{i_A j_B} \geq g^2 \tag{2.16}$$

holds. Here, i_A and j_A denote positions on sublattice A, and i_B and j_B denote positions on sublattice B. The condition with $g^2 = 0$ thus means that spins on different sublattices interact either antiferromagnetically or not at all, i.e., the system is bipartite in the sense of the previously given definition.

the previous subsection. $\vec{s}_1$ and $\vec{s}_3$ are coupled to $\vec{S}_{13}$, and $\vec{s}_2$ and $\vec{s}_4$ to $\vec{S}_{24}$. Then, $\vec{S}_{13}$ and $\vec{S}_{24}$ are coupled to the total spin $\vec{S}$.

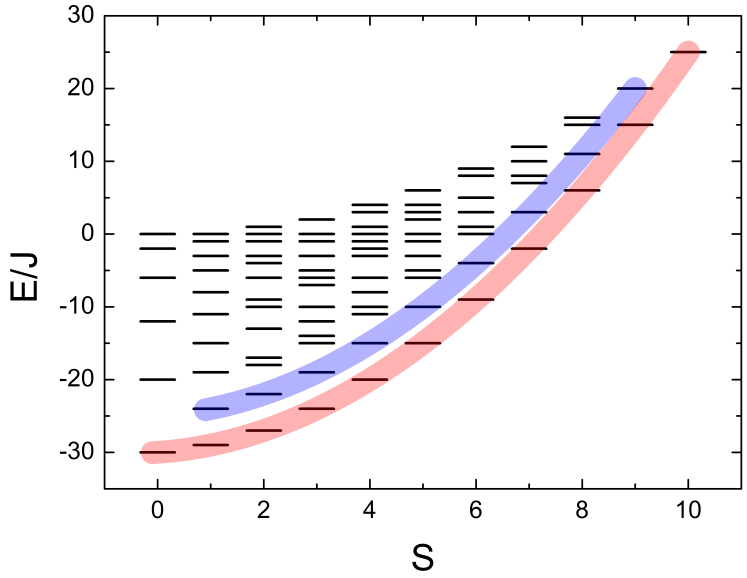

Figure 2.4.: Spectrum of the antiferromagnetic Heisenberg square with $s = 5/2$. The red background marks the lowest rotational band (L band) and the next-higher rotational band (also called E band [37]) is marked blue (see text).

Rotational bands

The ordering of energy levels as stated above was proved by Lieb and Mattis only for systems obeying condition (2.16). However, numerical investigations show that such an ordering also exists for many other systems. Furthermore, the dependence of the lowest energy eigenvalues on S is often approximately parabolic as for the square [19, 20, 30, 37, 39, 60–65], i.e.,

$$E_{\min}(S) - E_0 \approx \text{const.} \times S(S+1)\,, \tag{2.17}$$

This structure is called "rotational band" [64], "L band" [37], or is described as following the Landé interval rule [30]. The spectrum of antiferromagnetic Heisenberg systems which fulfill the Lieb-Mattis condition with $g^2 = 0$ and $J_{i_A j_B} = J\ \forall i_A, j_B$ ("Lieb-Mattis model") can be calculated analytically in the same way as for the Heisenberg square and the energy eigenvalues are $E_{\text{Lieb-Mattis}}(S, S_A, S_B) = \frac{J}{2}(S(S+1) - S_A(S_A+1) - S_B(S_B+1))$ [52]. S_A is the spin quantum number of sublattice spin $\vec{S}_A \equiv \sum_{i_A} \vec{s}_{i_A}$ and likewise for S_B. The parabolic dependence on S is also exact for systems where each spin interacts with every other spin with the same strength, since then the Hamiltonian can always be rewritten as $H = J\sum_{i<j} \vec{s}_i \cdot \vec{s}_j = \frac{J}{2}(\vec{S}^2 - \sum_i \vec{s}_i^2)$. Also, many classical spin systems show an exact parabolic dependence of that form [66].

For quantum systems that do not belong to the Lieb-Mattis-type models, a "derivation" of the (approximate) parabolic dependence and justification for using an approximation based on rotational bands can be given as follows [64, 67, 68]. In the Lieb-Mattis model, the system can be divided into two sublattices, and the sublattice spins couple to their maximum value for the (relative) ground states as a function of S. The idea of the *rotational band approximation* is to use these states as approximations of the relative ground states also for other models. Let us first consider a bipartite antiferromagnetic Heisenberg system with N spins, e.g., a simple spin ring with the Hamiltonian

$$H_{\text{ring}} = J \sum_{i=1}^{N} \vec{s}_i \cdot \vec{s}_{i+1} \,, \quad N+1 \equiv 1 \,, \tag{2.18}$$

with $J > 0$. We couple the sublattice spins to their maximal values, $S_A = Ns/2$ and $S_B = Ns/2$, and the approximations for the relative ground states are given by $|S_A S_B S M\rangle$. This state is a kind of "quantum Néel state", but not a classical "up-down" Néel state, which is not an $\vec{S}^2$ eigenstate. Within this basis, the spin ring Hamiltonian is equivalent to the two-spin Hamiltonian [67, 68]

$$H_{AB} = a_1 J \vec{S}_A \cdot \vec{S}_B = a_1 \frac{J}{2} (\vec{S}^2 - \vec{S}_A^2 - \vec{S}_B^2) \,, \tag{2.19}$$

i.e.,

$$\langle S_A S_B S M | H_{AB} | S_A S_B S M \rangle = \langle S_A S_B S M | H_{\text{ring}} | S_A S_B S M \rangle \,, \tag{2.20}$$

with $a_1 = 4/N$. The energy eigenvalues of the two-spin Hamiltonian H_{AB} are $E_{AB}(S) = a_1 \frac{J}{2}(S(S+1) - S_A(S_A+1) - S_B(S_B+1))$, i.e., they depend quadratically on S. Because of the variational principle, the energy $\langle S_A S_B S M | H_{\text{ring}} | S_A S_B S M \rangle$ is always bounded from below by the true (relative) ground state energy of the full N-spin Hamiltonian H_{ring}. The two-spin Hamiltonian H_{AB} has a much smaller Hilbert space dimension ($(Ns+1)^2$) than the original Hamiltonian and can even be solved analytically unless anisotropic terms are included. It is therefore used as an approximation if the full Hamiltonian cannot be treated numerically, see, e.g., Refs. [10, 67]. It is also possible to include anisotropic terms or to use other values for the constant a_1 in order to get better approximations for small spin quantum numbers [68]. The rotational band states are expected to be good approximations especially for large s and small N [37]. This will be analyzed in Sec. 5.2.1.

For a three-colorable system, i.e., a system that can be divided into three sublattices A, B, and C such that spins on different sublattices do not interact, one can devise a similar strategy by using states of the form $|S_A S_B S_C S M\rangle$, or equivalently a three-spin Hamiltonian of the form $H_{ABC} = cJ(\vec{S}_A \cdot \vec{S}_B + \vec{S}_B \cdot \vec{S}_C + \vec{S}_C \cdot \vec{S}_A)$, as an approximation [12, 16, 64].

The procedure can be extended by also using states where the sublattice spins are not coupled to their maximum values. If the sublattice spins are coupled to their maximal value and the energies $E_{AB}(S)$ or $E_{ABC}(S)$ are minimal, the corresponding energy values are called first (or lowest) rotational band or L band. If one of the sublattice spins is coupled to the maximal value minus one and the other sublattice spins to their maximal values, the corresponding energy eigenvalues are called second rotational band (cf. Fig. 2.4) [16, 37].

The rotational band approximation has been used with some success for different antiferromagnetic spin systems, see, e.g., Refs. [10, 16, 17, 39, 63, 67, 68].

Shift quantum numbers of spin rings

In this paragraph we focus on uniform antiferromagnetic isotropic rings with N spins and the same spin quantum number s for all spins. Some of the properties that are listed below will be used in chapter 5. We always assume that the Hamiltonian has the form H_{ring}, see Eq. (2.18). Spin rings with a Hamiltonian of this form are translational invariant, i.e., H_{ring} commutes with the shift operator $\mathcal{T}$ [69]. The shift operator $\mathcal{T}$ can be defined by its action on a state of the product basis:

$$\mathcal{T}|m_1 m_2 \dots m_N\rangle \equiv |m_N m_1 m_2 \dots m_{N-1}\rangle \,. \tag{2.21}$$

$\mathcal{T}$ also commutes with $\vec{S}^2$ and S^z. All eigenstates of a spin ring can be labeled according to S, M, and the shift quantum number k. The shift quantum number k can take the values $k = 0, 1, \dots, N-1$ and labels eigenstates of $\mathcal{T}$ according to

$$\mathcal{T}|k\rangle = e^{-\frac{2\pi i k}{N}}|k\rangle \,. \tag{2.22}$$

If the ring has an even number of spins, the theorem of Lieb and Mattis applies, so that the ground state is a singlet and the lowest energy levels in the S subspaces are ordered according to $E_{\min}(S) < E_{\min}(S+1)$. Furthermore, rigorous results for the shift quantum numbers of these relative ground states can be derived [70] (we assume here an even N):

1. If s is an integer or Ns is even, the shift quantum number of the ground state is $k = 0$.

2. If s is half-integer and Ns is odd, the shift quantum number of the ground state is $k = N/2$.

3. The lowest energy eigenstates in the eigenspaces of S have the shift quantum numbers 0, $N/2$, 0, $N/2, \dots$ for $S = Ns, Ns-1, Ns-2, Ns-2, \dots$, i.e., starting from the subspace with the largest possible S.

If $k \neq 0, N/2$, energy eigenstates with k and $N-k$ have the same energy, i.e., are degenerate [37].

2.3. Typical observables and experimental techniques

Measurements of the magnetization as a function of the applied magnetic field and temperature, and inelastic neutron scattering (INS) are very powerful techniques that are often applied to magnetic molecules [3, 28]. Other typical techniques are, e.g., nuclear magnetic resonance (NMR), measurements of the specific heat, or electron paramagnetic resonance [3]. We focus on the formulas needed for the calculation of the magnetization and the simulation of INS experiments in the following subsections. The DMRG and DDMRG techniques, which we mainly use for the theoretical calculations in this work, are very well suited to make predictions relevant for magnetization measurements and INS experiments.

2.3.1. Magnetization

The magnetization of magnetic molecules can, e.g., be measured with SQUIDs (see chapter 3 of Ref. [3]). On the theory side, the thermal expectation value of the magnetization operator as a function of magnetic field $\vec{B}$ and temperature $T \equiv 1/(k_B\beta)$ has to be calculated for the comparison with experimental data. The magnetization operator is defined as $-g\mu_B\vec{S}$ [71]. The (thermal equilibrium) expectation value of the magnetization, $\vec{\mathcal{M}}$, can then be calculated as

$$\vec{\mathcal{M}}(T,\vec{B}) = -\frac{g\mu_B}{Z}\,\mathrm{Tr}\,\{\,\vec{S}\,e^{-\beta H(\vec{B})}\,\}\,, \tag{2.23}$$

with $Z = \mathrm{Tr}\,\{\,e^{-\beta H(\vec{B})}\,\}$. If we have an isotropic Heisenberg Hamiltonian, the direction of the magnetic field does not matter and we can, e.g., choose $\vec{B} = B\vec{e}_z$. In this case, the magnetization has only a non-vanishing z component, i.e., $\vec{\mathcal{M}} = \mathcal{M}\vec{e}_z$. The expectation value can then be calculated as

$$\begin{aligned}\mathcal{M}(T,B) &= -\frac{g\mu_B}{Z}\,\mathrm{Tr}\,\{\,S^z\,e^{-\beta H(B)}\,\}\\ &= -\frac{g\mu_B}{Z}\sum_i M_i e^{-\beta E_i(B)}\,,\end{aligned} \tag{2.24}$$

where $E_i(B) = E_i + g\mu_B B M_i$ denotes the energy eigenvalues (E_i is the energy eigenvalue of the Heisenberg Hamiltonian without Zeeman interaction) and M_i the S^z eigenvalues of the corresponding eigenstates.

Although measurements at exactly $T = 0$ are, of course, not possible, very low temperatures can be reached so that in some cases it is reasonable to compare the simulated $T = 0$ magnetization with experimental low-temperature data. At $T = 0$, the system is always in the ground state. Let again $E_{\min}(S)$ denote the minimal energy for a fixed S without magnetic field. If $B > 0$, an additional energy of $g\mu_B BM$ has to be added, so that the energies

$$E(S,M,B) = E_{\min}(S) + g\mu_B BM \tag{2.25}$$

become M-dependent. To find the state with minimal energy for a given B, Eq. (2.25) has to be minimized with respect to M and S. The energy is minimal with respect to M for $M = -S$ (for $B > 0$). If we have a system for which $E_{\min}(S) < E_{\min}(S+1)$, the magnetic fields at which the ground state spin "jumps" from S to $S+1$ are[4]

$$B_{S\to S+1} = \frac{E_{\min}(S+1) - E_{\min}(S)}{g\mu_B}\,. \tag{2.26}$$

This means that one only needs the minimal energies in the S subspaces of the unperturbed system (i.e., without external field) to calculate the $T = 0$ magnetization curve for an isotropic Heisenberg system.

This procedure is visualized in Fig. 2.5 for the antiferromagnetic Heisenberg square. We only show the eigenvalues of the states with $M = -S$, since only these states are relevant.

In general, if the minimal energies depend quadratically on S, the resulting $T = 0$ magnetization curve always shows equidistant steps until the saturation magnetization is reached.

2.3.2. Inelastic neutron scattering (INS)

Neutrons are almost ideal for spectroscopy experiments on magnetic molecules. Since they have a magnetic moment, but no charge, they only interact with the nuclei and the magnetic moments of the unpaired electrons (i.e., the spins) in the sample [73]. INS allows to probe transitions to excited states so that direct conclusions about the spectrum can be drawn. In inelastic neutron scattering experiments, changes in the kinetic energies and the momenta of the neutrons are measured [3, 73, 74], see Fig. 2.6. The energy of a neutron with wave vector $\vec{q}$ is $E = \hbar^2 q^2/(2m)$, so that the transferred energy is given by[5]

$$\omega = \frac{\hbar^2}{2m}(q^2 - q'^2) = E - E'\,. \tag{2.27}$$

Here, $\vec{q}\,'$ denotes the wave vector of the neutron after leaving the sample. The transferred momentum $\hbar\vec{Q}$ is given by

$$\hbar\vec{Q} = \hbar(\vec{q} - \vec{q}\,'). \tag{2.28}$$

Measurements of the fraction of neutrons that are scattered with momentum transfer $\hbar\vec{Q}$ and energy transfer ω allow for a comparison to theoretical calculations. It is possible to derive an equation for the calculation of the double differential cross section $d^2\sigma/d\Omega d\omega$ for inelastic neutron scattering. We do not describe the derivation

[4] Also, the energies $E_{\min}(S)$ need to be convex [72].

[5] Here and in the following, ω has the dimension of energy.

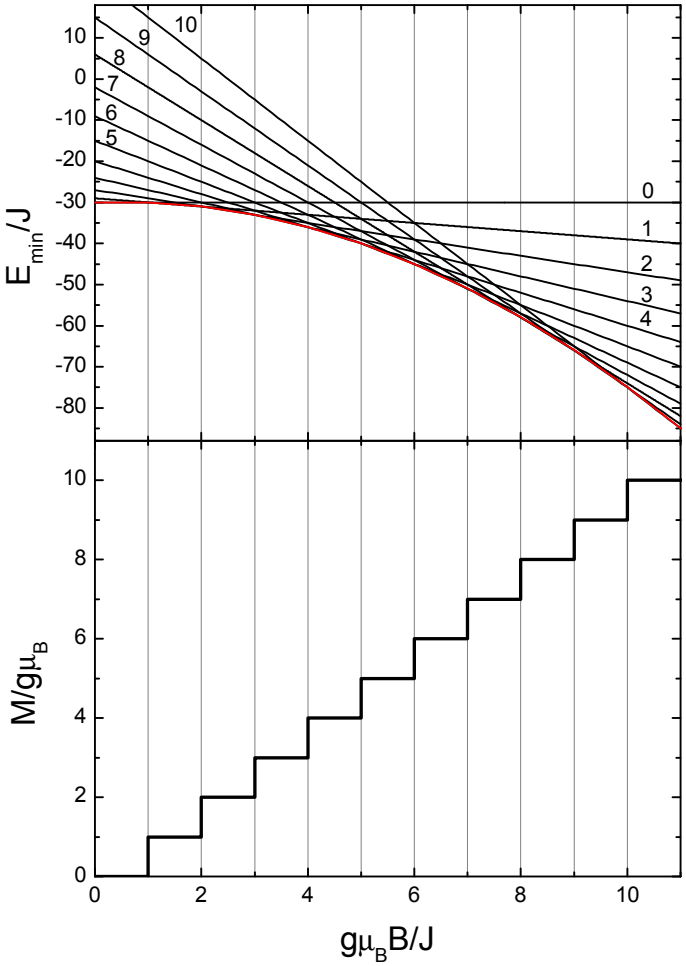

Figure 2.5.: Lowest energies in each S sector as a function of $g\mu_B B$ (top) and $T = 0$ magnetization curve (bottom) for the antiferromagnetic Heisenberg square with $s = 5/2$. The numbers above the lines denote the S quantum numbers of the corresponding eigenstates. The red line shows the ground state energy as a function of $g\mu_B B$.

here; it can be found in standard textbooks on neutron scattering, see, e.g., Refs. [73, 74]. $d^2\sigma/d\Omega d\omega$ describes the number of neutrons scattered per second into the infinitesimal solid angle $d\Omega$, with energy transfers between ω and $\omega + d\omega$, divided by the number of incoming neutrons per second. The derivation is based on Fermi's golden rule. The final result for the double differential cross section for inelastic

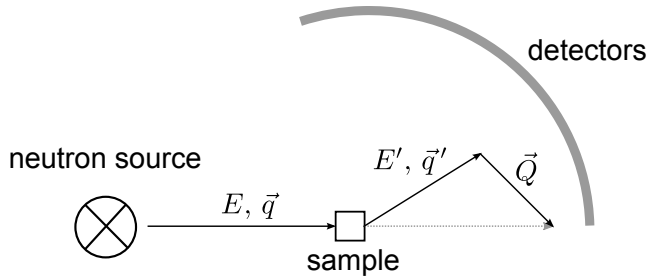

Figure 2.6.: Schematic illustration of inelastic neutron scattering. An incoming neutron with wave vector $\vec{q}$ and energy E is scattered in the sample and leaves with wave vector $\vec{q}'$ and energy E'.

neutron scattering on magnetic systems is [73, 74]

$$\frac{d^2\sigma}{d\Omega d\omega} = \text{const.} \times \frac{q'}{q} e^{-2W(Q,T)} F^2(\vec{Q}) \sum_{\alpha,\beta} \left(\delta_{\alpha\beta} - \frac{Q_\alpha Q_\beta}{Q^2} \right) S^{\alpha\beta}(\vec{Q},\omega)\,, \qquad (2.29)$$

where $\alpha, \beta = x, y, z$, $\exp[-2W(Q,T)]$ is the Debye-Waller factor, and $F(\vec{Q})$ is the form factor of a magnetic ion which is assumed to be the same for all magnetic centers. In the following, we only consider the limit $T = 0$. Apart from the Debye-Waller factor and the magnetic form factor, the only system-dependent part of equation (2.29) is the dynamical correlation function $S^{\alpha\beta}(\vec{Q},\omega)$, also called magnetic scattering function, which is defined as [73]

$$S^{\alpha\beta}(\vec{Q},\omega) = \sum_{j,j'} e^{i\vec{Q}\cdot(\vec{R}_j - \vec{R}_{j'})} \sum_{m,n} \frac{e^{-\beta E_m}}{Z} \langle m|s_j^\alpha|n\rangle\langle n|s_{j'}^\beta|m\rangle\, \delta(\omega - E_n + E_m)\,, \quad (2.30)$$

where Z denotes the partition function. For zero temperature, this expression simplifies to

$$S^{\alpha\beta}(\vec{Q},\omega) = \sum_{j,j'} e^{i\vec{Q}\cdot(\vec{R}_j - \vec{R}_{j'})} S_{jj'}^{\alpha\beta}(\omega)\,, \qquad (2.31)$$

with

$$S_{jj'}^{\alpha\beta}(\omega) \equiv \sum_n \langle 0|s_j^\alpha|n\rangle\langle n|s_{j'}^\beta|0\rangle\, \delta(\omega - E_n + E_0). \qquad (2.32)$$

Here, $|n\rangle$ denotes an energy eigenvector with energy E_n. $|0\rangle$ is the ground state. If the ground state was degenerate, one would have to sum over all degenerate states with equal weight. $\vec{R}_j$ denotes the position of the jth magnetic ion. As already mentioned before, we only consider the zero-temperature dynamical correlation function in the following.

Selection rules and isotropic systems

In this thesis, the cross section is only calculated for isotropic systems. This leads to some simplifications and to selection rules. The selection rules for matrix elements of the form $\langle S'M'|s_j^\alpha|SM\rangle$ are (the matrix element is zero, if the selection rules are not fulfilled) [73]

$$\Delta S \equiv S' - S = 0, \pm 1 \quad \text{and} \quad \Delta M \equiv M' - M = 0, \pm 1\,. \tag{2.33}$$

However, $S = 0 \to S' = 0$ transitions are also not allowed [75], so that for systems with a singlet ground state only transitions to $S = 1$ states are possible.

Furthermore, it can be shown that one only has to consider $S^{zz}_{jj'}(\omega)$ in the differential cross section formula. Terms with $\alpha \neq \beta$ cancel out and $S^{\alpha\alpha}_{jj'}(\omega) = S^{zz}_{jj'}(\omega)$ $\forall\,\alpha$. This has the consequence that

$$\sum_{\alpha,\beta}\left(\delta_{\alpha\beta} - \frac{Q_\alpha Q_\beta}{Q^2}\right) S^{\alpha\beta}(\vec{Q},\omega) = 2S^{zz}(\vec{Q},\omega)\,, \tag{2.34}$$

and the differential cross section formula acquires a much simpler structure.

Powder samples

Since inelastic neutron scattering experiments in the field of molecular magnetism are usually performed on powder samples, the orientation of the molecules is essentially random and one has to average over all directions of $\vec{Q}$ [76]:

$$\begin{aligned} S^{zz}(Q,\omega) &\equiv \frac{1}{4\pi}\int d\Omega \sum_{j,j'} e^{i\vec{Q}\cdot(\vec{R}_j - \vec{R}_{j'})} S^{zz}_{jj'}(\omega) \\ &= \sum_{j,j'} \frac{\sin(QR_{jj'})}{QR_{jj'}} S^{zz}_{jj'}(\omega)\,, \end{aligned} \tag{2.35}$$

with $R_{jj'} \equiv |\vec{R}_j - \vec{R}_{j'}|$ and $Q = |\vec{Q}|$.

Integration over all $\vec{Q}$

To obtain a function that is independent of $\vec{Q}$ and the positions of the ions, $\vec{R}_j$, we can average over all $\vec{Q}$ [77]:

$$S^z(\omega) \equiv \frac{\int d^3Q S^{zz}(\vec{Q},\omega)}{\int d^3Q} = \sum_j S^{zz}_{jj}(\omega) \equiv \sum_j S^z_j(\omega)\,. \tag{2.36}$$

Here we have used $\int d^3Q\, e^{i\vec{Q}\cdot(\vec{R}_j - \vec{R}_{j'})} / \int d^3Q = \delta_{jj'}$ [73]. We get the same result if we calculate $\int dQ S^{zz}(Q,\omega) / \int dQ$ and omit a factor Q^2, which we would have for

a three-dimensional averaging. If we have a translational invariant system, e.g., a uniform spin ring, the sum over j simplifies to $NS_j^z(\omega)$ with an arbitrary j.

For INS experiments performed with time-of-flight spectrometers, the integration over all scattering angles is not equal to the expression above and the detector geometry is relevant [78]. This will be analyzed below. Note that the form factors and the Debye-Waller factor are ignored if one uses Eq. (2.36) for a direct comparison with experimental data.

For highly symmetric systems such as rings, the function $S_j^z(\omega)$ and the knowledge of the spacial quantum numbers of the participating energy levels are sufficient to reconstruct the momentum dependent function $S^{zz}(\vec{Q},\omega)$ [76].

The integration over all ω leads to a useful sum rule for the dynamical correlation functions $S_j^z(\omega)$ for the case of an isotropic system:

$$\begin{aligned}\int_{-\infty}^{+\infty} d\omega\, S_j^z(\omega) &= \sum_n |\langle 0|s_j^z|n\rangle|^2 = \langle 0|(s_j^z)^2|0\rangle \\ &= \frac{1}{3}s(s+1)\,. \end{aligned} \tag{2.37}$$

Simulation of time-of-flight INS data

To properly simulate INS data that were obtained by summing over all detector banks, the formulas introduced above need to be modified [78–80]. The reason is that if the data are collected over a range of scattering angles, the range of possible Q values depends not only on the the detector geometry, but also on the energy transfer. At first, we give the formula for the momentum transfer as a function of ϑ (the scattering angle, i.e., angle between $\vec{q}$ and $\vec{q}\,'$, in degree), ω (energy transfer, in meV), and λ (wavelength of the incoming neutrons, in Å^{-1}):

$$Q(\omega,\,\vartheta,\,\lambda) = \sqrt{\frac{8\pi^2}{\lambda^2} - \frac{4\pi\cos\vartheta}{\lambda}\sqrt{\frac{4\pi^2}{\lambda^2} - 0.4826\,\omega} - 0.4826\,\omega}\,. \tag{2.38}$$

This equation can easily be derived using the scattering triangle (see Fig. 2.6).

In Ref. [78] the following formula was given to simulate time-of-flight data:

$$I(\omega) = \int_{Q_{\min}(\omega)}^{Q_{\max}(\omega)} dQ\, g(Q)F^2(Q)S^{zz}(Q,\,\omega)\,, \tag{2.39}$$

where $g(Q)$ is the density of detectors per Q interval, and $Q_{\min/\max}(\omega)$ are the minimum/maximum Q value for fixed ω and can be calculated via Eq. (2.38) by inserting the minimum/maximum scattering angle. This equation will be used in chapter 5.

Application to the Heisenberg square

As an example, we explicitly calculate $S_j^z(\omega)$ for the spin-s Heisenberg square with Hamiltonian (2.13). The energy eigenvalues of this system are $E(S, S_{13}, S_{24}) = \frac{J}{2}(S(S+1) - S_{13}(S_{13}+1) - S_{24}(S_{24}+1))$ and the eigenstates have the form $|S_{13}S_{24}SM\rangle$ (see Eq. (2.15)). This means, we have to calculate the matrix elements

$$\langle S'_{13}S'_{24}S'M'|s_j^z|S_{13}S_{24}SM\rangle\,. \tag{2.40}$$

In addition to the standard INS selection rules (2.33), we have the following selection rules for the intermediate quantum numbers [37, 42]:

$$\Delta S_{13} = 0 \quad \text{and} \quad \Delta S_{24} = 0, \pm 1\,, \tag{2.41}$$

or

$$\Delta S_{13} = 0, \pm 1 \quad \text{and} \quad \Delta S_{24} = 0\,. \tag{2.42}$$

The ground state has $S_{13} = S_{24} = 2s$. Since $E(S, 2s, 2s-1) = E(S, 2s-1, 2s)$, only two distinct transitions contribute to the dynamical correlation functions $S_j^z(\omega)$: a transition within the lowest rotational band (L band) and a transition to the second rotational band (E band). These transitions are shown in Fig. 2.7. The squared matrix element for the transition to the first excited state is (see appendix A.1 and Refs. [42, 73] for details of the calculation):

$$|\langle 2s, 2s, S' = 1, M' = 0|s_j^z|2s, 2s, S = 0, M = 0\rangle|^2 = \frac{1}{3}s\left(s + \frac{1}{2}\right)\,. \tag{2.43}$$

The weight of the transitions to the states with $S_{13} = 2s - 1$ (and $S_{24} = 2s$) or $S_{24} = 2s - 1$ (and $S_{13} = 2s$) can then be deduced using the sum rule (2.37):

$$[\text{weight of all other transitions}] = \frac{1}{3}s(s+1) - \frac{1}{3}s\left(s + \frac{1}{2}\right) = \frac{1}{6}s\,. \tag{2.44}$$

The excitation energies are $\Delta E_1 = J$ and $\Delta E_2 = (1+2s)J$. The resulting dynamical correlation function for $s = 5/2$ is shown in Fig. 2.8.

Rotational band approximation

As a second example, we calculate the dynamical correlation function $S_j^z(\omega)$ in the rotational band approximation (cf. Sec. 2.2.3) for antiferromagnetic spin rings with an even number N of spins. The idea of the rotational band approximation for such systems was to use the states $|S_A S_B SM\rangle$ as approximations of the true eigenstates, or alternatively to use an effective two-spin Hamiltonian $H_{AB} \propto \vec{S}_A \cdot \vec{S}_B$ instead of

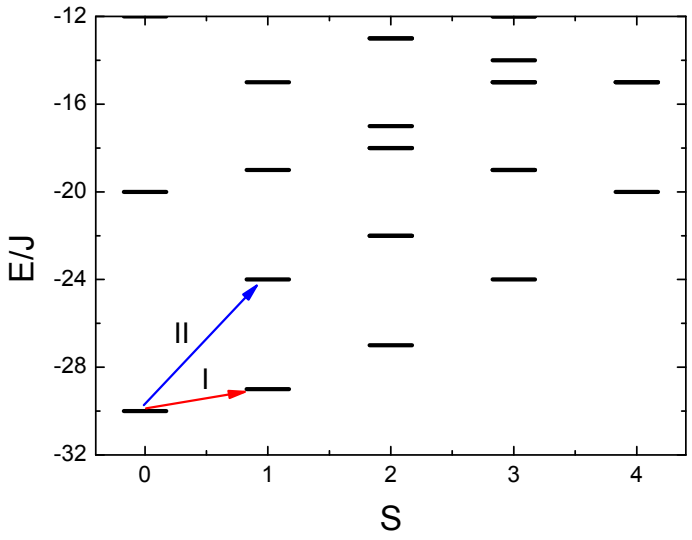

Figure 2.7.: Low-energy part of the spectrum of the spin-5/2 Heisenberg square (cf. Fig. 2.4). The arrows mark the transitions from the ground state which are relevant for INS, i.e., which have nonzero weight. The red arrow shows the transition within the L band, and the blue arrow shows the transition to the E band.

the full Hamiltonian. S_A and S_B are the sublattice spin quantum numbers. For the lowest rotational band we have $S_A = S_B = Ns/2$. To determine the dynamical correlation function in this approximation, we need the squared matrix elements $|\langle S'_A S'_B S' M'|s^z_j|S_A S_B S M\rangle|^2$.

The states $|S_A S_B S M\rangle$ are exact eigenstates of the Heisenberg square, so that the calculation of the matrix elements is completely analogous to that case, see appendix A.1. In addition to the standard INS selection rules we again have selection rules for the sublattice spin quantum numbers:

$$\Delta S_A = 0 \quad \text{and} \quad \Delta S_B = 0, \pm 1\,, \tag{2.45}$$

or

$$\Delta S_A = 0, \pm 1 \quad \text{and} \quad \Delta S_B = 0\,. \tag{2.46}$$

As for the Heisenberg square, only two distinct peaks can appear in the dynamical correlation function. The matrix elements can be calculated in the same way as for the Heisenberg square and the final result is ($S_A = S_B = Ns/2$)

$$|\langle S_A, S_B, S' = 1, M' = 0|s^z_j|S_A, S_B, S = 0, M = 0\rangle|^2 = \frac{1}{3} s \left(s + \frac{2}{N}\right)\,. \tag{2.47}$$

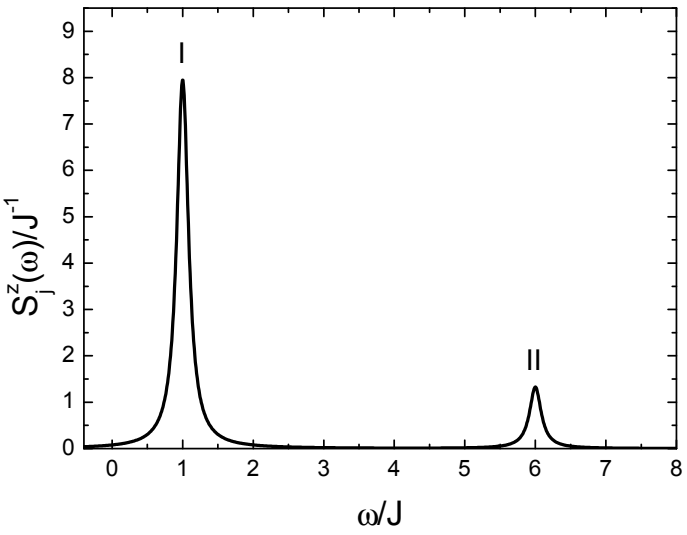

Figure 2.8.: Zero-temperature dynamical correlation function $S_j^z(\omega)$ for the spin-5/2 Heisenberg square. For visualizing purposes, the delta functions were replaced by Lorentzians $\eta/\pi(x^2+\eta^2)$ with $\eta = 0.1\,J$. The roman numerals mark the peaks corresponding to the transition within the L band ("I") and the transition to the E band ("II"), see Fig. 2.7.

The weight of all remaining peaks is $\frac{1}{3}s(1-\frac{2}{N})$. The excitation energies are $\Delta E_1 = J$ and $\Delta E_2 = (\frac{4}{N}+2s)J$. However, a comparison with spectra of the "full" Hamiltonians shows that the rotational band approximation is too simple for excitations beyond the lowest rotational band for spin rings with $N > 6$ [37]. This will also be shown in chapter 5.

3. The density matrix renormalization group (DMRG)

3.1. Introduction

The aim of this chapter is to give an overview of the basics of the density matrix renormalization group (DMRG) method and to present some details of the implementation that was developed for this work. The DMRG technique is a rather recent numerical technique and was introduced by S. White in 1992 [5] to overcome problems that occurred when the numerical renormalization group (NRG) [81, 82] was applied to quantum lattice models such as the Heisenberg or the Hubbard model [83]. The DMRG technique is a very efficient and, at least for many one-dimensional quantum lattice systems, also a very accurate numerical method. Since its invention in 1992 it has evolved into a widely-used, almost standard numerical method mostly applied to one-dimensional and quasi-one-dimensional systems [6, 84].

The calculation of properties such as the ground state energy, ground state expectation values, or energy gaps of quantum lattice models (e.g., the Heisenberg model or the Hubbard model) is always hindered by the exponentially growing dimension of the underlying Hilbert space. For a spin chain (with open boundary conditions) consisting of L spins with an individual spin quantum number s and the coupling constant set to one, the Heisenberg Hamiltonian looks like

$$H_{\text{chain}} = \sum_{i=1}^{L-1} \vec{s}_i \cdot \vec{s}_{i+1} \,. \tag{3.1}$$

In the following, we use this simple system as an example to demonstrate how the method works. The Hilbert space dimension is $(2s+1)^L$. This exponential dependence on the number of spins has the consequence that, if complete exact diagonalization techniques are used, one is limited to rather small systems, even if all symmetries are used [51]. One solution to this dilemma are Monte Carlo methods [58], which, however, suffer from the so-called negative-sign problem for fermionic or frustrated spin systems [85]. NRG and DMRG are approximate numerical techniques that are based on a truncation of the Hilbert space and can thus be applied to rather large systems. They do not suffer from the negative-sign problem.

In the following section, the principles of basis truncation in the NRG and DMRG method are introduced and compared to each other. In sections 3.3 and 3.4, the

DMRG algorithm and the implementation as developed for this thesis are described. In section 3.5, the connection to so-called matrix product states (MPS) is briefly discussed. The first sections use the simple open spin chain (Eq. (3.1)) as an example. In section 3.6, it is described how to apply the DMRG method to spin systems that are not one-dimensional. Section 3.7 covers the dynamical DMRG (DDMRG) technique. The last section contains some tests of the basic properties of the DMRG algorithm and of the program that was developed for this work. The first sections of this chapter are in large parts based on the excellent and comprehensive introduction to the DMRG technique in Ref. [6].

3.2. Basis truncation

The density matrix renormalization group is a numerical method which relies on an effective truncation of the Hilbert space of quantum lattice models. The variational theorem states that the ground state energy that is calculated in a reduced Hilbert space is always higher or equal to the exact ground state energy [50]. This means that the lower the calculated ground state energy within the reduced space, the better is the approximation. In some sense, the DMRG basis truncation is optimal, as will be shown later. However, we first describe the simpler basis truncation used in the NRG.

3.2.1. Real-space NRG truncation

Let us assume we are interested in calculating ground state properties of the spin chain (3.1), but using only a limited number of basis states. A simple basis truncation scheme, which is used in the NRG method, is the following: One starts with a very small system and does a piecewise enlargement while truncating the basis after each enlargement step. The spin chain Hamiltonian in Eq. (3.1) can recursively be constructed in the following way (H_l denotes the Hamiltonian for the chain with $l \leq L$ spins):

$$H_l = H_{l-1} + s^z_{l-1} s^z_l + \frac{1}{2}\left(s^+_{l-1} s^-_l + s^-_{l-1} s^+_l\right) . \tag{3.2}$$

This step enlarges the chain by one spin and the underlying Hilbert space by a factor of $d_S = 2s + 1$. Since we are interested in calculating the ground state, we might think of a truncation scheme based on keeping the energy eigenvectors with the smallest eigenvalues as basis vectors for the next step. To do so, we could set a threshold basis dimension m and as soon as Hilbert space dimension for the chain with l spins, $D_l = (2s+1)^l$, is larger than this value, H_l is replaced by $T^\dagger H_l T$, where

T contains the m eigenvectors of H_l with the smallest eigenvalues:

$$T = \sum_{n=1}^{D_l} \sum_{n'=1}^{m} |n\rangle\langle n'| \,, \tag{3.3}$$

where both $|n\rangle$ and $|n'\rangle$ denote energy eigenstates of H_l. The eigenstates are assumed to be ordered such that the corresponding eigenvalues obey $E_n \leq E_{n+1}\ \forall n$. The operators s_l^z, s_l^+, and s_l^- have to be likewise transformed for the next step, of course. Then, $T^\dagger H_l T$ and $T^\dagger s_l^{z/+/-} T$ (represented by $m \times m$ matrices) are used for the construction of H_{l+1} and the basis is truncated again. This procedure (see Fig. 3.1) is repeated until the desired system size is reached.

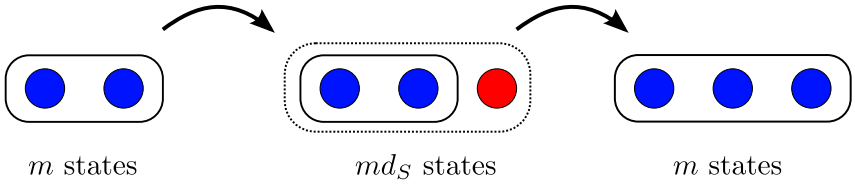

Figure 3.1.: Depiction of the NRG basis truncation procedure. The red circle shall illustrate a site with the basis dimension d_S that is added to the system (illustrated by the blue circles) with the basis dimension m. After diagonalization, the basis is truncated from md_S to m states.

This truncation procedure, however, yields unreliable results for many uniform systems such as the Hubbard model or the Heisenberg model (see Ref. [86] for a discussion of applications of this scheme). The unreliability of this procedure is often explained on the basis of a simple single-particle tight-binding model [6]. At the position where the site is added to the chain, the chain had a fixed boundary in the previous step and the basis states were chosen according to these boundary conditions. This results in wrong features of the wave function at the position where the site is added. For the single-particle model, fixed boundary conditions translate to nodes of the wave function at the boundary [6]. However, the ground state wave function of the enlarged system should have nodes only at the ends. A detailed discussion can be found in Ref. [83]. NRG was, however, originally not developed for uniform Heisenberg or Hubbard systems. It was developed for the solution of the Kondo problem [81]. In the Kondo model, the addition of a site is a small perturbation (because of a small relative coupling strength) and neglecting high-energy states turns out to have only a small effect on the low-energy spectrum. For the uniform Heisenberg or Hubbard model, the coupling strength between the sites stays constant and thus neglecting states on the basis of their energy is an "uncontrolled approximation", as pointed out by Costi in Ref. [84].

White and Noack were the first to notice that it is possible to overcome these problems by embedding the system that is enlarged and whose basis is truncated in a larger system [83]. This is the core idea of DMRG and improvement compared to NRG. It is discussed in the following subsection.

3.2.2. DMRG truncation

Let us again assume that we are interested in calculating the ground state of a quantum lattice system, e.g., a simple spin chain as in Eq. (3.1). Let us now divide the system into two subsystems which we call "block A" and "block B". For each of these blocks we have a complete orthonormal basis, $\{|i\rangle\}$ for block A and $\{|j\rangle\}$ for block B (see Fig. 3.2). The basis dimension of block A (B) is D_A (D_B).

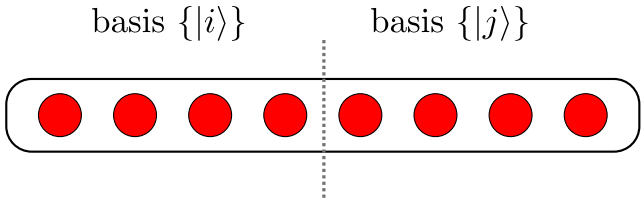

Figure 3.2.: Division of the system into two blocks. The red circles mark the "sites", i.e., the spins.

A normalized state $|\psi\rangle$ of the complete system, also called "superblock" (because it consists of two "blocks"), can be expanded in the following way:

$$|\psi\rangle = \sum_{i=1}^{D_A} \sum_{j=1}^{D_B} \psi_{ij} |i\rangle |j\rangle \,, \quad \sum_{i,j} |\psi_{ij}|^2 = 1 \,. \tag{3.4}$$

The state $|\psi\rangle$ can, e.g., be the ground state of the system, but the following statements are true for an arbitrary (normalized) superblock state. Before we proceed with the derivation of the "optimal" truncation scheme, we shortly recapitulate the concept of reduced density matrices [87].

Reduced density matrices: If we have a system divided into two blocks (subsystems) A and B, and the system is in a general mixed state ρ, the reduced density matrices ρ_A and ρ_B are defined as [87]

$$\rho_A \equiv \mathrm{Tr}_B \, \rho \;\text{ and }\; \rho_B \equiv \mathrm{Tr}_A \, \rho \,, \tag{3.5}$$

where $\mathrm{Tr}_B\{\cdot\}$ denotes a partial trace over all basis states $|j\rangle$ of block B, i.e., $\mathrm{Tr}_B\{\cdot\} \equiv \sum_j \langle j|\cdot|j\rangle$, and likewise for $\mathrm{Tr}_A\{\cdot\}$. This procedure yields an operator that acts only

on the Hilbert space of subsystem A or B. ρ_A and ρ_B both have the standard properties of a density matrix [88]. The expectation value of an operator O that also only acts on one of the subsystems, e.g., subsystem A, can then be calculated as [87]

$$\mathrm{Tr}\{\,\rho\,O\,\} = \mathrm{Tr}_A\{\,\rho_A\,O\,\}\,. \tag{3.6}$$

If the system is in a pure state $|\psi\rangle = \sum_{i,j}\psi_{ij}|i,j\rangle$ with $|i,j\rangle \equiv |i\rangle|j\rangle$, so that $\rho = |\psi\rangle\langle\psi| = \sum_{i,i',j,j'}\psi_{ij}\psi_{i'j'}|i,j\rangle\langle i',j'|$ (we assume here and in the following real coefficients), the reduced density matrices are calculated as follows:

$$\begin{aligned}\rho_A &= \mathrm{Tr}_B\{\,|\psi\rangle\langle\psi|\,\} = \sum_{i,i',j}\psi_{ij}\psi_{i'j}|i\rangle\langle i'|\,,\\ \rho_B &= \mathrm{Tr}_A\{\,|\psi\rangle\langle\psi|\,\} = \sum_{i,j,j'}\psi_{ij}\psi_{ij'}|j\rangle\langle j'|\,.\end{aligned} \tag{3.7}$$

As will be shown later, both density matrices have the same nonzero eigenvalues.

The problem of finding the optimal approximation

$$|\tilde{\psi}\rangle = \sum_{a=1}^{m}\sum_{j=1}^{D_B}\tilde{\psi}_{aj}|a\rangle|j\rangle \tag{3.8}$$

of $|\psi\rangle$ with only $m < D_A$ basis states for block A has a solution [86] as will be shown in the following. Mathematically, we are solving the following problem (we closely follow the derivation in Ref. [6]): We look for a transformation U_{ai} to orthonormal states

$$|a\rangle = \sum_i U_{ai}|i\rangle \equiv \sum_i\langle i|a\rangle|i\rangle\,,\ \langle a|a'\rangle = \delta_{aa'} \tag{3.9}$$

and coefficients $\tilde{\psi}_{aj}$, so that the square of the distance,

$$||\psi\rangle - |\tilde{\psi}\rangle|^2\,, \tag{3.10}$$

is minimal. Inserting (3.4), (3.8), and (3.9) yields (again assuming real coefficients)

$$||\psi\rangle - |\tilde{\psi}\rangle|^2 = 1 + \sum_{a,j}\tilde{\psi}_{aj}^2 - 2\sum_{a,i,j}\tilde{\psi}_{aj}U_{ai}\psi_{ij}\,. \tag{3.11}$$

Minimizing this expression with respect to $\tilde{\psi}_{aj}$ leads to the condition $\tilde{\psi}_{aj} = \sum_i U_{ai}\psi_{ij}$, so that

$$||\psi\rangle - |\tilde{\psi}\rangle|^2 = 1 - \sum_{a,j}\tilde{\psi}_{aj}^2\,. \tag{3.12}$$

Finding the minimum of this expression is equivalent to finding the maximum of

$$\sum_{a,j} \tilde{\psi}_{aj}^2 = \sum_{a,i,i',j} U_{ai} U_{ai'} \psi_{ij} \psi_{i'j} \equiv \sum_{a,i,i'} U_{ai} U_{ai'} (\rho_A)_{ii'} \,, \tag{3.13}$$

where $(\rho_A)_{ii'}$ are the matrix elements of the reduced density matrix (see Eqs. 3.7) of block A in the basis $\{|i\rangle\}$. This means that the eigenvalues w_a of ρ_A have the properties $0 \leq w_a \leq 1$ and $\sum_{a=1}^{D_A} w_a = 1$. The equation can now be rewritten using $U_{ai} = \langle i|a\rangle$:

$$\sum_{a,j} \tilde{\psi}_{aj}^2 = \sum_{a=1}^{m} \langle a|\rho_A|a\rangle \,. \tag{3.14}$$

This expression is maximal if we choose the $|a\rangle$ to be the eigenvectors of ρ_A with the largest eigenvalues [6, 86]. Summarizing, if we want to keep only m basis states for block A, $||\psi\rangle - |\tilde{\psi}\rangle|^2$ is minimal and hence the wave function approximation optimal if we approximate

$$|\psi\rangle = \sum_{i=1}^{D_A} \sum_{j=1}^{D_B} \psi_{ij} |i\rangle|j\rangle \tag{3.15}$$

by

$$|\tilde{\psi}\rangle = \sum_{a=1}^{m} \sum_{j=1}^{D_B} \tilde{\psi}_{aj} |a\rangle|j\rangle \,, \tag{3.16}$$

with $\tilde{\psi}_{aj} = \sum_i \langle i|a\rangle \psi_{ij}$ and $|a\rangle$ being the m eigenvectors of ρ_A with the largest eigenvalues w_a. The error of this approximation is

$$||\psi\rangle - |\tilde{\psi}\rangle|^2 = 1 - \sum_{a=1}^{m} w_a \equiv \Delta w \,. \tag{3.17}$$

The quantity Δw is called "truncated weight" [6] and is a measure for the error due to the truncation. For many systems, the error of the energy per site that was calculated within the truncated basis using DMRG is approximately proportional to the truncated weight [6, 89].

Using the so-called Schmidt decomposition [87,90,91] leads to a more direct derivation of the optimal truncation procedure. If we again start from Eq. (3.4), the singular value decomposition of the matrix ψ_{ij} leads to the Schmidt decomposition of $|\psi\rangle$ [6, 87, 90]:

$$|\psi\rangle = \sum_{\alpha=1}^{D_{\text{Schmidt}}} \sqrt{w_\alpha} |\alpha_A\rangle|\alpha_B\rangle \,, \tag{3.18}$$

with $|\alpha_A\rangle$ ($|\alpha_B\rangle$) being the eigenvectors of the reduced density matrix of block A (B) and w_a being the eigenvalues, i.e.,

$$\rho_A = \sum_{\alpha=1}^{D_{\text{Schmidt}}} w_\alpha |\alpha_A\rangle\langle\alpha_A| \,, \;\; \rho_B = \sum_{\alpha=1}^{D_{\text{Schmidt}}} w_\alpha |\alpha_B\rangle\langle\alpha_B| \,, \tag{3.19}$$

with $D_{\text{Schmidt}} \leq \min(D_A, D_B)$. Both reduced density matrices have the same D_{Schmidt} nonzero eigenvalues (the remaining $D_A - D_{\text{Schmidt}}$ eigenvalues for block A and $D_B - D_{\text{Schmidt}}$ eigenvalues for block B are zero). Since $0 \leq \sqrt{w_\alpha} \leq 1$, it is immediately clear, which block basis states contribute most to the state $|\psi\rangle$, namely the eigenvectors of the reduced density matrices with the largest eigenvalues. The Schmidt decomposition is furthermore enlightening because it reveals the degree of entanglement between the two blocks for the state $|\psi\rangle$. The von Neumann entropy of the reduced density matrices can be used as a measure for the entanglement [92]:

$$S_{\text{vN}} = -\sum_\alpha w_\alpha \ln w_\alpha \,. \tag{3.20}$$

If the superblock is in a product state, only one of the eigenvalues of the reduced density matrices is nonzero, i.e., equal to one for this case, and the entanglement is zero. If all reduced density matrix eigenvalues have the same value, the entanglement is maximal [87]. Keeping the m density matrix eigenvectors with the largest eigenvalues thus also means maintaining the maximum amount of entanglement between the blocks [6]. We can furthermore define the truncated entropy,

$$\Delta S = -\sum_{\alpha=m+1}^{D_{\text{Schmidt}}} w_\alpha \ln w_\alpha \,, \tag{3.21}$$

which can also be used as a measure for the accuracy of a calculation [93–95].

A reduction to m normalized density matrix eigenvectors leads to a state $|\tilde{\psi}\rangle$ which is not normalized, since $\sum_{a,j} \tilde{\psi}_{aj}^2 = 1 - \Delta w$. However, since $\Delta w \ll 1$, the estimation of the error in Eq. (3.17) still approximately holds for a normalized state

$$|\phi\rangle \equiv \frac{1}{\sqrt{1-\Delta w}} |\tilde{\psi}\rangle = \sum_{\alpha=1}^{m} \frac{\sqrt{w_\alpha}}{\sqrt{1-\Delta w}} |\alpha_A\rangle|\alpha_B\rangle \tag{3.22}$$

as a more detailed calculation shows:

$$\begin{aligned} ||\psi\rangle - |\phi\rangle|^2 &= \sum_{\alpha=1}^{m} \left(\sqrt{w_\alpha} - \frac{\sqrt{w_\alpha}}{\sqrt{1-\Delta w}} \right)^2 + \sum_{\alpha=m+1}^{D_{\text{Schmidt}}} \frac{w_\alpha}{1-\Delta w} \\ &= 2 - \Delta w - 2\sqrt{1-\Delta w} + \frac{\Delta w}{1-\Delta w} \,. \end{aligned} \tag{3.23}$$

If we now use $\sqrt{1-\Delta w} \approx 1 - \Delta w/2$ and $\Delta w/(1-\Delta w) \approx \Delta w$, we arrive at

$$||\psi\rangle - |\phi\rangle|^2 = ||\psi\rangle - \frac{1}{\sqrt{1-\Delta w}}|\tilde{\psi}\rangle|^2 \approx \Delta w\,, \tag{3.24}$$

which holds for small Δw. Δw is indeed usually very small in calculations, often much smaller than 10^{-4}.

The statement about the error is in general, however, only true if the block bases are complete before the truncation. In practice, one works with truncated bases for both blocks. This induces the so-called "environmental error" [6, 89]. The environmental error can, however, be minimized by employing the finite-size algorithm with its "sweeps" (see Sec. 3.3). Before we proceed to the description of the DMRG algorithm, we introduce the notion of "target states".

Target states: The states that are to be approximated are called target states. This can, e.g., be the ground state or the lowest energy eigenstate in some symmetry subspace. It is important to note that a target state does not need to be an energy eigenstate. It is possible to target more than one state at the same time. In this case, there are two possible strategies for how to build the reduced density matrices (with $|\psi_k\rangle$ denoting the target states):

- One might build and diagonalize the reduced density matrices separately for the individual target states and then choose several of the eigenstates of the individual density matrices as the new basis states [96].
- One can build a weighted density matrix

$$\rho = \sum_k p_k |\psi_k\rangle\langle\psi_k|\,,\ \sum_k p_k = 1\,, \tag{3.25}$$

  which is used for the calculation of the reduced density matrices (3.7). Then, the m eigenstates of the reduced density matrices with the largest eigenvalues are chosen [86]. The states $|\psi_k\rangle$ need not be orthogonal [88].

We have always used the second approach in our implementation. The weights were chosen equal, if $|\psi_k\rangle$ are energy eigenstates. For the dynamical DMRG (DDMRG) method (see Sec. 3.7), the weighting is slightly different.

3.3. Algorithms

We can now use the knowledge about the optimal basis truncation to formulate the DMRG algorithm [86]. The algorithm is divided into two parts: the "warm-up phase", also called "infinite-system algorithm", and the "finite-system" algorithm [86]. In the warm-up phase, the system (i.e., the superblock) size is gradually

increased until the desired size is reached. Then, the finite-system algorithm sets in. During the finite-system algorithm, the system size is kept constant while the basis of one block is optimized. In the following, we frequently use the notion of a block. It has already been described in the previous section that a block is a part of the system that is analyzed. In an implementation of the DMRG algorithm, a block is a collection of representations (i.e., matrices) of the Hamiltonian of the block and relevant operators. For example, operators that are needed for the construction of the interaction term between a block and a site and between both blocks are "relevant". In Sec. 3.4 the steps are described in more detail.

3.3.1. Infinite-system algorithm

The infinite-system algorithm consists of the following steps which are repeated until the desired system/superblock size L is reached [86]:

1. Start with small blocks A and B, each consisting of only one site. The Hamiltonians are H_A and H_B (with block lengths $l_A = 1$ and $l_B = 1$).

2. Enlarge both block A (length l_A) and block B (length l_B) by one site. For the spin chain with open boundary conditions (Eq. (3.1)), this step corresponds to calculating $H_A^{\text{new}} = H_A^{\text{old}} + s_{l_A}^z s_{l_A+1}^z + \frac{1}{2} s_{l_A}^+ s_{l_A+1}^- + \frac{1}{2} s_{l_A}^- s_{l_A+1}^+$, and in the same way H_B^{new}.

3. Build the superblock consisting of the enlarged blocks A and B and calculate the target states and the expectation values of interest (e.g., the ground state energy) in the superblock basis.

4. Build and diagonalize the reduced density matrices for block A and B using the states obtained in the previous step.

5. If necessary (i.e., if the block dimensions are larger than the predefined threshold value m), truncate both bases to m states and transform the block Hamiltonians as well as the block operators using the m density matrix eigenvectors which have the largest weight as new basis states.

6. Go to step 2.

The infinite-system algorithm is depicted in Fig. 3.3. A more detailed illustration of a single iteration is shown in Fig. 3.4. It is important to note that both block bases are incomplete. This means that the truncation error (measured by the truncated weight Δw, see Eq. (3.17)) is not the only error. There is an additional "environmental error" that is not captured by the truncated weight Δw [6, 89].

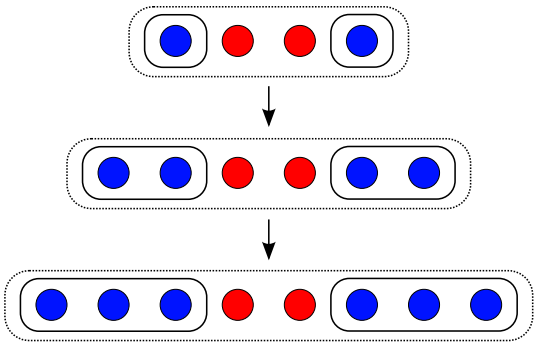

Figure 3.3.: Schematic representation of the infinite-system algorithm: Two exactly represented sites (red circles) are added to the existing blocks at each step. After that, both block bases are truncated. Blue circles indicate sites that are already included in the blocks.

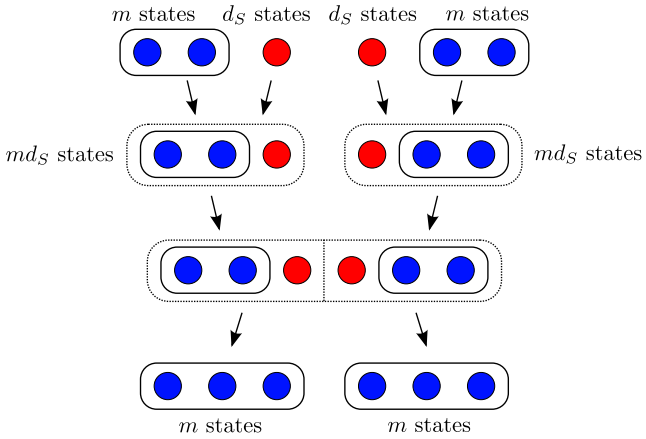

Figure 3.4.: Detailed graphical illustration of a single iteration in the infinite-system algorithm: Blocks A and B (with m basis states each) are both enlarged by one site. The two enlarged blocks then form the superblock. The states of interest and afterwards the reduced density matrices are calculated. Both block bases are finally truncated to m states again. The resulting blocks are then used for the next iteration.

3.3.2. Finite-system algorithm

The environmental error can be reduced and the block bases optimized by conducting the so-called "sweeps" of the finite-system algorithm [86]. Whereas the system (superblock) size is increased in each iteration of the infinite-system algorithm, the system size is kept constant in the finite-system algorithm. Again, two sites of the

system are represented exactly. Before starting with the finite-system algorithm, the infinite-system algorithm is iterated until the desired system length is reached. The representations of block A and B have to be saved for each block size. The finite-system algorithm consists of the following steps that are repeated until the quantities of interest have converged:

1. Enlarge block A by one site, so that the size of this block increases from l_A to $l_A + 1$. A previously stored block B with the proper number of sites is taken from memory and also enlarged by one site. "The proper number of sites" means that the total number of sites, $l_A + l_B + 2$, equals the predefined system size L.

2. Build the superblock consisting of the enlarged blocks A and B. Then, the states and expectation values of interest (e.g., the ground state energy) are calculated.

3. Build and diagonalize the reduced density matrix for block A using the (target) states obtained in the previous step.

4. Truncate the basis of block A and represent the block Hamiltonian as well as the block operators using the m density matrix eigenvectors which have the largest weight. Store the block. If block A now contains less than $L-2$ sites,[1] go to 1. Otherwise go to 5.

5. Repeat steps 1-4 with the roles of the blocks A and B interchanged, i.e., block B grows at the expense of block A. If block B has reached its maximum size, repeat steps 1-4 with block A growing again until blocks A and B have the same size. Then, a complete sweep has been conducted. For the next sweep, start with 1.

One complete sweep is depicted in Fig. 3.5. We have described the so-called two-site scheme, i.e., two sites are represented exactly before the states of the superblock are calculated. In our implementation, we have only used this scheme. Other schemes with only one exactly represented site are also possible [97, 98]. If the system possesses reflection symmetry, a reflected block A can be used as block B [86]. We have not used reflection symmetry in our implementation in order to be able to treat more complicated systems that do not possess this symmetry. Also, for systems with periodic boundary conditions a slightly different scheme is sometimes used [86]. We have always employed the scheme in which the sites are added at the center.

The m value, i.e., the maximal block basis dimension after truncation, can be increased from sweep to sweep. This is usually done in order to obtain results

[1] The sweep direction can be reversed earlier, see the note at the end of this section.

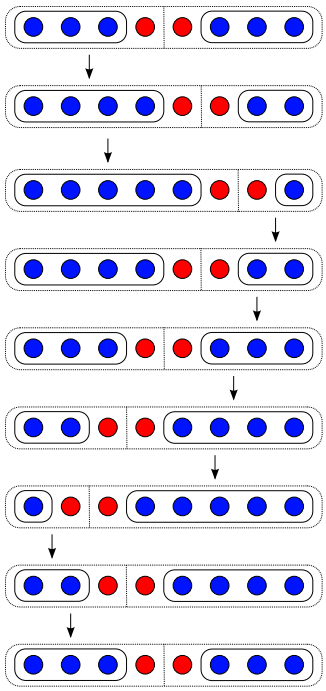

Figure 3.5.: Schematic illustration of a complete sweep in the finite-system algorithm. In each superblock configuration, two sites are represented exactly (red circles). One block is taken from the previous step while the other block is taken from memory. The truncation procedure is only applied to one block.

for different m values. This is, besides using the truncated weight as a control parameter, important for judging the convergence.

The minimal block size, i.e., the size l_A or l_B (without counting the "exact sites") at which the sweep direction is reversed (cf. Fig. 3.5), does not need to be one. In our implementation, we choose the minimal block size such that the Hilbert space dimension of this minimal block is as large as possible with the restriction of being smaller than the m value that is used for the warm-up sweep. One therefore looks for the largest $l_{\min}$ so that $(2s+1)^{l_{\min}} \leq m$ still holds. In this way, computing time can be saved.

As already mentioned in Sec. 3.2, the error of the ground state energy often depends linearly on the truncated weight so that an extrapolation to $\Delta w \to 0$ (or $m \to \infty$) can be possible. However, for systems with long-range interactions or varying coupling strengths, the truncated weight is position dependent, i.e., depends on the position of the two "exact sites". One possible solution is to sum over all truncated weights of a complete sweep to get a value that is independent of the

current position of the two exactly represented sites that are added to the blocks [99]. For most of the systems that we have investigated, an extrapolation to $\Delta w \to 0$ (or $m \to \infty$) was either not needed or not very useful.

3.4. Implementation and technical details

In this section, technical details of the algorithm and some parts of the DMRG implementation that was developed for this work are described in detail. The implementation was done in *C++* [100]. The usage of an object-oriented programming language allows for an elegant and simple handling of "blocks" and "superblocks" and makes the code very readable. As already mentioned before, the notion of blocks, sites, and the superblock is an important part of the DMRG technique. A block is simply a collection of matrices and is represented by a *C++ class*. We store the block Hamiltonian representation and the s_i^z and s_i^+ representations for all sites that are contained in the block. The matrices representing s_i^z and s_i^+ are needed for the construction of the enlarged blocks and the superblock. Since S^z symmetry is used in the program, the matrices have a special form, as is discussed later on. The block class also provides several functions which allow to add a site to the block. Furthermore, if observables other than the total energy shall be calculated, the corresponding operator representations also have to be saved. A superblock is composed of blocks and the corresponding class provides functions for the calculation of states and the reduced density matrices.

3.4.1. Operators, states, and quantum numbers

For the isotropic Heisenberg model, $S^z = \sum_{i=1}^{L} s_i^z$ commutes with the Hamiltonian. This has the consequence that all eigenstates of the Heisenberg Hamiltonian can be labeled according to the magnetic quantum number M, and the Hamiltonian of the complete system as well as the "block Hamiltonians" and the operators s_i^z, s_i^+, and s_i^- have a block structure (see Fig. 3.6). Exploiting this symmetry leads to a great reduction of memory requirements and an acceleration of the program. Furthermore, we can directly calculate energy eigenstates in S^z subspaces. It is also possible to exploit other symmetries such as mirror symmetry, spin-flip symmetry [6, 101], and the SU(2) symmetry (if S is a good quantum number) [53]. However, we have only used the S^z symmetry. Using SU(2) symmetry is very helpful, of course, but would also lead to a significantly more complicated code and was beyond the scope of this work.

We denote the M quantum number of a block state $|a\rangle$ by $M(a)$. Then, the block Hamiltonian H_A and the s_i^z operators for all sites are block diagonal, i.e., $\langle a|H_A|a'\rangle = 0$ and $\langle a|s_i^z|a'\rangle = 0$ for $M(a) \neq M(a')$. Since $s_i^- = (s_i^+)^\dagger$, there is no need to store the s_i^- operator representations. For the s_i^+ operators we have the selection rule

$\langle a|s_i^+|a'\rangle = 0$ for $M(a) \neq M(a') - 1$, which results in an off-diagonal block structure (if the basis states are ordered according to their M quantum numbers). The same considerations apply for block B, of course.

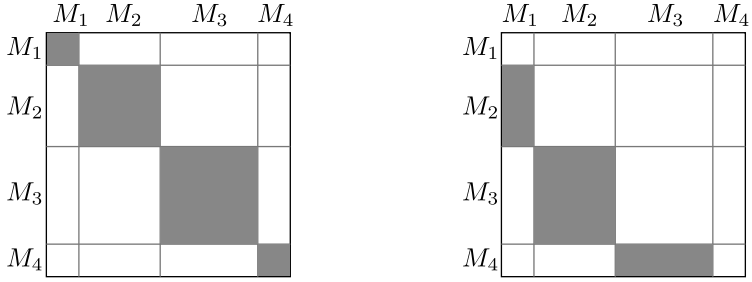

Figure 3.6.: Schematic illustration of the block structure of the operator representations. Submatrices that can contain nonzero elements are highlighted in gray. Left: Block-diagonal structure (s_i^z, $H_{A/B}$, and $\rho_{A/B}$). Right: Off-diagonal block structure with the nonzero submatrices below the main diagonal (s_i^+). The values M_i denote the M quantum numbers of the S^z subspaces and are ordered so that $M_i < M_{i+1}$.

Adding a site to a block results in an enlargement of the basis. The block structure mentioned above still exists for the enlarged blocks if the basis states are properly ordered. The addition of a site with the basis $\{|\alpha\rangle\}$ to the block A with the basis $\{|a\rangle\}$ results in the product basis $\{|a\rangle|\alpha\rangle\}$ for the enlarged block. Since M is an additive quantum number, the state $|a\rangle|\alpha\rangle$ has the quantum number $M(a) + M(\alpha)$.

If a superblock (two blocks and two sites) state

$$|\psi\rangle = \sum_{a,\alpha,\beta,b} \psi_{a\alpha\beta b}|a\rangle|\alpha\rangle|\beta\rangle|b\rangle \equiv \sum_{i,j} \psi_{ij}|i\rangle|j\rangle \quad (|i\rangle \equiv |a\rangle|\alpha\rangle,\, |j\rangle \equiv |\beta\rangle|b\rangle) \tag{3.26}$$

is an S^z eigenstate with the magnetic quantum number M_0, then this state has a block structure, since $\psi_{a\alpha\beta b} = 0$ for $M(a) + M(\alpha) + M(\beta) + M(b) \neq M_0$ (or $\psi_{ij} = 0$ for $M(i) + M(j) \neq M_0$). The reduced density matrices calculated using this state then also have a block structure. The reduced density matrix for block A is defined as $\rho_{ii'} = \sum_j \psi_{ij}\psi_{i'j}$. Nonzero entries can only occur if $M(i) + M(j) = M_0$ and $M(i') + M(j) = M_0$. Combining these conditions leads to $M(i) = M(i')$. Therefore, the reduced density matrices are also block-diagonal, provided the enlarged bases are sorted so that $M(i) \leq M(i+1)$ or $M(i) \geq M(i+1)$.

Operators, states, and the reduced density matrices can be efficiently represented by "sparse block matrices", i.e., one only saves the submatrices for which the corresponding selection rules are fulfilled (see Fig. 3.6).

3.4.2. Detailed description of the basic DMRG steps

The main steps needed for the implementation of the algorithm are:

1. Adding a site to a block,
2. forming the superblock,
3. calculating the target state(s), and
4. truncating the basis, i.e., transforming the operators according to $T^\dagger O T$, where T is represented by a rectangular $md_S \times m$ matrix.

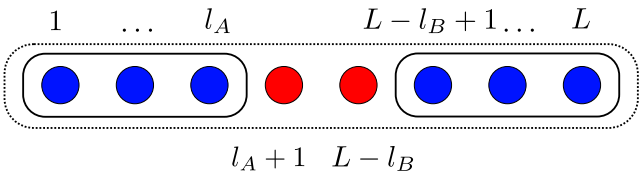

Figure 3.7.: Numbering of the sites in the superblock. For the finite-system algorithm, we have $l_A+l_B+2=L$ so that $L-l_B=l_A+2$. Otherwise, the system grows from both ends with the blocks always being connected in the warm-up phase (cf. Sec. 3.6).

These steps are described in detail in the following (for the spin chain example (3.1)):

1. Again, l_A (l_B) denotes the length of block A (B) before the addition of a site. The site operators are $s^z_{l_A+1}$ ($s^z_{L-l_B}$) and $s^+_{l_A+1}$ ($s^+_{L-l_B}$) and the site basis states are denoted by $|\alpha\rangle$ ($|\beta\rangle$). The basis states of the enlarged block A are $|i\rangle \equiv |a\rangle|\alpha\rangle$. We choose the mapping $i(a,\alpha)$ such that the states $|i\rangle$ are ordered according to the magnetic quantum number with $M(i) \leq M(i+1)\ \forall\, i$. The basis states of the enlarged block B are $|j\rangle \equiv |\beta\rangle|b\rangle$ and likewise ordered. Using the basis transformations $i(a,\alpha)$ and $j(\beta,b)$, all operator representations can then be transformed to the enlarged bases, i.e., $O_{aa'} \to O_{aa'}\delta_{\alpha\alpha'} \to O_{ii'}$ for a block operator and $O_{\alpha\alpha'} \to \delta_{aa'}O_{\alpha\alpha'} \to O_{ii'}$ for a site operator ($i' \equiv i(a',\alpha')$). The Hamiltonians of the enlarged blocks are calculated according to

$$\begin{aligned}(H_A^{\text{new}})_{i(a,\alpha)i(a',\alpha')} &= (H_A^{\text{old}})_{aa'}\delta_{\alpha\alpha'} \\ &\quad + (s^z_{l_A})_{aa'}(s^z_{l_A+1})_{\alpha\alpha'} \\ &\quad + \frac{1}{2}(s^+_{l_A})_{aa'}(s^-_{l_A+1})_{\alpha\alpha'} \\ &\quad + \frac{1}{2}(s^-_{l_A})_{aa'}(s^+_{l_A+1})_{\alpha\alpha'} \end{aligned} \tag{3.27}$$

and

$$\begin{aligned}(H_B^{\text{new}})_{j(\beta,b)j(\beta',b')} &= \delta_{\beta\beta'}(H_B^{\text{old}})_{bb'} \\ &\quad + (s^z_{L-l_B})_{\beta\beta'}(s^z_{L-l_B+1})_{bb'} \\ &\quad + \frac{1}{2}(s^+_{L-l_B})_{\beta\beta'}(s^-_{L-l_B+1})_{bb'} \\ &\quad + \frac{1}{2}(s^-_{L-l_B})_{\beta\beta'}(s^+_{L-l_B+1})_{bb'} \,. \end{aligned} \tag{3.28}$$

For systems with long-range interactions, more terms would appear.

2. For efficiency reasons, the superblock Hamiltonian is not explicitly constructed. The matrix elements of the superblock Hamiltonian can be calculated as

$$\begin{aligned}(H_{\text{super}})_{ii'jj'} &= (H_A^{\text{new}})_{ii'}\delta_{jj'} + \delta_{ii'}(H_B^{\text{new}})_{jj'} \\ &\quad + (s^z_{l_A+1})_{ii'}(s^z_{L-l_B})_{jj'} \\ &\quad + \frac{1}{2}(s^+_{l_A+1})_{ii'}(s^-_{L-l_B})_{jj'} \\ &\quad + \frac{1}{2}(s^-_{l_A+1})_{ii'}(s^+_{L-l_B})_{jj'} \,. \end{aligned} \tag{3.29}$$

Here, $l_A + 1$ is the index of the site that was added to block A, and $L - l_B$ is the index of the site that was added to block B, cf. Fig. 3.7. Again, the generalization to systems with long-range interactions or periodic boundary conditions is straightforward.

3. For the calculation of the ground state and low-lying excited states the Lanczos algorithm [102] is used. The Lanczos algorithm only needs – apart from simple vector operations – the operation $|\phi\rangle = H|\psi\rangle$ for the calculation of these states. The algorithm is described in more detail in the next subsection. For the calculation of dynamical properties via the correction vector, we use the CG algorithm [103] (see Sec. 3.7).

4. The reduced density matrices for the two blocks are defined as (represented in the bases of the enlarged blocks and for real coefficients)

$$\begin{aligned}(\rho_A)_{ii'} &= \sum_j \psi_{ij}\psi_{i'j} \\ (\rho_B)_{jj'} &= \sum_i \psi_{ij}\psi_{ij'} \,, \end{aligned} \tag{3.30}$$

where $|\psi\rangle$ is the target state. There can be more than one target state. Then the density matrices are calculated according to Eq. (3.25). These operations are simply matrix-matrix products:

$$\begin{aligned} \boldsymbol{\rho}_A &= \boldsymbol{\Psi}\boldsymbol{\Psi}^T\,, \\ \boldsymbol{\rho}_B &= \boldsymbol{\Psi}^T\boldsymbol{\Psi}\,. \end{aligned} \tag{3.31}$$

The submatrices of the density matrices are then diagonalized using a *LAPACK* routine [104], so that $\rho_A|\tilde{a}\rangle = w_{\tilde{a}}|\tilde{a}\rangle$ and $\rho_B|\tilde{b}\rangle = w_{\tilde{b}}|\tilde{b}\rangle$. The eigenvalues are ordered so that $w_{\tilde{a}} \geq w_{\tilde{a}+1}$ and $w_{\tilde{b}} \geq w_{\tilde{b}+1}$. The transformation matrices for the basis truncation of block A and B have the elements

$$T^A_{i\tilde{a}} = \langle i|\tilde{a}\rangle \;\text{ and }\; T^B_{j\tilde{b}} = \langle j|\tilde{b}\rangle\,, \tag{3.32}$$

with $1 \leq \tilde{a} \leq m$ and $1 \leq \tilde{b} \leq m$, i.e., the m eigenvectors of the reduced density matrices with the largest eigenvalues are the columns of the $md_S \times m$ transformation matrices. The block Hamiltonians and block operators are transformed to the truncated bases according to $\mathbf{O} := \mathbf{T}^T\mathbf{O}\mathbf{T}$.[2] Of course, all these operations have to be performed such that the block structures are maintained, and the lists with the corresponding M quantum numbers have to be updated.

3.4.3. Superblock diagonalization: Lanczos procedure and matrix-vector product

For the calculation of the ground state or low-lying excited states (and the corresponding eigenvalues), we use the Lanczos algorithm [102]. (An alternative, which is also well suited for this purpose, is the Davidson algorithm [86].) The Lanczos algorithm is an effective numerical method for the calculation of extremal eigenvalues and the corresponding eigenvectors of a matrix, e.g., the representation of a Hamiltonian H. Starting with an initial vector $|\phi_0\rangle$, the Lanczos algorithm generates a Krylov subspace $K_i(H, |\phi_0\rangle) \equiv \text{span}\,\{|\phi_0\rangle, H|\phi_0\rangle, H^2|\phi_0\rangle, H^3|\phi_0\rangle, \ldots, H^{i-1}|\phi_0\rangle\}$. Within this subspace, H is represented by an $i \times i$ matrix which is called the Lanczos matrix. The extremal eigenvalues of this matrix are approximations of the extremal eigenvalues of H. These approximations are already very good for a value of i that is much (often several orders of magnitude) smaller than the dimension of the underlying Hilbert space.

The success of the Lanczos algorithm can be understood by examining the power method [105]. This method consists of a repeated application of the Hamiltonian to

[2] ":=" means that the right hand side is assigned to the left hand side.

a trial state $|\phi_0\rangle$, i.e., one calculates $H^k|\phi_0\rangle$. An expansion of this state with respect to the eigenstates $|n\rangle$ of H yields

$$H^k|\phi_0\rangle = \sum_n E_n^k \langle n|\phi_0\rangle |n\rangle \,. \tag{3.33}$$

For large k, the eigenstate that belongs to the eigenvalue with the largest absolute value gets the largest weight, i.e., the method converges for $k \to \infty$ towards this state, apart from a normalization factor. In the Lanczos procedure one also keeps the vectors from previous steps. This leads to a much faster convergence of the Lanczos algorithm compared to the power method [106].

The Lanczos algorithm is very easy to implement since the orthonormalized basis vectors of the Krylov subspace can be generated using a simple three-term recurrence relation so that only three states have to be saved [102]:

$$\beta_{i+1}|\phi_{i+1}\rangle = H|\phi_i\rangle - \alpha_i|\phi_i\rangle - \beta_i|\phi_{i-1}\rangle \,, \;\; \alpha_i = \langle\phi_i|H|\phi_i\rangle \,. \tag{3.34}$$

Furthermore, the matrix (the "Lanczos matrix" $\mathbf{L}_i$) generated by this procedure after i steps (the projection of H onto the Krylov subspace) is tridiagonal:

$$\mathbf{L}_i = \begin{pmatrix} \alpha_0 & \beta_1 & 0 & \cdots & & 0 \\ \beta_1 & \alpha_1 & \beta_2 & & & \\ 0 & \beta_2 & \alpha_2 & \ddots & & \\ \vdots & & \ddots & \ddots & \beta_{i-2} & \\ & & & \beta_{i-2} & \alpha_{i-2} & \beta_{i-1} \\ 0 & & & & \beta_{i-1} & \alpha_{i-1} \end{pmatrix} . \tag{3.35}$$

Our implementation of the algorithm follows Ref. [102], starting with a normalized initial vector $|\phi_0\rangle$ and $i = 0$ ($|\phi_{-1}\rangle \equiv 0$, $\beta_0 \equiv 0$). The following steps are carried out until convergence[3] is reached:

1. $|\tilde{\phi}_i\rangle = H|\phi_i\rangle - \beta_i|\phi_{i-1}\rangle$.
2. $\alpha_i = \langle\tilde{\phi}_i|\phi_i\rangle$. The tridiagonal Lanczos matrix $\mathbf{L}_i$ (see Eq. (3.35)) is updated and diagonalized using a *LAPACK* routine. If $|E_i^{\text{Lanczos}} - E_{i-1}^{\text{Lanczos}}| < \epsilon_1$, stop. E_i^{Lanczos} is the smallest eigenvalue of the Lanczos matrix $\mathbf{L}_i$.
3. $|\tilde{\phi}_i\rangle := |\tilde{\phi}_i\rangle - \alpha_i|\phi_i\rangle$ and furthermore explicit reorthogonalization against previously calculated Lanczos vectors and other vectors, if needed.

[3] The convergence criteria in our implementation are $|E_i^{\text{Lanczos}} - E_{i-1}^{\text{Lanczos}}| < \epsilon_1$ or $|\beta_{i+1}| < \epsilon_2$ ($\epsilon_1 > 0$ and $\epsilon_2 > 0$), where E_i^{Lanczos} is the smallest eigenvalue of the Lanczos matrix $\mathbf{L}_i$. We have usually chosen $\epsilon_1 = 10^{-10}$ and $\epsilon_2 = 10^{-9}$.

4. $\beta_{i+1} = \sqrt{\langle\tilde{\phi}_i|\tilde{\phi}_i\rangle}$. If $|\beta_{i+1}| < \epsilon_2$, stop.

5. $|\phi_{i+1}\rangle = \frac{1}{\beta_{i+1}}|\tilde{\phi}_i\rangle$.

6. $i := i + 1$ and go to 1.

Although in principle only three vectors have to be saved, we save all previously calculated Lanczos vectors in our implementation. This leads to a simple construction of the (approximate) eigenstates of H. If only three vectors are saved, one has to start a second run of the algorithm to construct the eigenvectors [106]. The three-term recursion relation in Eq. (3.34) leads to orthogonal states only in exact arithmetics. On a computer, most real numbers cannot be represented exactly. This leads to a loss of orthogonality of the Lanczos vectors after some iterations [107]. We explicitly orthogonalize (see step 3 of the algorithm) the newly created Lanczos vector against all previously created ones after some iterations (usually 10).

If one has a good guess for the initial vector $|\phi_0\rangle$, as is the case for the finite-system DMRG algorithm (see subsection 3.4.5), one often needs less than 10 iterations of the Lanczos algorithm to obtain converged results. If one does not have a good guess, it is convenient to use a normalized initial vector with random entries [107]. With a random vector as the initial state, usually $\mathcal{O}(100)$ Lanczos iterations are needed to get converged results.

In the form presented above, it is not possible to resolve degenerate eigenstates of H [57, 108]. We have used the following approach to overcome this problem [57]: First, we calculate the ground state of H. For the calculation of the next state we again start the Lanczos algorithm and explicitly orthogonalize the initial vector against the previously calculated ground state. Additionally, in each iteration (see step 3 of the algorithm) we explicitly orthogonalize the current Lanczos vector against the ground state. For the calculation of a third state, we proceed similarly and orthogonalize against the previously calculated eigenstates, etc. In this way, it is easily possible to calculate eigenstates of degenerate eigenvalues using the Lanczos algorithm. Another possibility to resolve degeneracies is the band Lanczos method [108] which we have, however, not tested in our implementation.

Apart from simple vector operations, the Lanczos algorithm requires only the application of H to a state. For the DMRG algorithm, this has the advantage that the superblock Hamiltonian H_{super} does not need to be explicitly constructed as a matrix. Instead, the matrix-vector product can be traced back to simple matrix-matrix products [109]. We start from the form of the superblock Hamiltonian as shown in Eq. (3.29). The structure of the superblock Hamiltonian is:

$$H_{\text{super}} = \sum_k A_k B_k \,, \tag{3.36}$$

where A_k denotes operators acting on the block A and B_k operators acting on block B. The product of H_{super} with the state $|\psi\rangle$ can then be written as

$$\psi'_{ij} \equiv \langle i,j|H_{\text{super}}|\psi\rangle = \sum_k \sum_{i',j'} (A_k)_{ii'} (B_k)_{jj'} \psi_{i'j'} \,, \tag{3.37}$$

where $|i\rangle$ denotes the basis states of the left block and $|j\rangle$ those of the right block. The terms $\sum_{i',j'} (A_k)_{ii'} (B_k)_{jj'} \psi_{i'j'}$ are matrix-matrix products [109]:

$$\mathbf{\Psi'} = \sum_k \mathbf{A}_k \left(\mathbf{\Psi} \mathbf{B}_k^T \right) \,, \tag{3.38}$$

where $\mathbf{\Psi'}$ and $\mathbf{\Psi}$ denote the representations of state vectors in the superblock product basis, $\mathbf{A}_k$ is the representation of the operator A_k in the current basis of block A, and $\mathbf{B}_k$ is the representation of the operator B_k in the current basis of block B. Therefore, the product of the superblock Hamiltonian with a superblock state can be traced back to simple matrix-matrix products with a cost of $\mathcal{O}(m^3 d_S^3)$. The eigenstate calculation is usually by far the most time-consuming part of the DMRG algorithm so that the overall numerical complexity of DMRG as described here is $\mathcal{O}(m^3 d_S^3)$, too. The reformulation of the operation $H_{\text{super}}|\psi\rangle$ as described above allows for the usage of the *BLAS* library [110]. As previously noted, the matrices all have a special block structure due to the S^z symmetry, so that the matrix product is a product between block-sparse matrices and the *BLAS* routines are used on the level of the dense submatrices. At this point, it is also possible to parallelize the algorithm using *OpenMP*. This can be done by hand or simply by linking the program with the highly optimized *BLAS* routines of the *MKL* [109]. We have used the latter approach in our program. However, since the dense submatrices are rather small, it is not advisable to run the program on many cores for a single calculation. We have normally used not more than 4 CPU cores for a parallel calculation. The operation $H_{\text{super}}|\psi\rangle$ can be further unrolled by not explicitly constructing the enlarged blocks, see [6]. This probably leads to a faster, but also more complicated code. We have implemented the simpler variant as described above.

3.4.4. Calculation of expectation values

The expectation value of some operator O, which only acts on either the left or the right block, such as the local magnetization in a spin chain can easily be calculated using DMRG. For the calculation of the expectation value with respect to $|\psi\rangle$ (e.g., the ground state or an excited state), which is represented in the superblock basis, we need the representation of the operator in the current block basis, i.e., we need the matrix elements $O_{ii'}$. We assume here that the operator acts on the left block.

Then the expectation value is calculated as

$$\langle\psi|O|\psi\rangle = \sum_{i,i',j} \psi_{ij} O_{ii'} \psi_{i'j} \,. \tag{3.39}$$

The generalization to an operator acting on the right block or to nonlocal operators as needed for, e.g., correlation functions is straightforward, see [6].

3.4.5. Target state transformation

In the finite-size algorithm, the system is only changed insofar as the position, at which the exactly represented sites are added, is moving (cf. Fig. 3.5). It is possible to transform the target states from one step to the next step using a transformation that was developed by White in 1996 [111]. This transformation does not lead to an exact eigenstate of the superblock Hamiltonian, but is still very useful in most cases [6]. If one has a good starting vector for the Lanczos algorithm, the number of steps needed for convergence can be greatly reduced. Since the superblock diagonalization is the most time-consuming step in the whole algorithm, the use of White's target state transformation usually accelerates the program by a factor of about 10. For the wave function transformation, the transformation matrices (see Eq. (3.32)) for all steps and for both blocks have to be saved.

Up to now, the notation was as follows. The basis states of block A were denoted as $|a\rangle$ and those of block B as $|b\rangle$. The site that is added to block A has the basis states $|\alpha\rangle$, and the site that is added to block B has the basis $|\beta\rangle$. The bases of the enlarged blocks were denoted as $\{|a\rangle|\alpha\rangle\} = \{|i\rangle\}$ and $\{|\beta\rangle|b\rangle\} = \{|j\rangle\}$. Following Refs. [6,111], we now slightly change the notation and introduce the position dependence of the bases. Let the indices (or positions) of the sites that are added to the blocks A and B be $l+1$ and $l+2$ (i.e., $l \equiv l_A$ compared to Fig. 3.7). We then change the basis notation to $|a_l\rangle$, $|\sigma_{l+1}\rangle$ (instead of $|\alpha\rangle$), $|\sigma_{l+2}\rangle$ (instead of $|\beta\rangle$), and $|b_{l+3}\rangle$.

If we have calculated the state $|\psi\rangle$ with the coefficients

$$\psi_{a_l \sigma_{l+1} \sigma_{l+2} b_{l+3}} = \langle a_l \sigma_{l+1} \sigma_{l+2} b_{l+3} | \psi \rangle \tag{3.40}$$

at some point in the algorithm and if the sweep direction is from left to right (i.e., the size of block A is increased), we can use these coefficients to get a good approximation of the state for the next step. At the next step, the coefficients take the form $\langle a_{l+1} \sigma_{l+2} \sigma_{l+3} b_{l+4} | \psi \rangle$. Since the bases $\{|a_l\rangle\}$ and $\{|b_{l+3}\rangle\}$ are incomplete, we can only find an approximate transformation:

$$\langle a_{l+1} \sigma_{l+2} \sigma_{l+3} b_{l+4} | \psi \rangle \approx \sum_{a_l, \sigma_{l+1}, b_{l+3}} \langle a_{l+1} | a_l \sigma_{l+1} \rangle \langle \sigma_{l+3} b_{l+4} | b_{l+3} \rangle \langle a_l \sigma_{l+1} \sigma_{l+2} b_{l+3} | \psi \rangle \,. \tag{3.41}$$

The coefficients $\langle a_{l+1}|a_l\sigma_{l+1}\rangle$ are the matrix elements of the transformation operator $T^{A_{l+1}}$ at the point where the basis is truncated from $\{|a_l\rangle|\sigma_{l+1}\rangle\}$ to $\{|a_{l+1}\rangle\}$, i.e., from the previous step. Similarly, the coefficients $\langle\sigma_{l+3}b_{l+4}|b_{l+3}\rangle$ are the elements of a transformation matrix that has been used at an earlier step to truncate the basis of block B after it was enlarged by one site. The wave function transformation can be traced back to matrix-matrix products. First, one calculates

$$\psi^{\mathrm{tmp}}_{a_{l+1}j_{l+2}} \equiv \sum_{i_{l+1}} T^{A_{l+1}}_{i_{l+1}a_{l+1}} \psi_{i_{l+1}j_{l+2}}\,, \tag{3.42}$$

where $i_{l+1} = i_{l+1}(a_l, \sigma_{l+1})$ and $j_{l+2} = j_{l+2}(\sigma_{l+2}, b_{l+3})$. Then, one calculates

$$\psi^{\mathrm{approx}}_{i_{l+2}j_{l+2}} \equiv \sum_{b_{l+3}} \psi^{\mathrm{tmp}}_{i_{l+2}b_{l+3}} T^{B_{l+3}}_{j_{l+2}b_{l+3}}\,, \tag{3.43}$$

where $i_{l+2} = i_{l+2}(a_{l+1}, \sigma_{l+2})$ and again $j_{l+2} = j_{l+2}(\sigma_{l+2}, b_{l+3})$.

If the sweep direction is from right to left, i.e., block B grows at the expense of block A, the transformation is given by

$$\langle a_{l-4}\sigma_{l-3}\sigma_{l-2}b_{l-1}|\psi\rangle \approx \sum_{a_{l-3},\sigma_{l-1},b_l} \langle a_{l-4}\sigma_{l-3}|a_{l-3}\rangle\langle b_{l-1}|\sigma_{l-1}b_l\rangle\langle a_{l-3}\sigma_{l-2}\sigma_{l-1}b_l|\psi\rangle\,, \tag{3.44}$$

which can again easily be formulated using two successive products of matrices.

3.5. Connection to matrix product states

For a spin-s system with L spins, a general state $|\psi\rangle$ can be written as

$$|\psi\rangle = \sum_{\sigma_1,\sigma_2,\ldots,\sigma_L} \psi_{\sigma_1\sigma_2\ldots\sigma_L}|\sigma_1\sigma_2\ldots\sigma_L\rangle\,, \tag{3.45}$$

where $|\sigma_l\rangle$ denotes the local basis states of the spin at position l. For the calculation of the ground state one has to find the minimum of $\langle\psi|H|\psi\rangle/\langle\psi|\psi\rangle$ (or solve the eigenvalue equation) in a $(2s+1)^L$-dimensional parameter space. The idea of matrix product states is to rewrite the coefficients $\psi_{\sigma_1\sigma_2\ldots\sigma_L}$ of the state $|\psi\rangle$ as a product of matrices [112]:

$$|\psi_{\mathrm{MP}}\rangle = \sum_{\sigma_1,\sigma_2,\ldots,\sigma_L} \mathbf{M}^{\sigma_1}\mathbf{M}^{\sigma_2}\cdots\mathbf{M}^{\sigma_L}|\sigma_1\sigma_2\ldots\sigma_L\rangle\,, \tag{3.46}$$

where $\mathbf{M}^{\sigma_l}$ are $m\times m$ matrices, except for $l = 1$ and $l = L$, where we have $1\times m$ and $m\times 1$ matrices, so that the product of the matrices results in a scalar. Such a state is

called a matrix product state (MPS). Now we have $m^2 \cdot (2s+1) \cdot L$ free parameters.[4] If we choose m large enough, any state of the system can be written exactly in matrix product form. If m is, however, not large enough to exactly represent an arbitrary state, such a matrix product state can be used as a variational ansatz and the energies calculated with this ansatz always lie above the true ground state energy. For some Hamiltonians (not for Heisenberg systems as considered in this chapter), it is even possible to construct the exact ground state with $m = 2$ [112].

It was first noted in 1995 that there exists a connection between DMRG and matrix product states [113]. DMRG consists of enlargements of the blocks and a subsequent basis truncation: We have a block with m basis states $|a_l\rangle$ which is enlarged by one site, so that the enlarged block has md_S basis states $|i_l\rangle \equiv |a_l\rangle|\sigma_{l+1}\rangle$, and after the calculation of, e.g., the ground state and the reduced density matrix, the basis is truncated to m states again according to

$$|a_{l+1}\rangle = \sum_{a_l,\sigma_{l+1}} T^{A_{l+1}}_{a_{l+1}a_l\sigma_{l+1}} |a_l\rangle|\sigma_{l+1}\rangle \,. \tag{3.47}$$

The next DMRG iteration leads to

$$|a_{l+2}\rangle = \sum_{a_{l+1},\sigma_{l+2}} T^{A_{l+2}}_{a_{l+2}a_{l+1}\sigma_{l+2}} \sum_{a_l,\sigma_{l+1}} T^{A_{l+1}}_{a_{l+1}a_l\sigma_{l+1}} |a_l\rangle|\sigma_{l+1}\rangle|\sigma_{l+2}\rangle \,, \tag{3.48}$$

etc. The summation over a_{l+1} corresponds to a product of matrices, so that the DMRG procedure leads to states with coefficients that are obtained as products of matrices. This has led to DMRG algorithms which explicitly use matrix product states and operate strictly variationally on the space of these states [112]. For the traditional "two-site" DMRG, as it has been described earlier in this chapter (section 3.3) and used for this work, it can be shown that the approximation of the ground state energy is not guaranteed to decrease from iteration to iteration [6, 114, 115]. This can be seen in calculations if one compares the energies in a particular sweep and investigates inhomogeneous systems, but at least the convergence from sweep to sweep turns out to be rather smooth in practice. In contrast to this, in the single-site DMRG the energy is guaranteed to decrease from iteration to iteration [6, 97, 116]. However, two-site DMRG seems to be better suited to avoid being trapped in metastable states [117].

The MPS formulation of DMRG has clear advantages for the calculation of spectral functions, as pointed out in Refs. [118, 119]. One only needs to simultaneously target real and imaginary part of the correction vector and not additionally the states $|0\rangle$ and $|B\rangle$ as in the standard DMRG approach (see Sec. 3.7). Also, the MPS formulation allows to compute, e.g., the overlap between wave functions obtained in

[4] Strictly speaking we have only $m^2(2s+1)(L-2)+2m(2s+1)$ parameters because of the smaller matrices at the positions $l = 1$ and $l = L$.

different calculations [120]. With traditional DMRG, which has been used for this work, this is only possible for wave functions that are targeted simultaneously in the same calculation.

3.6. General spin lattices

Up to now we have described the DMRG steps for a simple spin chain with open boundary conditions and nearest-neighbor interactions (see Eq. (3.1)). In this section we briefly describe how to use the DMRG algorithm for general Heisenberg systems with Hamiltonians of the form

$$H = \sum_{i<j} J_{ij} \vec{s}_i \cdot \vec{s}_j \,. \tag{3.49}$$

We can rewrite this equation as

$$H = \sum_i \vec{s}_i \cdot \sum_{k>0} J_{i,i+k} \vec{s}_{i+k} \,, \tag{3.50}$$

so that we can see that every Heisenberg system can be treated as a one-dimensional chain with long-range interactions. The DMRG algorithm can then be applied to such a chain. This is the usual way DMRG is applied to systems that are not one-dimensional [84,121]. We have also followed this way in this work. There exist other possibilities for, e.g., the Heisenberg model on the square lattice (see [122–124]), but the standard approach with a mapping to a chain seems to be the method that is most often used [6, 125, 126]. However, DMRG has fundamental difficulties when applied to systems that are not one-dimensional or quasi-one-dimensional [6]. Furthermore, DMRG is most accurate when applied to systems with open boundary conditions. For one-dimensional spin chains, White found out that if m density matrix states are kept for a system with open boundary conditions, m^2 states are needed to achieve the same accuracy for the system with periodic boundary conditions [86]. For systems with periodic boundary conditions, the truncated weight is usually much larger than for a system with open boundary conditions (see Sec. 3.8). For two-dimensional systems with a dimension of $L \times L$, Liang and Pang found out that the number of kept density matrix eigenstates has to grow exponentially with L in order to approximately keep the accuracy constant [127]. For two-dimensional systems with periodic boundary conditions in both directions, DMRG is clearly at or beyond its limits [128]. However, often an application of DMRG to complicated systems still makes sense since it is possible to give error estimates based on the truncated weight and calculations for various m values.

There are extensions based on the variational formulation with matrix product states for two-dimensional systems [129] and for one-dimensional systems with periodic boundary conditions [130] that overcome some of these fundamental difficulties.

However, compared to standard DMRG, the numerical complexity of these techniques is much larger. Recently developed techniques such as correlator product states (CPS) in combination with variational Monte Carlo seem to be a promising alternative [131, 132].

The question remains how to map a system to a one-dimensional chain (i.e., how to number the spins) to get the best results with the DMRG method. Long-range interactions seem to decrease the accuracy of DMRG so that it is reasonable to number the spins such that long-range interactions are minimized as far as possible. We come back to this question in chapter 4. Furthermore, it is not clear how to grow the system during the warm-up phase (cf. Fig.3.3). In our implementation, we grow the system from both ends and treat the spin interactions according to the coupling matrix J_{ij} with the exception that we always explicitly connect both blocks with an antiferromagnetic interaction of strength one. Otherwise, we would have for, e.g., a one-dimensional system with only nearest-neighbor interactions two isolated blocks in the warm-up phase, and the superblock would not resemble the "final" system.

3.7. Dynamical DMRG

It is also possible to calculate zero-temperature dynamical correlation functions using extensions of the DMRG technique. There already exists an extension of the Lanczos algorithm to calculate dynamical correlation functions [133]. The idea of the Lanczos approach is to rewrite the dynamical correlation function in the form of a continued fraction. This technique can be built into the DMRG algorithm [134], but the accuracy is rather limited for many systems [7]. We have implemented and used the more accurate, but also more time-consuming dynamical DMRG (DDMRG) technique [7, 8, 135]. We do not distinguish between the DDMRG and the correction vector DMRG (which is sometimes done in the literature, see [6, 8]) in this work, since the differences are very small and we use parts of both variants in our implementation.

In the following, we focus on the calculation of zero-temperature dynamical correlation functions such as

$$G_{A,B}(\omega + i\eta) = -\frac{1}{\pi}\langle 0|A^\dagger \frac{1}{E_0 + \omega + i\eta - H} B|0\rangle\,, \tag{3.51}$$

where $|0\rangle$ denotes the ground state with the energy E_0. A and B are some transition operators, e.g., the spin operators for inelastic neutron scattering (INS, see Sec. 2.3.2). For the comparison to a spectroscopic experimental method such as

INS, the important part of this function is the imaginary part

$$\begin{aligned} \operatorname{Im} G_{A,B}(\omega + i\eta) &= \frac{1}{\pi}\langle A| \frac{\eta}{(E_0 + \omega - H)^2 + \eta^2} |B\rangle \\ &= \sum_n \langle A|n\rangle\langle n|B\rangle \delta_\eta(\omega + E_0 - E_n)\,, \end{aligned} \tag{3.52}$$

where $\delta_\eta(x) = (\eta/\pi)/(x^2 + \eta^2)$ is the Lorentzian function with $\lim_{\eta\to 0} \delta_\eta(x) = \delta(x)$,[5] $|A\rangle \equiv A|0\rangle$, and $|B\rangle \equiv B|0\rangle$. E_n denotes the energy eigenvalue belonging to the eigenstate $|n\rangle$. Determining the matrix elements $\langle A|n\rangle$ and $\langle n|B\rangle$ by directly calculating the excited states $|n\rangle$ using standard DMRG [136] is possible only for low energies or simple systems since all energy eigenstates up to the desired state have to be included as target states in the reduced density matrix. Using many target states, however, decreases the accuracy of a DMRG calculation [86]. Furthermore, states that do not contribute to the dynamical correlation function would possibly still be targeted. The DDMRG method solves these problems and requires only four target states.

The basic idea of the DDMRG method is a reformulation of equation (3.52) using the so-called correction vector, which is defined as [7]

$$|C(\omega + i\eta)\rangle = \frac{1}{E_0 + \omega + i\eta - H}|B\rangle\,. \tag{3.53}$$

If one splits the correction vector into $|C(\omega + i\eta)\rangle = |C^r(\omega + i\eta)\rangle + i|C^i(\omega + i\eta)\rangle$ with

$$|C^i(\omega + i\eta)\rangle = \frac{-\eta}{(E_0 + \omega - H)^2 + \eta^2}|B\rangle \tag{3.54}$$

and

$$|C^r(\omega + i\eta)\rangle = \frac{H - E_0 - \omega}{\eta}|C^i(\omega + i\eta)\rangle\,, \tag{3.55}$$

a direct calculation of $\operatorname{Im} G_{A,B}(\omega + i\eta)$ is possible as [8, 137]

$$\operatorname{Im} G_{A,B}(\omega + i\eta) = -\frac{1}{\pi}\langle A|C^i(\omega + i\eta)\rangle\,. \tag{3.56}$$

Within the reduced DMRG basis, $|C^i(\omega + i\eta)\rangle$ is calculated as the solution of the linear equation system

$$[(E_0 + \omega - H)^2 + \eta^2]|C^i(\omega + i\eta)\rangle = -\eta|B\rangle\,. \tag{3.57}$$

[5] In practice, one always runs calculations with a finite η, of course.

Solving this linear equation system is equivalent to minimizing the functional [8,138]

$$\begin{aligned} W_{B,\eta}(\omega,\psi) &= \langle\psi|[(E_0+\omega-H)^2+\eta^2]|\psi\rangle \\ &\quad +\eta\langle B|\psi\rangle+\eta\langle\psi|B\rangle\,. \end{aligned} \tag{3.58}$$

There are many possibilities for solving the linear equation system (3.57) or minimizing the functional, see, e.g., [139–141]. We have used a simple conjugate gradient (CG) algorithm without preconditioning as described in Refs. [103, 138] for the calculation of the correction vector. The CG method is an effective numerical method for solving symmetric positive linear equation systems. Like the Lanczos method, it also belongs to the Krylov subspace methods [102] and only needs the operation $|\phi\rangle = [(E_0+\omega-H)^2+\eta^2]|\psi\rangle$ (besides simple vector operations such as addition, etc.). Since we only have an approximation of H, but not of H^2, in the current (reduced) superblock basis, we make the approximation [8]

$$[(E_0+\omega-H)^2]_{\text{eff}} \approx (E_0+\omega-H_{\text{eff}})^2\,. \tag{3.59}$$

Here, the subscript "eff" means the representation of the operator in the reduced superblock basis. The construction of $[(E_0+\omega-H)^2]_{\text{eff}}$ is numerically much too expensive for, e.g., Heisenberg systems with many spins. However, the squaring of a matrix leads to a slowdown of the convergence [6]. The convergence strongly depends on the condition number of the matrix (the representation of the operator on the left hand side of Eq. (3.57), to be more precise). The condition number (of a normal matrix) is defined as $\kappa = |\lambda_{\max}|/|\lambda_{\min}|$, where $\lambda_{\max}$ is the eigenvalue of the matrix with largest and $\lambda_{\min}$ the eigenvalue with smallest absolute value, respectively [142]. A smaller condition number usually leads to a better convergence of the algorithm, which means that squaring the matrix slows down the convergence. Here, preconditioning techniques might help [102, 142]. We have not used preconditioning, but have employed the wave function transformation (see Sec. 3.4.5) for the correction vector to speed up the algorithm.[6] A good guess for the solution of the linear equation system leads to less iterations of the CG algorithm that are needed for convergence. It is also clear that the convergence strongly depends on the broadening parameter η. The limit $\eta \to \infty$ would lead to a condition number of

[6] Here, a minor difficulty emerges: Let $|0'\rangle$ be the state that is obtained as the transformation of the ground state from the previous DMRG step. This state is then used as a starting point for the Lanczos algorithm and the "correct" ground state $|0\rangle$ is obtained. Since the phase of the ground state does not matter, it might be that $\langle 0'|0\rangle \approx -1$, i.e., the phase is changed in the Lanczos calculation. If the imaginary part of the correction vector is also transformed, one has to take care of this phase change, since $|0\rangle$ and not $|0'\rangle$ is used for the linear equation system that is solved. We deal with this problem by checking if the functional (3.58) is smaller for $|C^{i'}(\omega+i\eta)\rangle$ or $-|C^{i'}(\omega+i\eta)\rangle$, where $|C^{i'}(\omega+i\eta)\rangle$ denotes the transformed imaginary part of the correction vector from the previous DMRG step.

one and thus optimal convergence. Therefore, the larger the value of η, the better is the convergence of the CG algorithm.

The target states for the reduced density matrix are $|0\rangle$, $|B\rangle$, $|C^i(\omega + i\eta)\rangle$, and $|C^r(\omega + i\eta)\rangle$ [7, 8]. Although not needed for the calculation of the imaginary part of the dynamical correlation function, $|C^r(\omega + i\eta)\rangle$ is also included in order to minimize the error in the calculation of (3.59) [6, 8]. As in Ref. [140], we weight the ground state with 0.4 and each of the other states with 0.2 in the density matrix (cf. Eq. (3.25)). However, only the ground state is normalized. We normalize the other states when we include them in the density matrix. Otherwise, the density matrix (3.25) would not have trace one.

If the correction vector has been calculated, the value of the dynamical correlation function for a specific frequency can be calculated using equation (3.56). If $A = B$, we can also use the functional (3.58). Inserting $|C^i(\omega + i\eta)\rangle$ leads to

$$W_{B,\eta}(\omega, C^i) = \eta \langle B|C^i(\omega + i\eta)\rangle = -\pi\eta \operatorname{Im} G_{B,B}(\omega + i\eta)\,. \tag{3.60}$$

Using the functional for the calculation of the dynamical correlation function should lead to a smaller error than using equation (3.56) if we have only approximately calculated the correction vector [8]. If the error in the calculation of the correction vector is ϵ, the error in the dynamical correlation function is also of order ϵ if Eq. (3.56) is used. In contrast, if Eq. (3.60) is used, the error is only of order ϵ^2 [8]. However, this statement is not strictly true if one uses the approximation (3.59). For the systems that we have analyzed with DDMRG, we have found no significant differences between the two approaches or the differences did not matter. We have always calculated both values for dynamical correlation functions with $A = B$.

Summarizing, the DDMRG method consists of the following steps that are carried out for fixed ω and η within the (reduced) superblock space, i.e., in step 2 of the algorithm described in Sec. 3.3.2: The ground state $|0\rangle$ and the ground state energy E_0 are calculated using the Lanczos method as described in Sec. 3.4.3. The state $|B\rangle$ is determined by applying the operator B to the ground state: $|B\rangle = B|0\rangle$. $|C^i(\omega + i\eta)\rangle$ is calculated using the CG algorithm and $|C^r(\omega + i\eta)\rangle$ is obtained via Eq. (3.55). Then, the reduced density matrix is formed using these four states.

It has to be noted here that the procedure has to be repeated separately for every frequency ω. For this reason, the DDMRG method is numerically very expensive. Also, depending on the value of ω, sometimes more than 1000 CG steps are needed for convergence so that the calculation of the correction vector is usually numerically much more demanding than the calculation of the ground state. However, the complete independence of the calculations for different values of ω gives rise to a trivial parallelization of the program. Therefore, DDMRG is very well suited for high-performance computers.

3.8. Basic properties of the algorithm and tests

In the following, we test the DMRG program for several antiferromagnetic Heisenberg systems with the coupling constant J set to one in all cases. The goal of this section is to study the basic properties of the DMRG algorithm as well as the reliability and accuracy of our DMRG implementation. For these purposes we apply the DMRG program to several "test systems" for which numerically exact or analytical results are available.

3.8.1. Haldane gap

As a first test of our DMRG program we calculate the lowest energy eigenvalues of $s = 1$ spin chains with open boundary conditions and of various lengths. The $s = 1$ chain is of special interest since Haldane conjectured in 1983 that a gap between the ground state energy and the energy of the first excited state exists in the thermodynamic limit [143, 144]. However, for finite systems with open boundary conditions, the gap between the lowest $M = 0$ and the lowest $M = 1$ energy eigenvalue goes to zero when the chain length is increased. Instead, the Haldane gap opens between the lowest $M = 1$ and $M = 2$ energy eigenvalues [145, 146]. This behavior is attributed to so-called boundary excitations in open $s = 1$ chains so that the first "bulk excitation" occurs in the $M = 2$ subspace [5,145–148]. White and Huse have obtained the value $\Delta_H = 0.41050(2)$ for the Haldane gap of the infinite $s = 1$ chain using highly accurate DMRG calculations [146]. Using our DMRG program we have calculated the lowest energy eigenvalues in the $M = 0$, $M = 1$, and $M = 2$ subspaces for open $s = 1$ chains. These eigenvalues are called E_0, E_1, and E_2 in the following. Based on the above picture we expect $E_1 - E_0$ to go to zero and $E_2 - E_1$ to go to 0.4105 when the chain length N is increased. The results are shown in Fig. 3.8 and fully confirm the expectations.

3.8.2. Ground state energy of the infinite $s = 1/2$ chain

As a second test (similar to Ref. [140]) we compute the ground state energy per spin, $E_0(N)/N$, of periodic $s = 1/2$ chains with different lengths N. The Bethe ansatz allows for an exact calculation of this quantity for the infinite chain and the result is $e_0 = \frac{1}{4} - \ln 2$ [149, 150]. Furthermore, an exact formula for the leading finite-size corrections of the ground state energy per spin is known [151, 152]:

$$\left| \frac{E_0(N)}{N} - e_0 \right| = \frac{\pi^2}{12N^2} \left(1 + \mathcal{O}\left(\frac{1}{(\ln N)^2} \right) \right) . \tag{3.61}$$

The results for periodic chains with lengths up to $N = 200$ are shown in Fig. 3.9. It can be seen that the behavior for increasing N (decreasing $1/N^2$) is excellently reproduced by Eq. (3.61).

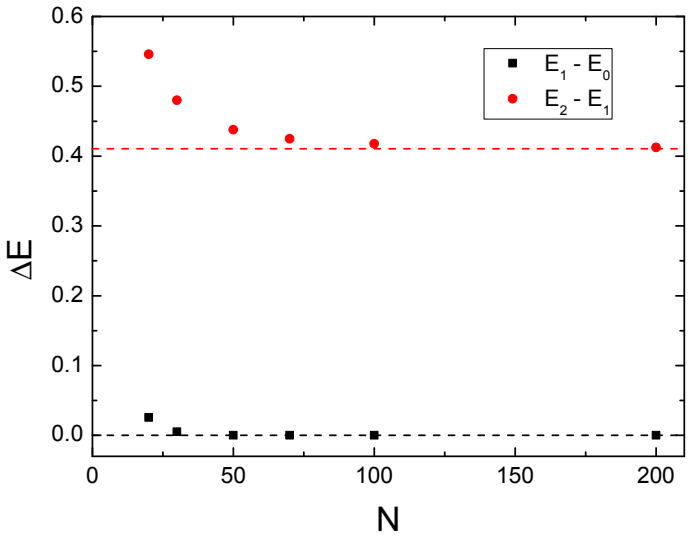

Figure 3.8.: The energy gaps $E_1 - E_0$ and $E_2 - E_1$ as obtained by DMRG calculations for open $s = 1$ chains of different lengths N. E_0 denotes the ground state energy, and E_1 and E_2 are the energies of the first and second excited state. The dashed lines show the expected results for the thermodynamic limit. Up to $m = 200$ density matrix eigenstates have been kept for these calculations resulting in a truncated weight smaller than 10^{-10}.

3.8.3. Convergence and reduced density matrix spectra

In this paragraph, the convergence properties of the DMRG algorithm as implemented for this work are tested in a similar way to Ref. [86]. As pointed out in Ref. [86], DMRG results become more inaccurate the more states are targeted. Also, periodic boundary conditions decrease the accuracy compared with open boundary conditions [86]. On the other hand, keeping more density matrix eigenstates should result in more accurate results since the variational space becomes larger. As an example we consider a chain with $N = 16$ spins of $s = 1$. For this chain size, the Lanczos algorithm still allows for a numerically exact calculation of low-lying energy eigenvalues and eigenstates [153]. We have used the *ALPS sparsediag* code [154,155] to calculate the ground state energy for the $N = 16$ chain with open and periodic boundary conditions. The exact values are $E_0^{\text{open}} = -21.250217994164$ and $E_0^{\text{periodic}} = -22.446807281173$.

In Fig. 3.10 the absolute error of the ground state energy as calculated using DMRG for periodic and open boundary conditions is shown as function of m. It can be seen that for fixed m the error is several orders of magnitude larger for periodic boundary conditions compared to the case of open boundary conditions. This can

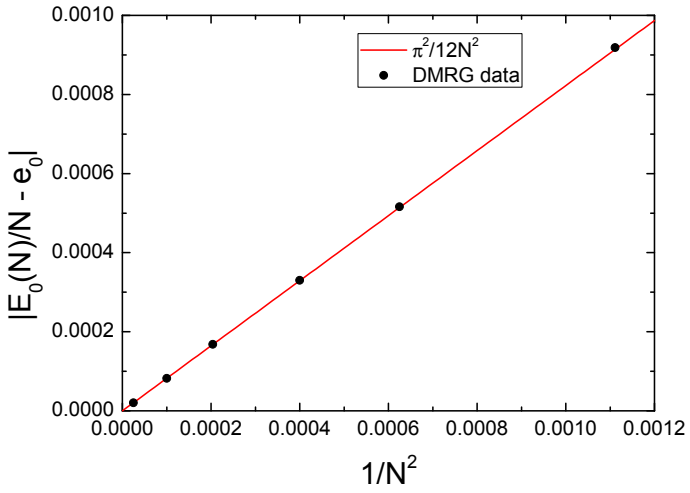

Figure 3.9.: Difference between the ground state energy per spin of finite periodic $s = 1/2$ chains (calculated with DMRG) and the exact infinite system value plotted against $1/N^2$. The line shows the finite-size behavior as expected from Eq. (3.61). We have kept up to $m = 500$ density matrix eigenstates for the $N = 200$ ring so that the truncated weight is at most of the order of 10^{-7}.

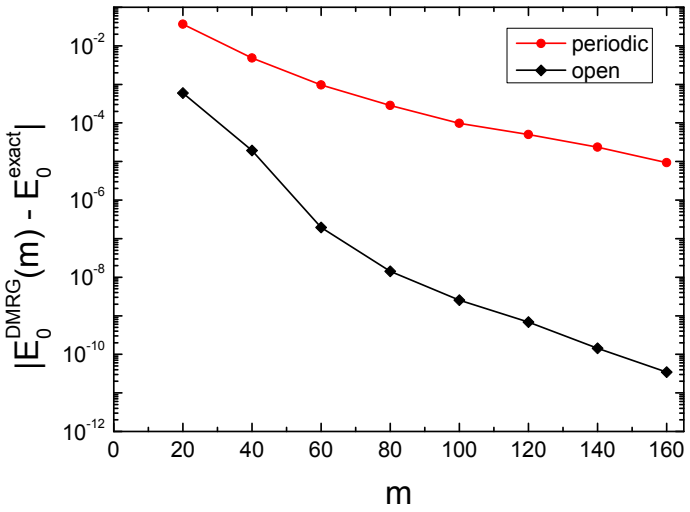

Figure 3.10.: Error of the ground state energy of an $s = 1$ and $N = 16$ Heisenberg chain with open and periodic boundary conditions as calculated with DMRG for different m values.

be understood by looking at the spectrum of the reduced density matrix for one half of the chain. The spectra for the open and periodic system are shown in Fig. 3.11. For the periodic chain the eigenvalue spectrum of the reduced density matrix decays much more slowly.

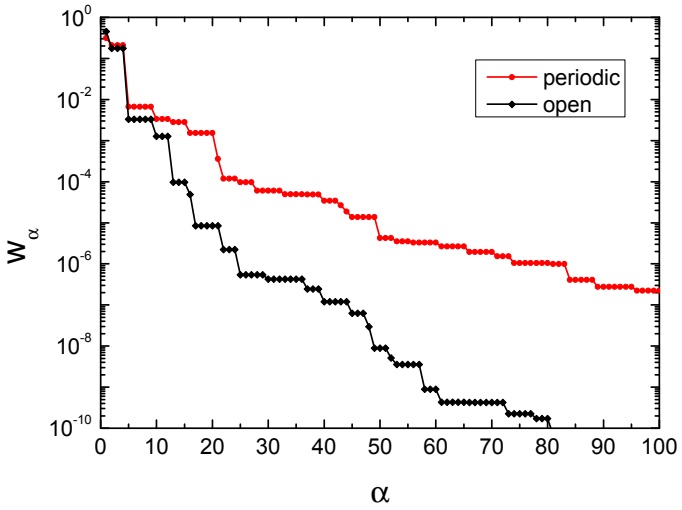

Figure 3.11.: Reduced density matrix spectrum of an $s = 1$ and $N = 16$ Heisenberg chain with open and periodic boundary conditions as calculated with DMRG for a symmetric partition of the system (i.e., both blocks have the same size). The reduced density matrix eigenvalues are ordered such that $w_\alpha \geq w_{\alpha+1}\ \forall\alpha$. We have kept $m = 140$ density matrix eigenstates in the calculation.

The accuracy of the results for a varying number of simultaneously targeted energy eigenstates is shown in Fig. 3.12 and Tab. 3.1 (for a periodic Heisenberg chain with $N = 16$ and $s = 1$). For this purpose, the lowest n energy eigenvalues (with $n = 1, 2, 4$) in the $M = 0$ subspace were calculated. The exact eigenvalues ($E_0 = -22.446807281173$, $E_1 = -22.004011719815$, and $E_2 = E_3 = -21.380099425721$) were again calculated using the ALPS sparsediag program [154, 155]. It can be seen that a larger number of simultaneously targeted eigenstates leads to a slower decay of the reduced density matrix spectra and consequently to a lower accuracy of the results for fixed m.

3.8.4. Comparison with exact diagonalization and ALPS DMRG: The icosidodecahedron

As a more complicated example we consider the $s = 1/2$ Heisenberg icosidodecahedron ($N = 30$, see Fig. 4.1 in chapter 4) which can still be treated using the Lanczos

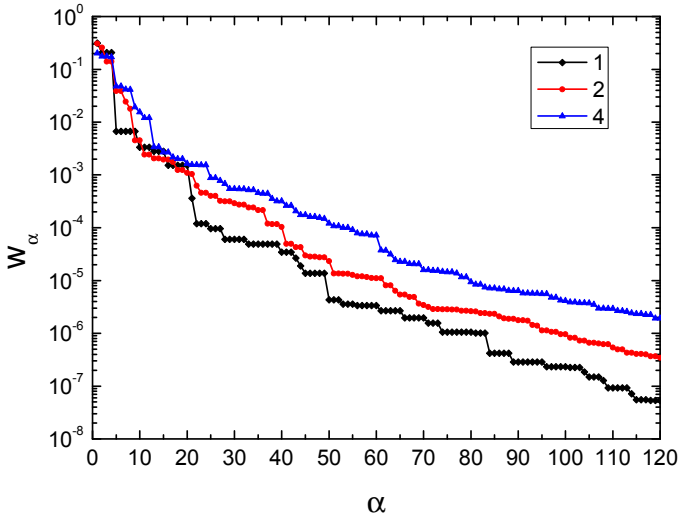

Figure 3.12.: Spectra of the reduced density matrices of an $s = 1$ Heisenberg spin ring with $N = 16$ for a varying number of simultaneously targeted energy eigenstates in the $M = 0$ subspace, calculated with $m = 300$ for a symmetric partition of the system (i.e., both blocks have the same size).

n	1	2	4
E_0^{DMRG}	-22.446807157967	-22.446806594872	-22.446804447681
error	$1.232 \cdot 10^{-7}$	$6.863 \cdot 10^{-7}$	$2.833 \cdot 10^{-6}$
E_1^{DMRG}	-	-22.004011004224	-22.004008692221
error	-	$7.156 \cdot 10^{-7}$	$3.028 \cdot 10^{-6}$
E_2^{DMRG}	-	-	-21.3800927350638
error	-	-	$6.691 \cdot 10^{-6}$
E_3^{DMRG}	-	-	-21.380094563956
error	-	-	$4.862 \cdot 10^{-6}$

Table 3.1.: The n lowest energy eigenvalues for a periodic Heisenberg chain ($s = 1$, $N = 16$) were calculated by simultaneously targeting the corresponding states in the $M = 0$ subspace with equal weights. $m = 300$ has been used for all calculations. The more states are targeted, the higher is the absolute error for fixed m. However, the agreement with the exact values (see text) is still excellent, and furthermore the degeneracy of E_2 and E_3 causes no trouble for our DMRG implementation. The truncated weights at the last step of the DMRG calculations are $8 \cdot 10^{-9}$ ($n = 1$), $5 \cdot 10^{-8}$ ($n = 2$), and $5 \cdot 10^{-7}$ ($n = 4$).

algorithm [19, 20]. We have used the mapping to a one-dimensional chain according to Ref. [121]. This system will be analyzed in more detail in chapter 4. The DMRG energies as a function of the sweep number are shown in Fig. 3.13.

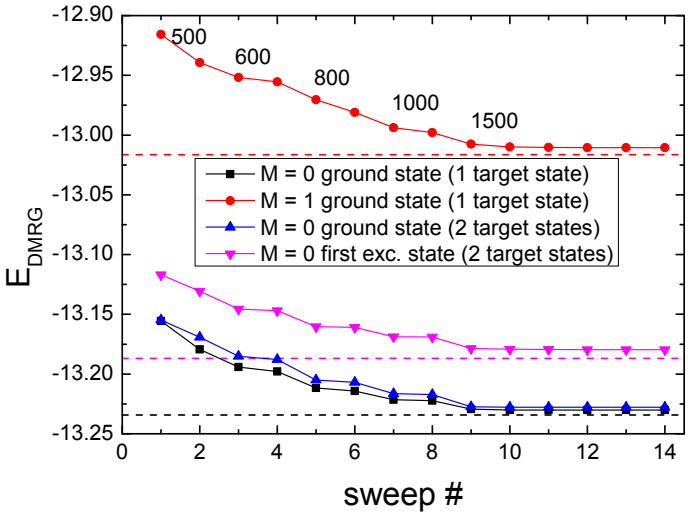

Figure 3.13.: Lowest energy eigenvalues of the antiferromagnetic Heisenberg icosidodecahedron with $s = 1/2$. The results have been obtained in three different calculations: a calculation of the lowest energy eigenvalue in the $M = 0$ and $M = 1$ subspaces (one target state for each calculation) and a simultaneous calculation of the two lowest eigenvalues in the $M = 0$ subspace. The same m sequence has been used in all three calculations. The numbers in the upper part of the figure indicate the values of m that were used for the different sweeps. For the last 6 sweeps, $m = 1500$ states were kept. The dashed lines indicate the exact results, taken from Ref. [20].

From sweep to sweep, we have increased the number of retained density matrix eigenstates. It can clearly be seen that the energies converge towards the correct results for increasing m. However, this system is already very hard to treat with DMRG and many density matrix eigenstates are needed to get sufficient convergence.

In Tab. 3.2, the DMRG energies obtained at the end of the last sweep are presented and compared with both exact diagonalization results and results of the *ALPS DMRG* program[7] [154]. The ALPS program uses a different weighting scheme for the target states when several states are simultaneously targeted. This explains the small differences in the case that the two lowest energy eigenstates in the $M = 0$ subspace are calculated.

[7] ALPS DMRG is a freely available DMRG program, see `http://alps.comp-phys.org`.

	self-written program	ALPS DMRG
$M = 0$ lowest state (1 target state)	-13.2301675711	-13.2301677929
truncated weight	$8.762 \cdot 10^{-5}$	$8.756 \cdot 10^{-5}$
$M = 1$ lowest state (1 target state)	-13.0104914709	-13.0104911717
truncated weight	$1.245 \cdot 10^{-4}$	$1.241 \cdot 10^{-4}$
$M = 0$ lowest state (2 target states)	-13.2276866784	-13.2294884014
$M = 0$ first excited state	-13.17963752313	-13.1753087703
truncated weight	$3.087 \cdot 10^{-4}$	$2.160 \cdot 10^{-4}$

Table 3.2.: Comparison of the results of our own program with the results of the ALPS DMRG code. Energy eigenvalues of the $s = 1/2$ icosidodecahedron from the last sweep of three different calculations are compared (see Fig. 3.13): the lowest eigenvalue in the $M = 0$ subspace, the lowest eigenvalue in the $M = 1$ subspace, and the two lowest eigenvalues in the $M = 0$ subspace (i.e., two states were simultaneously targeted). $m = 1500$ states were kept in the last sweep. The ALPS program uses a different weighting if several states are simultaneously targeted. This explains the differences when two states are targeted in the $M = 0$ subspace.

3.8.5. Test of the DDMRG implementation

In order to test our implementation of the DDMRG method, we investigate the zero-temperature dynamical correlation functions

$$S_j^z(\omega) = \sum_n |\langle 0|s_j^z|n\rangle|^2 \delta_\eta(\omega - E_n + E_0) \tag{3.62}$$

and

$$S^z(k,\omega) = \sum_n |\langle 0|S^z(k)|n\rangle|^2 \delta_\eta(\omega - E_n + E_0)\,, \tag{3.63}$$

where $\delta_\eta(x)$ is the Lorentzian function and

$$S^z(k) \equiv \sum_j e^{\frac{2\pi i j k}{N}} s_j^z\,. \tag{3.64}$$

$|n\rangle$ denotes an energy eigenstate with eigenvalue E_n and $|0\rangle$ is the ground state. For uniform spin rings, the transition operator $S^z(k)$ can be replaced in the dynamical correlation function (3.63) by

$$\tilde{S}^z(k) = C \cos\left(\frac{2\pi k j}{N}\right) s_j^z\,, \tag{3.65}$$

with $C = 1$ for $k = 0, N/2$ and $C = \sqrt{2}$ otherwise without changing the result [7,156]. We consider a uniform antiferromagnetic Heisenberg spin ring (i.e., periodic

boundary conditions are applied) with $N = 18$ spins with $s = 1/2$. This system can also be treated using exact diagonalization. The low-energy spectrum (with quantum numbers k and S) is shown in Fig. 3.14. The use of $S^z(k)$ as the transition operator leads to the selection rule $\Delta k = k + Nz$ (z is an integer number) for the matrix elements $\langle 0|S^z(k)|n\rangle$ [75]. Δk denotes the difference between the shift quantum number of the ground state and that of the excited state. For both transition operators we have the selection rule $\Delta S = 1$ since the system has an $S = 0$ ground state. This means that only transitions to $S = 1$ states can be observed at $T = 0$. Furthermore, $S^z(k, \omega)$ allows for an investigation of the k quantum numbers of the excited states.

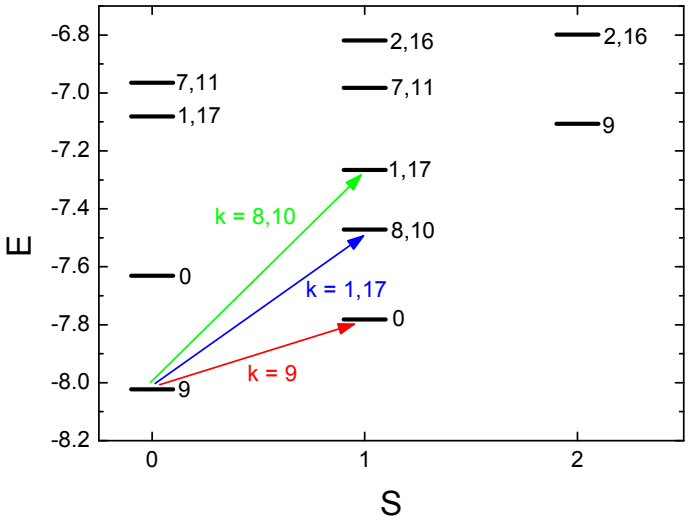

Figure 3.14.: Low-energy spectrum of a Heisenberg spin ring ($N = 18$, $s = 1/2$) as obtained by exact diagonalization. (These calculations were performed by J. Schnack [157].) The numbers next to the energy levels denote the corresponding shift quantum numbers and the arrows show the three lowest transitions that we can expect to observe in the dynamical correlation functions $S^z_j(\omega)$ and $S^z(k, \omega)$. The labels next to the arrows indicate for which value of k the corresponding excitation can be observed in $S^z(k, \omega)$.

The dynamical correlation functions were calculated in two different ways (cf. Sec. 3.7):

- One possibility is to target several eigenstates in the $M = 0$ subspace and directly calculate the transition matrix elements [136, 158]. This variant is called *standard DMRG* in the following.
- Another possibility is an effective calculation via the correction vector. This

variant is denoted as *DDMRG*.

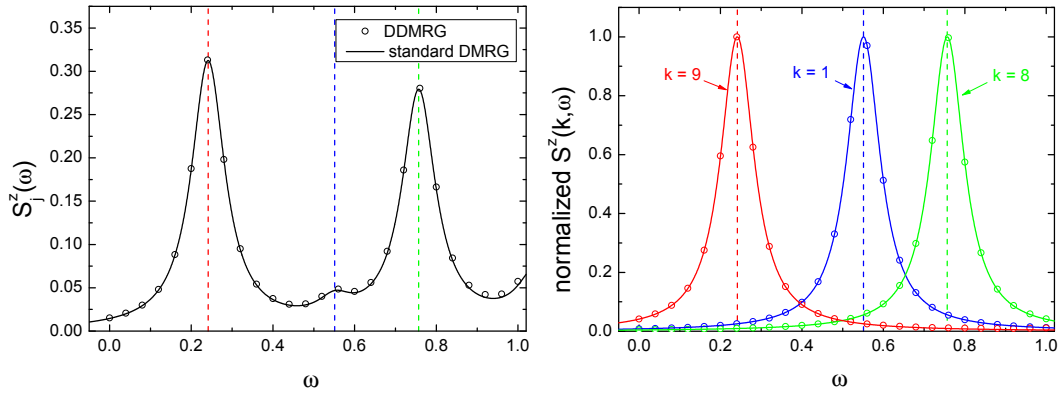

Figure 3.15.: Dynamical correlation functions $S^z_j(\omega)$ (left) and $S^z(k,\omega)$ (right), calculated both with the standard DMRG code (solid lines) and the DDMRG code (symbols). For the standard DMRG calculations 20 eigenvectors in the $M = 0$ sector were simultaneously targeted with $m = 250$ retained density matrix eigenstates. The transition matrix elements were then calculated and used for the calculation of $S^z_j(\omega)$ and $S^z(k,\omega)$. In the DDMRG calculations, $m = 128$ states were kept. The $S^z(k,\omega)$ data is normalized so that the maximal value is 1 for each curve and the broadening is chosen as $\eta = 0.05$. The dashed lines show the exact energy differences between the lowest three excited states and the ground state, cf. Fig. 3.14.

The results of both approaches are compared in Fig. 3.15. For the DDMRG calculation we have chosen $j = 15$, i.e., the center of the chain, but the dynamical correlation function should be independent of j for this system. An excellent agreement is observed and the peaks of the dynamical correlation functions furthermore lie at the correct positions, which can be deduced from the exact spectrum in Fig. 3.14 and the selection rules. In particular for higher energies, it can be seen in Fig. 3.15 that the symbols, i.e., the DDMRG results, always lie above the continuous curve (the standard DMRG results). This is because of the limited number of energy eigenstates that were calculated with the standard DMRG code. For a finite broadening η, high-energy states also contribute to the spectrum at lower energies so that the dynamical correlation functions calculated with standard DMRG always lie below the true function, unless all contributing states are taken into account.

4. The antiferromagnetic Heisenberg icosidodecahedron

4.1. Introduction

In this chapter, we present DMRG results for the antiferromagnetic Heisenberg icosidodecahedron. Fig. 4.1 shows the structure of the icosidodecahedron. It is a polyhedron with 12 pentagons and 20 triangles [159], which means that it is geometrically frustrated. There exist several icosidodecahedral magnetic molecules: $Mo_{72}Fe_{30}$ [4], $W_{72}Fe_{30}$ [15] (both $s = 5/2$), $Mo_{72}Cr_{30}$ [23] ($s = 3/2$), $Mo_{72}V_{30}$ [59, 160], and $W_{72}V_{30}$ [24] (both $s = 1/2$). These molecules are some of the largest magnetic molecules synthesized to date [3] and there are a lot of experimental and theoretical studies on these systems [4, 11–14, 16–20, 22, 64, 161–166]. Icosidodecahedral magnetic molecules are of special interest because they are highly symmetric, frustrated, exist with different spin quantum numbers, and are a kind of finite-size version of the Kagomé lattice [20].

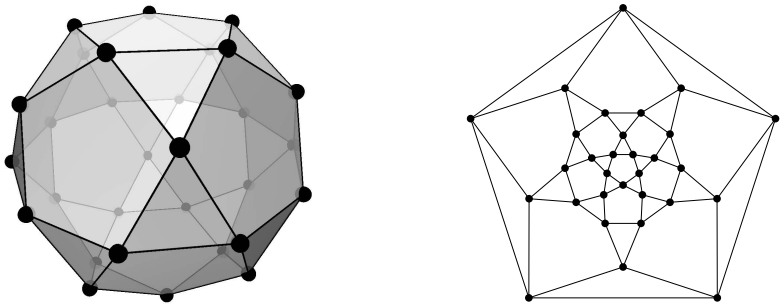

Figure 4.1.: Structure of the icosidodecahedron: The black bullets correspond to the spin positions and the lines to interaction paths between them. The right part of the figure shows a two-dimensional projection.

Experimental investigations of the magnetic properties of these molecules focus in most cases on measurements of the susceptibility as a function of temperature [4,15,23,24,59,160] or applied magnetic field [14,166], or magnetization as a function

of magnetic field [4, 16, 166]. These experiments show that the icosidodecahedral magnetic molecules have antiferromagnetic interactions and a nonmagnetic ground state. Other experimental techniques that were applied to these molecules are NMR and μSR [162, 163, 165], INS [17], diffuse (elastic) neutron scattering, and specific heat measurements [18].

These molecules are usually modeled using a simple uniform Heisenberg model [4, 12, 13, 15, 17, 18, 21–24, 59, 161, 164, 167]. However, more complicated models were also studied: Additional anisotropic terms were considered in Refs. [164] and [11], and bond disorder and distortions (i.e., more than just one exchange constant in the Heisenberg Hamiltonian) were investigated in Refs. [14] and [21]. Since the icosidodecahedral molecules comprise $N = 30$ spins, a numerically exact calculation of $T = 0$ properties is only possible for the $s = 1/2$ case [19, 20, 168]. Zero-temperature magnetization curves for the similar, but smaller cuboctahedron were already calculated in Refs. [19] and [20] for different spin quantum numbers. In Ref. [19], parts of magnetization curves were also calculated for the icosidodecahedron with $s > 1/2$, but only the smallest subspaces for large M can be treated due to the limitations of the Lanczos method. For $s = 1/2$, thermodynamic properties can also be calculated quasi-exactly for $T > 0$ using the finite-temperature Lanczos method [21, 22, 167]. Quantum Monte Carlo suffers from the negative-sign problem so that calculations for small temperatures are not feasible [23, 24, 59]. For the calculation of ground state and low-temperature properties for $s > 1/2$, approximative methods are therefore needed. For $s = 3/2$ and $s = 5/2$ systems, the classical Heisenberg model was used as an approximation [4, 13–15, 161, 164, 169], for which efficient Monte Carlo algorithms are available. However, it is not clear how good this classical approximation is for very low temperatures. This is also true for the rotational band approximation which was used in Refs. [4, 12, 16–18, 64]. Furthermore, there are features of frustrated systems such as magnetization jumps and plateaus, or low-lying singlets in the spectrum [19], for which it is known that they are not captured by the rotational band approximation. Another approximation which was applied to the icosidodecahedron and whose accuracy is unclear is spin-wave theory [11, 12].

Although there exist many theoretical studies on the icosidodecahedron with $s > 1/2$, it has to be emphasized here that accurate numerical calculations for the *full* Heisenberg model and without (semi-)classical approximations are very rare. The DMRG method allows to treat the full Heisenberg Hamiltonian in a reduced Hilbert space. As discussed in chapter 3, it relies on a controlled truncation of the Hilbert space and allows for an estimation of the accuracy. In Ref. [121], the DMRG method has already been applied to the Heisenberg icosidodecahedron with $s = 5/2$. However, a maximum of only $m = 120$ density matrix eigenstates was used so that the accuracy of the results is rather limited for such a complicated system with a geometry that is not favorable for the DMRG method.

We also apply the DMRG method to the antiferromagnetic Heisenberg icosido-

decahedron and focus on the approximate calculation of the lowest energies in the subspaces of magnetic quantum number M. These eigenvalues allow for a calculation of the $T = 0$ magnetization curve and also of energy gaps which can be probed by spectroscopic methods such as INS. For the case $s = 1/2$, we also calculate the dynamical correlation function $S_j^z(\omega)$ using DDMRG. A very recent calculation of the low-energy spectrum using variational Monte Carlo applied to so-called correlator product states (CPS) was carried out by Neuscamman and Chan in Ref. [170]. This method seems to be very promising for an accurate calculation of zero-temperature properties. In Sec. 4.2.3 we compare our DMRG results with the CPS results and the previous DMRG results.

Since we calculate magnetization curves for different spin quantum numbers, the transition to the classical limit can furthermore be studied. We always use a simple antiferromagnetic Heisenberg Hamiltonian $H_{\text{Heisenberg}}$ (see Eq. (2.2)) with $J_{ij} = J$ if the spins at positions i and j are nearest neighbors and $J_{ij} = 0$ otherwise (cf. Fig. 4.1). Before we discuss the DMRG results, we summarize basic properties of frustrated systems such as the icosidodecahedron, as well as results of the classical and rotational band approximations.

4.1.1. Properties of systems with corner-sharing triangles

The icosidodecahedron consists of 12 corner-sharing triangles. Antiferromagnetic frustrated spin systems with corner-sharing triangles, e.g., the Kagomé lattice or the cuboctahedron, have special properties such as [19, 20, 26, 168, 171]:

- low-lying singlets below the first triplet, i.e., there exist several excited $S = 0$ states with lower energies than the energetically lowest $S = 1$ state;
- magnetization plateaus in the $T = 0$ magnetization curve at one-third of the saturation magnetization;
- magnetization jumps to saturation.

The magnetization jumps can be attributed to localized independent magnon states, which are exact eigenstates of the Heisenberg Hamiltonian [168, 171]. Starting from the ferromagnetic state, it is possible to place some localized excitations with $|\Delta M| = 1$ on the Kagomé lattice, the cuboctahedron, or the icosidodecahedron. Since these excitations are localized and do not interact, the total energy depends linearly on their number and thus on the magnetization. This linear dependence results in a jump to saturation of the (zero-temperature) magnetization. However, the number of localized independent magnon states that can be placed on a finite lattice is limited, of course. In the case of the icosidodecahedron, three localized excitations can be placed on the lattice without interaction, so that the magnetization jump to saturation has a height of $\Delta\mathcal{M}/(g\mu_B) = 3$ [168].

4.1.2. Classical limit and the rotational band approximation

The classical ground state (in the limit $s \to \infty$) as a function of the magnetic field $\vec{B}$ was calculated in Ref. [161]. The icosidodecahedron is three-colorable, which means that it is possible to divide it into three sublattices A, B, and C such that spins on the same sublattice do not interact with each other and only interactions between spins on different sublattices occur. The classical ground state for zero magnetic field has a simple structure: Spins on the same sublattice point in the same direction and the angle between spins on different sublattices is 120°. For a finite magnetic field B, the ground state energy has a parabolic dependence on B, which leads to a (zero-temperature) magnetization curve that is linear in B up to the saturation magnetization [161]. The zero-temperature susceptibility for fields smaller than the saturation field is thus simply a constant. For finite temperature an interesting effect occurs: The susceptibility shows a dip near one-third of the saturation field [13]. This effect is attributed to magnetically stiff "up-up-down" configurations that contribute to the partition function. At the field where the dip occurs, the ground state as described above (i.e., the 120° configuration) has the same energy as the configuration where the spins on each triangle have a "up-up-down" structure. This dip in the susceptibility has also been measured in several experiments but the explanation on the basis of a classical system is rather unsatisfactory since the temperature in the experiments was very low [13, 14].

The rotational band approximation [16, 64] leads to very similar results for the zero-temperature magnetization. It is expected to be a good approximation only for large s quantum numbers. The idea of the rotational band approximation is to use states of the form $|S_A S_B S_C S M\rangle$ as approximations of the energetically lowest states in the S subspaces (cf. Sec. 2.2.3). Here, S_X denotes the spin quantum number of sublattice X with $X = A, B, C$. In the subspace of states with $S_A = S_B = S_C = Ns/3$ ($N = 30$ is the number of spins) the full Heisenberg Hamiltonian is equivalent to the three-spin Hamiltonian [12]

$$\begin{aligned} H_{ABC} &= \frac{J}{5}\left(\vec{S}_A \cdot \vec{S}_B + \vec{S}_B \cdot \vec{S}_C + \vec{S}_C \cdot \vec{S}_A\right) \\ &= \frac{J}{10}\left(\vec{S}^2 - \vec{S}_A^2 - \vec{S}_B^2 - \vec{S}_C^2\right) . \end{aligned} \tag{4.1}$$

The energy eigenvalues of H_{ABC} are then given by

$$E_{ABC}(S, S_A, S_B, S_C) = \frac{J}{10}(S(S+1) - S_A(S_A+1) - S_B(S_B+1) - S_C(S_C+1)) . \tag{4.2}$$

For $S_A = S_B = S_C = Ns/3$, the eigenvalues of the lowest rotational band are obtained. For $S_A = Ns/3 - 1$, $S_B = S_C = Ns/3$ and permutations thereof, we get the energy eigenvalues of the next-higher rotational band [17]. The zero-temperature

magnetization curve in the rotational band approximation is a staircase with constant step width up to the saturation magnetization. The dynamical correlation function $S_j^z(\omega)$, which is related to INS spectra, shows only two peaks at $T = 0$ in this approximation [17]. One peak corresponds to a transition within the lowest rotational band ($\Delta E_1 = J/5$) and the other peak corresponds to transitions to the next-higher rotational band ($\Delta E_2 = \frac{J}{5} + 2Js$). It is expected that the level structure that is predicted by the rotational band model is too simple to accurately describe the excitations of the full 30-spin Hamiltonian and is only a good approximation for the lowest energies in the S subspaces [12, 17]. For example, the rotational band approximation cannot fully explain results of INS experiments that were obtained for the $s = 5/2$ system $Mo_{72}Fe_{30}$ [17].

In Refs. [16, 121] a modified rotational band approximation with "quantum corrections" has been proposed in order to better reproduce measured magnetization curves. In the modified version, an additional parameter γ and the overall prefactor a are introduced as parameters:

$$\begin{aligned} E^{\mathrm{mod}}_{ABC}(S, S_A, S_B, S_C) &= aJ\Big\{S(S+1) - \gamma(S_A(S_A+1) \\ &\quad + S_B(S_B+1) + S_C(S_C+1))\Big\}. \end{aligned} \tag{4.3}$$

Based on a comparison to magnetization measurements for $Mo_{72}Fe_{30}$ ($s = 5/2$), the values $a = 0.1038$ and $\gamma = 1.07$ were obtained [16]. The DMRG calculation in Ref. [121] yielded $a = 0.1028$ and $\gamma = 1.05$. Both results are actually very close to the simple rotational band model with $a = 1/10$ and $\gamma = 1$. We will compare our new DMRG results with these numbers at the end of this chapter.

4.2. DMRG results

The DMRG technique is best suited for open one-dimensional chains, but can be applied to systems with an arbitrary geometry. The icosidodecahedron can be viewed as a two-dimensional lattice on a sphere (similar to the Kagomé lattice, see [20]), i.e., a lattice with periodic boundary conditions. This means that no numerically exact results can be expected when DMRG is applied to such a system. However, the accuracy of calculated quantities can be estimated by varying the number of kept density matrix eigenstates and watching the changes in the quantity of interest. Since DMRG is a variational method, it is clear that the lower the energy, the better is the approximation of the ground state (or the energetically lowest state in a subspace). Furthermore, the truncated weight Δw offers the possibility to judge the quality of the results, and an extrapolation to zero truncated weight (or $m \to \infty$) is possible if enough data are available.

4.2.1. Numbering of the spins

When DMRG is applied to spin systems that are not one-dimensional, the usual way is to map the system on a one-dimensional chain with long-range interactions. This is done by numbering the spins in a certain way [126]. However, for complex system it is not clear, which numbering produces the best results [172]. A similar problem occurs when DMRG is applied in the field of quantum chemistry, where models similar to the Hubbard model with long-range interactions are used and the orbitals have to be ordered in some way [114,172–175]. Since long-range interactions diminish the accuracy of the DMRG method (cf. Ref. [127]), it is clear that a good ordering needs to minimize long-range interactions as much as possible. In Ref. [114], the reverse Cuthill-McKee algorithm [176, 177] was proposed to obtain a "good" ordering. In Ref. [172], a genetic algorithm was used to get good orderings for a specific system. However, employing a genetic algorithm is very costly since calculations for many different orderings have to be performed.

We have tested several orderings for the icosidodecahedron. The coupling matrices J_{ij} resulting from the different numberings of the vertices of the icosidodecahedron are shown in Fig. 4.2. This system has already been treated with DMRG by Exler and Schnack in Ref. [121]. The numbering used by Exler and Schnack (see top left of Fig. 4.2) gives a very regular "interaction pattern" with rather short-ranged interactions. However, the periodic boundaries, i.e., the interactions between the first and the last spins, are clearly not optimal for the DMRG algorithm with two center sites. As proposed in Ref. [114], we have also tested a variant of the reverse Cuthill-McKee algorithm [176, 177], the RCMD algorithm, which aims to number the vertices such that the bandwidth of the matrix is minimized. In addition, we have applied the Sloan algorithm [178], which minimizes the "envelope size", i.e., the sum of the "row bandwidths". (The bandwidth is the maximum of the row bandwidths.) These algorithms were used as implemented in Mathematica [179]. Fig. 4.2 also shows an unoptimized numbering for comparison.

Results of DMRG calculations (using the ALPS DMRG code [154]) for the different spin numberings are presented in Fig. 4.3. We have calculated the ground state energy of the $s = 1/2$ icosidodecahedron with an increasing number of retained density matrix eigenstates m so that the convergence can be investigated by comparing with the exact ground state energy (see Ref. [20]). One can see that the different optimized numberings (Exler/Schnack, RCMD, and Sloan) give almost identical results whereas the convergence properties of the unoptimized numbering are much worse. These results show that it is essential to use an optimized numbering of the spins when the DMRG method is applied to a spin system with a complicated structure. For the remaining results in this chapter, we have always used the numbering proposed by Exler and Schnack.

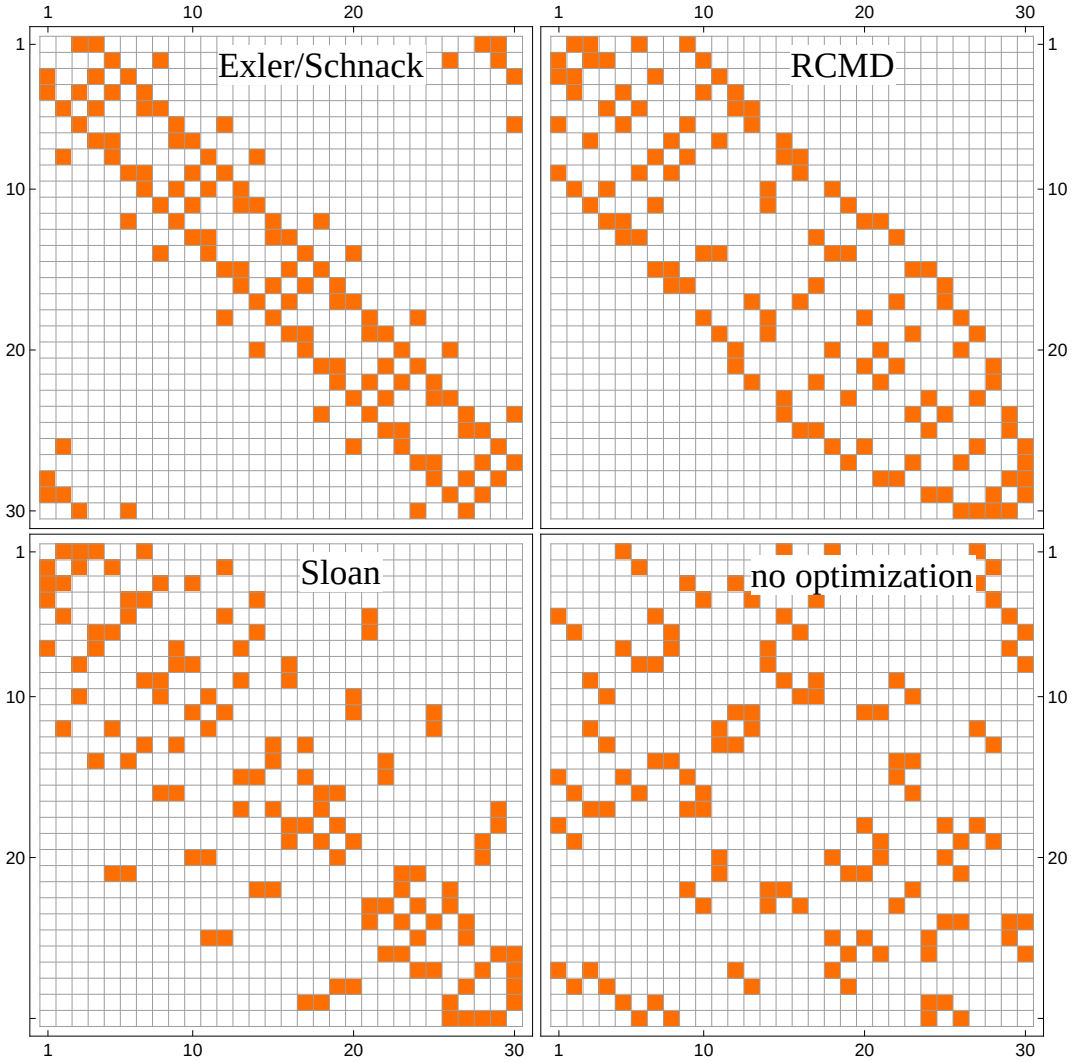

Figure 4.2.: Depiction of the coupling matrix J_{ij} for four different numberings of the vertices of the icosidodecahedron. Nonzero entries are indicated by orange squares. Top left: numbering according to Exler and Schnack (see Ref. [121]); top right: result of the RCMD algorithm; bottom left: result of the Sloan algorithm; bottom right: unoptimized numbering.

4.2.2. Lowest energy eigenvalues and magnetization curves

As the next step, we have calculated the lowest energies in the M subspaces for the icosidodecahedron with $s > 1/2$ using DMRG. The results for the $s = 1/2$ system

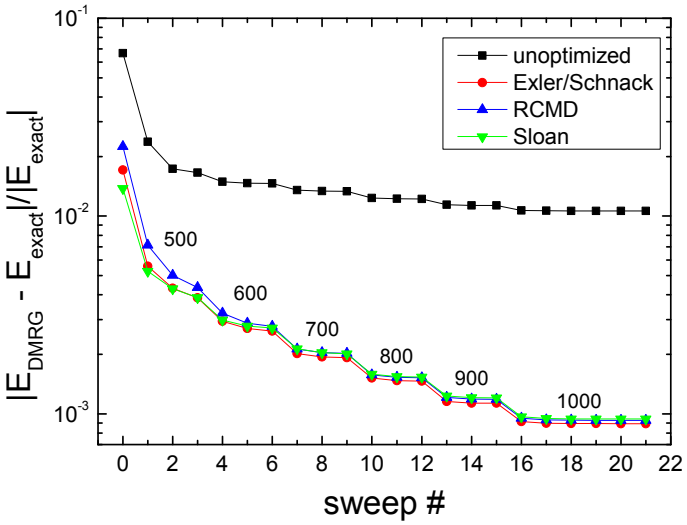

Figure 4.3.: Comparison of DMRG results for different numberings (see Fig. 4.2) of the $s = 1/2$ spins at the vertices of the icosidodecahedron. The plot shows the error of the ground state energy as obtained by DMRG and as a function of the sweep number. The exact energy is taken from Ref. [20]. The numbers above the symbols denote the number of density matrix eigenstates that were kept for the sweep. We have used the ALPS DMRG code [154] for these calculations.

already demonstrated that DMRG is still able to produce accurate results for this system with a relative error smaller than 10^{-3}. However, the accuracy is much worse than in the ideal case of one-dimensional chains with open boundaries (cf. Fig. 3.10 in chapter 3).

Fig. 4.4 shows the lowest energy eigenvalues in the subspaces of total magnetic quantum number M for the icosidodecahedron with $s = 1$ and $s = 3/2$ as obtained by DMRG. Note that for subspaces with large M ($M > 18$ for $s = 1$ and $M > 33$ for $s = 3/2$) results from Lanczos calculations performed by J. Schnack [180] are used. We have kept up to $m = 2500$ density matrix eigenstates for the $s = 1$ case and up to $m = 2000$ for the $s = 3/2$ case. An error estimate for the results of the $s = 1$ system is given in subsection 4.2.3. The largest truncated weight is of the order of $7 \cdot 10^{-4}$ for the $M = 0$ subspace (which is the largest subspace) of the $s = 1$ icosidodecahedron and of the order of $4 \cdot 10^{-4}$ for the $s = 3/2$ case. Although more states have been kept, the truncated weight for the $s = 1$ icosidodecahedron is larger than for the $s = 3/2$ system. This indicates that, at least in this case, it cannot be a reliable quantitative measure for the error, possibly because the results are not yet fully converged for the values of m that we have used. However, these calculations are very time-consuming. For example, the calculation of the ground

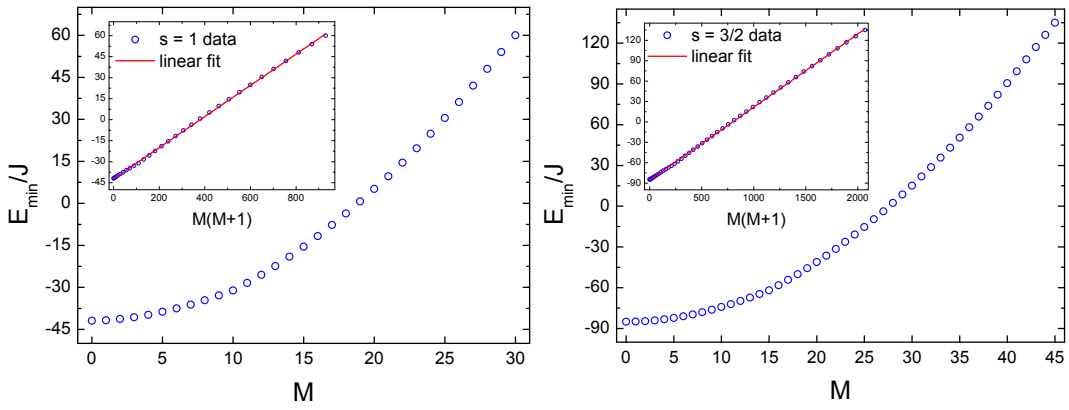

Figure 4.4.: Lowest energy eigenvalues in the subspaces of total magnetic quantum number M as obtained by DMRG calculations for the $s = 1$ (left) and the $s = 3/2$ (right) icosidodecahedron. The insets show the energies as a function of $M(M+1)$. The eigenvalues for the smallest subspaces, i.e., for large M, were calculated by J. Schnack with the Lanczos algorithm (see text). For the DMRG calculations, the ALPS DMRG code was used [154]. For the $s = 1$ system, $m = 2500$ density matrix eigenstates were kept in all DMRG calculations. For the $s = 3/2$ system, we have kept $m = 2000$ states for the subspaces with $M \leq 4$, $m = 1500$ states for the subspaces with $5 \leq M \leq 23$, and 1000 states for the subspaces with $M > 23$.

state energy ($M = 0$) of the $s = 1$ icosidodecahedron with 60 sweeps and $m = 2500$ states took about 4 weeks so that obtaining fully converged results for a fixed value of m is nearly impossible for the icosidodecahedron with $s > 1$.

The rotational band model predicts a behavior of the form $E_{\min}(M) - E_0 = aM(M+1)$, i.e., a parabolic dependence on M. The insets of Fig. 4.4 show that this is a good approximation for the lowest energy eigenvalues of the full Heisenberg model. The simple rotational band approximation predicts a proportionality constant of $a = 0.1$ (cf. Eq. (4.1)). The linear fits as shown in the insets give the values $a = 0.111$ for $s = 1$ and $a = 0.108$ for $s = 3/2$, which are quite close to the simple rotational band approximation. However, if one uses the DMRG data to calculate the zero-temperature magnetization curves, it becomes clear that there are some crucial deviations from the ideal parabolic dependence. If there was an ideal parabolic dependence, the resulting magnetization curve would consist of steps of constant width. Fig. 4.5 shows the resulting zero-temperature magnetization curves calculated from the DMRG data. Again, the exact diagonalization data for $s = 1/2$ is taken from Ref. [20]. One can see that the magnetization curves do not consist of steps with constant width. There are some anomalies as expected for frustrated systems. In particular, plateaus at $\mathcal{M}/\mathcal{M}_{\text{sat}} = 1/3$ are clearly visible. The

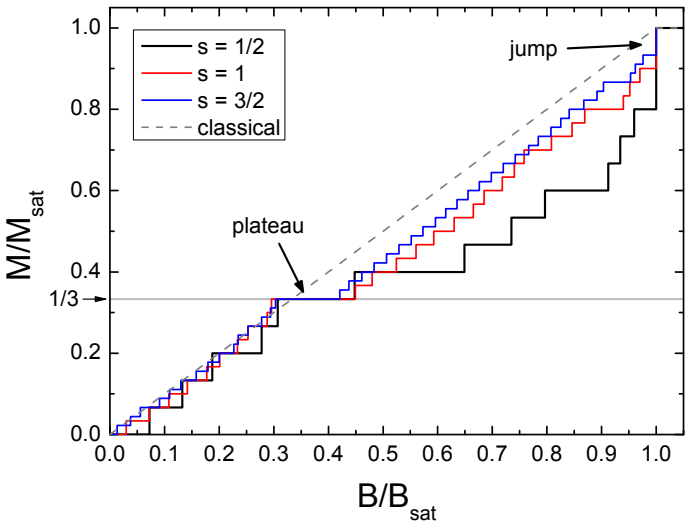

Figure 4.5.: Zero-temperature magnetization curves of the icosidodecahedron with $s = 1/2$, 1, and 3/2. The data for $s = 1/2$ is taken from Ref. [20], whereas the data for $s = 1$ add $s = 3/2$ are obtained by DMRG calculations (cf. Fig. 4.4). The dashed line shows the classical result [161]. The data is normalized to the saturation field and the saturation magnetization.

magnetization jumps to saturation due to the independent magnons (see Sec. 4.1.1 and Ref. [168]) are also visible. Since the jump has a fixed height of $\Delta M = 3$, it is clear that this effect vanishes in the plot for $s \to \infty$ because the magnetization is normalized to the saturation magnetization $\mathcal{M}_{\text{sat}} = 30 g \mu_B s$. For $s \to \infty$, the classical result, i.e., a strictly linear magnetization curve, is expected to be reached. However, the plateau seems to be very stable even for large s (see below). A similar behavior was already observed for the cuboctahedron, see Ref. [20].

For the cases $s = 2$ and $s = 5/2$ we have calculated the lowest energy eigenvalues only in some M subspaces, including those subspaces that are relevant for the calculation of the plateau width. We have kept $m = 2000$ density matrix eigenstates in these calculations. The magnetization curves are shown in Fig. 4.6. The plateau is clearly visible, even for $s = 5/2$. However, it is not clear if these plateaus can be measured in experiments. It was shown in Ref. [22] for the $s = 1/2$ system that the plateau disappears rather quickly with increasing temperature. Fig. 4.7 shows the plateau width for different values of s as obtained by the DMRG calculations and the exact diagonalization for $s = 1/2$ [20]. The figure also contains an extrapolation to $s \to \infty$ using the data for $s > 1/2$ and the ansatz $a + b/(x - c)$, where x denotes the plateau width and a, b, and c are constants. The extrapolated value for the plateau width of $0.013 B_{\text{sat}}$ is not exactly zero, but rather close to the expected value. It

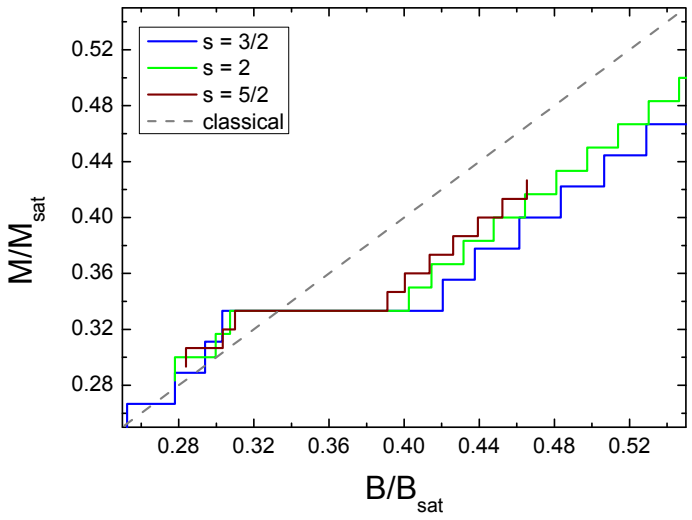

Figure 4.6.: Zero-temperature magnetization curves of the icosidodecahedron for $s = 3/2, 2, 5/2$ as obtained by (ALPS) DMRG calculations. We have kept $m = 2000$ density matrix eigenstates in these calculations. The dashed line shows the classical result [161]. As before, the data is normalized to the saturation field and the saturation magnetization.

has to be emphasized here that the plateau widths calculated using DMRG (i.e., for $s > 1/2$) are not numerically exact. The accuracy of the results is analyzed in the next subsection.

4.2.3. Estimation of the accuracy and comparison with CPS and previous DMRG results

A reasonable extrapolation in m (the number of kept density matrix eigenstates) or Δw (truncated weight) is only possible if the results are fully converged for each m value. Fig. 4.8 shows the ground state energy and the lowest energy in the $M = 1$ subspace of the $s = 1$ icosidodecahedron as calculated using DMRG for different values of m. We have carried out 12 sweeps for each value of m.

An extrapolation to $m \to \infty$ with an exponential ansatz $a + b\exp(-cm)$ (a, b, and c are constants) yields $E_{\mathrm{min}}^{\mathrm{extra}}(M = 0) = -41.97(2)J$ and $E_{\mathrm{min}}^{\mathrm{extra}}(M = 1) = -41.76(1)J$.[1] In Ref. [121], an extrapolation using an ansatz of the form $a + b/m$, where a and b are constants, was proposed. However, this ansatz does not work very well for our data, which is calculated with much larger m values than in Ref. [121]. The right part of Fig. 4.8 shows the estimated relative error (using the extrapolated

[1] The errors given in the brackets are the standard errors of the fitting procedure.

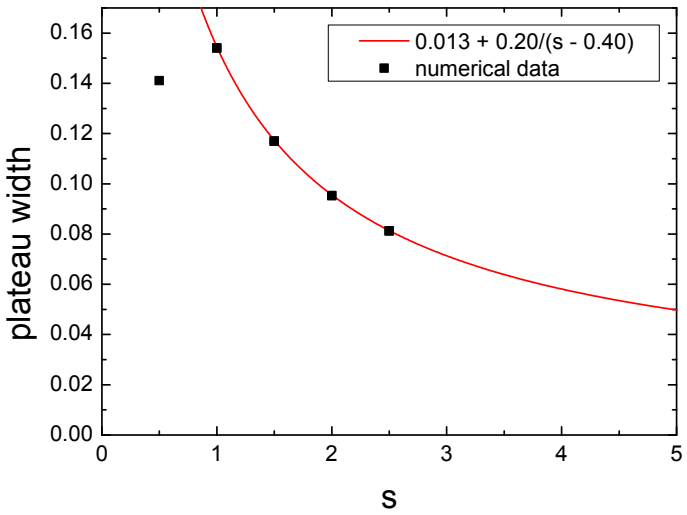

Figure 4.7.: Plateau width for different quantum numbers s as obtained by DMRG ($s > 1/2$) and exact diagonalization ($s = 1/2$) calculations. The exact diagonalization result is taken from Ref. [20]. The red line shows an extrapolation to $s \to \infty$ using the data for $s > 1/2$. The extrapolated value for the plateau width is 0.013.

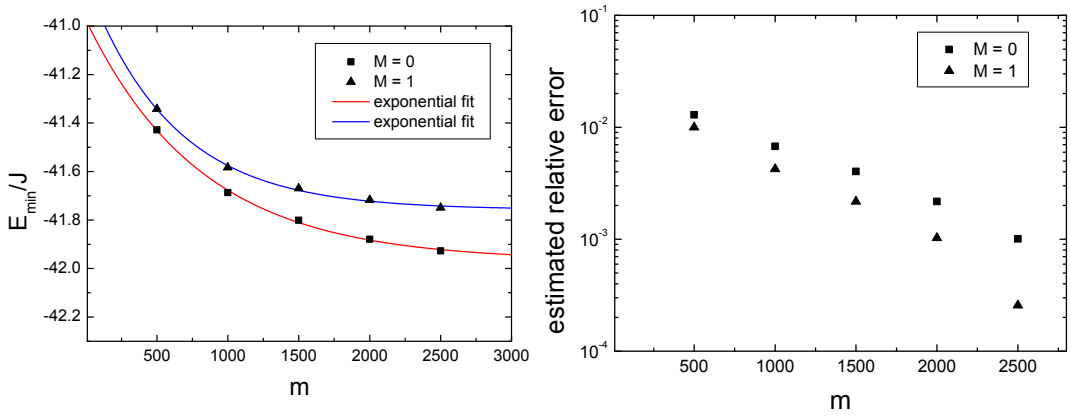

Figure 4.8.: Left: DMRG results for the lowest energy eigenvalues of the $M = 0$ and the $M = 1$ subspace of the $s = 1$ icosidodecahedron. m denotes the number of kept density matrix eigenstates. The lines are exponential fits to the data. Right: estimated relative error as a function of m.

ground state energy) as a function of m. For $m = 2500$, the relative error of the DMRG $M = 0$ energy is estimated as about 10^{-3}, which corresponds to an absolute error of approximately $0.04J$. This is a rather large value considering that the gap

to the next-higher state is about $0.2J$. For $s > 1$ such an extrapolation was not possible since it is too time-consuming and thus practically impossible to obtain converged energies for sufficiently many values of m.

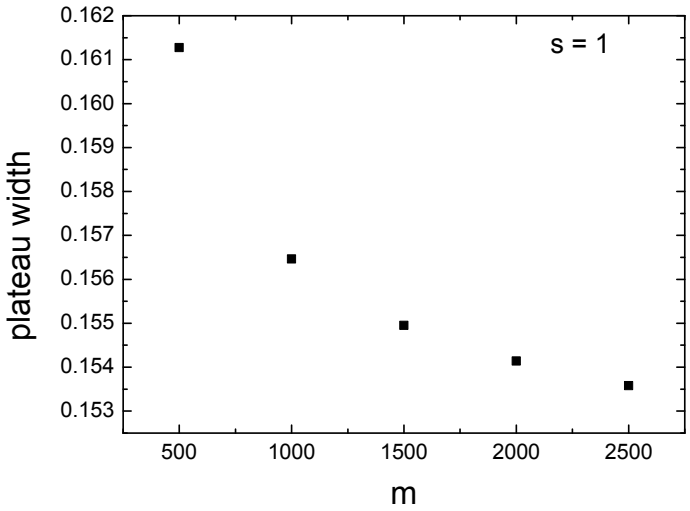

Figure 4.9.: The plateau width of the $s = 1$ icosidodecahedron as a function of the number of density matrix eigenstates that were kept in the DMRG calculations.

Fig. 4.9 shows the convergence of the width of the $\mathcal{M}_{\mathrm{sat}}/3$ plateau of the $s = 1$ icosidodecahedron as a function of m. One can see that the plateau width decreases with increasing m so that DMRG seems to overestimate the width of the plateau. We find similar effects for $s > 1$, but since the calculations are extremely time-consuming, it was not possible to produce enough data for a more systematic study of this effect. Looking more carefully at the truncated weights, we find that the DMRG calculations of the lowest energy in the $M = 10s(= \mathcal{M}_{\mathrm{sat}}/(3g\mu_B))$ subspace result in smaller values of the truncated weight than the calculations in the adjacent subspaces with the same m. However, the order of magnitude of the truncated weight is still the same. This indicates that DMRG leads to more accurate results exactly at one-third of the saturation magnetization which apparently has the consequence that the method systematically overestimates the plateau width if one works with the same m value for adjacent M subspaces.[2]

For many one-dimensional systems DMRG can be considered as a numerically exact method. This is clearly not the case for the icosidodecahedron. However, if we assume that the errors of the energy eigenvalues as obtained from the DMRG calculations are approximately the same for adjacent M subspaces, then we can still

[2]The positions of the magnetization steps are calculated using the differences $E_{\mathrm{min}}(M + 1) - E_{\mathrm{min}}(M)$, see Sec. 2.3.1.

regard the magnetization step widths as reliable. Since the subspace dimensions become smaller for increasing M, it is clear that calculations with fixed m are more accurate for the large-M subspaces. Nevertheless, we suppose that the main features of the magnetization curves as predicted by our DMRG calculations are not decisively affected by these considerations since the order of magnitude of the truncated weights is the same for energy eigenvalues in adjacent M subspaces.

The case $s = 5/2$

In this paragraph we focus on the $s = 5/2$ case and compare our calculations with previously obtained results. Fig. 4.10 shows the ground state energy as a function of the DMRG sweep number. The number of kept density matrix eigenstates increases with the sweep number. It can be seen that no convergence is achieved and

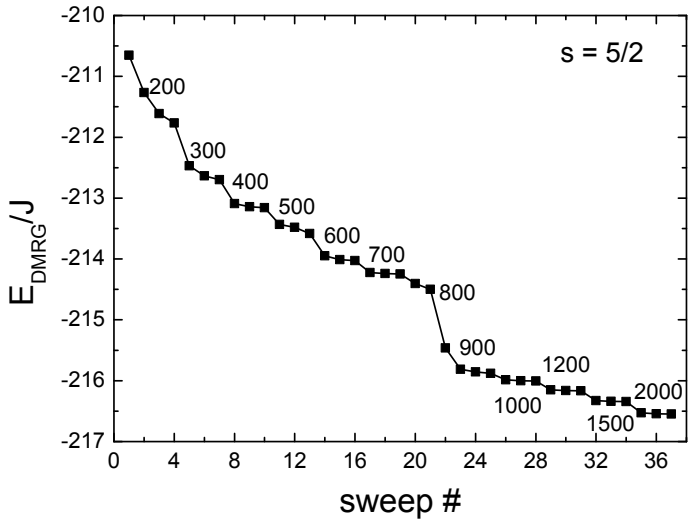

Figure 4.10.: Ground state energy of the $s = 5/2$ icosidodecahedron as a function of the DMRG sweep number. The ALPS DMRG program was used for this calculation. The numbers next to the symbols indicate the number of retained density matrix eigenstates for the different sweeps.

that probably much larger m values are needed to get converged results. Also, an extrapolation to $m \to \infty$ would not be reliably possible because it is not feasible to carry out enough sweeps for each m value.

For $m = 2000$ we obtain the value $E_0^{\mathrm{DMRG}} \approx -216.5J$, which can be compared with previous results. The DMRG result of Exler and Schnack for the ground state energy (with $m = 120$) is approximately $-211.1J$ [121], a value that is much higher and thus, since DMRG is a variational method, much more imprecise than our

result. The very recent result of Neuscamman and Chan using correlator product states (CPS) in combination with variational Monte Carlo is $-216.3J$ [170], which is also higher than our DMRG result. Furthermore, a comparison of the lowest energies in the M subspaces that are relevant for the calculation of the plateau width shows that our DMRG calculations with $m = 2000$ are more accurate than the CPS ansatz used in Ref. [170] (see Tab. 4.1). From this comparison we expect that our $s = 5/2$

M	$E_{\mathrm{min}}^{\mathrm{DMRG}}(M)/J$	$E_{\mathrm{min}}^{\mathrm{CPS}}(M)/J$
24	-158.43	-154.42
25	-153.78	-149.76
26	-147.91	-144.40

Table 4.1.: Comparison of the DMRG energies to the CPS energies for the $M = 24$, 25, and 26 subspaces of the $s = 5/2$ icosidodecahedron. For the DMRG calculations, $m = 2000$ states were kept. The CPS data is taken from Ref. [170].

DMRG data for the part of the $T = 0$ magnetization curve that includes the plateau is more accurate than the results of Ref. [170].

In Ref. [16], low-temperature magnetization data for $Mo_{72}Fe_{30}$ ($s = 5/2$) was analyzed on the basis of the modified rotational band approximation (see Sec. 4.1.2). Using these results gives a ground state energy of approximately $-216.6J$, which is very close to our DMRG result.

4.2.4. Dynamical correlation function for the $s = 1/2$ icosidodecahedron

To gain information about higher-lying excitations in the $s = 1/2$ system, we have calculated the dynamical correlation function $S_j^z(\omega)$ using DDMRG. Due to the symmetries of the system and since the ground state is nondegenerate [20], this function should be independent of j. For $s > 1/2$ such a calculation was not feasible with our program. The main problem is that DDMRG requires a rather accurate calculation of the ground state, which is one of the four target states. A large part of the spectrum of the $s = 1/2$ icosidodecahedron has already been calculated in Ref. [20], but only the energy levels and no transition matrix elements were considered. The function $S_j^z(\omega)$ also contains information about the transition matrix elements and is thus related to INS spectra.

We have kept $m = 2000$ density matrix eigenstates, which results in very time-consuming calculations. The broadening was chosen as $\eta = 0.15J$. The resulting dynamical correlation function is shown in Fig. 4.11.[3] It shows a rather sharp peak at

[3] A comparison with not yet published numerically exact Lanczos results for the same system by A. Läuchli [181] shows a nearly perfect agreement.

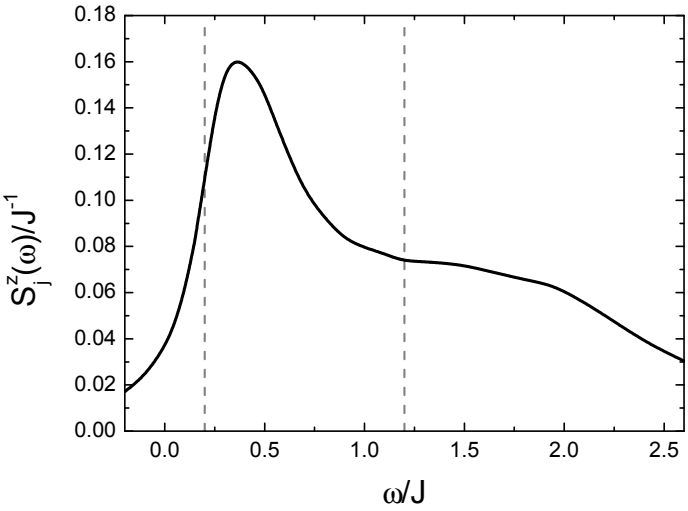

Figure 4.11.: The dynamical correlation function $S_j^z(\omega)$ of the $s = 1/2$ icosidodecahedron as obtained by DDMRG calculations. We have used $m = 2000$ and a broadening $\eta = 0.15J$. The gray dashed lines indicate the excitation energies at which the simple rotational band model predicts the peaks (see subsection 4.1.2).

approximately $0.35J$ and a very broad shoulder which falls of at approximately $2J$. The rotational band approximation predicts a two-peak structure of the dynamical correlation function (see Sec. 4.1.2 and Ref. [17]). This is clearly not the case since the spectrum of the full model is much broader and shows only one distinct peak. However, for such a large $s = 1/2$ system, we cannot expect the rotational band model to be a good approximation. It is expected to be most accurate for small systems with large spin quantum number s (see Ref. [37] and subsection 5.2.1.)

As already noted before, the $s = 1/2$ system can still be treated with the Lanczos method so that the DMRG and DDMRG techniques are not really needed for this system. DMRG, however, also allows for the calculation of magnetization curves for the icosidodecahedron with spin quantum numbers larger than $1/2$ on the basis of the full Hamiltonian. This is not possible with the Lanczos technique. It would be an important progress if the dynamical correlation functions could also be calculated for the icosidodecahedron with $s > 1/2$. This is, however, not reliably possible with our DDMRG program. The main problem is that a rather accurate ground state needs to be calculated for the DDMRG method. For the $s = 1$ icosidodecahedron, the estimated error of the ground state energy is of the order of $0.1J$ for $m = 2000$. This inaccuracy would be too large for a broadening of $\eta = 0.15J$ [182] and either a much larger broadening would have to be chosen or more states would be needed. However, keeping more states strongly increases the computational cost and a much

larger broadening would probably blur the spectrum too much. A better parallelized DDMRG code and much computing time on a supercomputer would be needed to make such calculations feasible.

5. Antiferromagnetic spin rings

5.1. Introduction

Antiferromagnetic molecules with a ring-like arrangement of the spins have attracted considerable attention since the measurement of quantum steps in the magnetization in such a system in 1994 [30]. Many of these systems consist of an even number of antiferromagnetically coupled Fe^{III} ions with $s = 5/2$. There exist realizations with $N = 6$ [63, 183], 8 [183], 10 [30], 12 [67], and 18 [9, 184] Fe^{III} centers. For these systems, there exist numerous experimental and theoretical studies [10, 38, 68, 185–191]. Many recent studies focus on the transition from quantum to classical behavior [37, 38, 191] and the possibility to observe quantum tunneling of the Néel vector [10, 68, 186, 187, 189, 190].

The numerical treatment of antiferromagnetic spin rings is hindered by the large Hilbert space dimensions. The Hilbert space dimension of a spin-5/2 system with N spins is 6^N so that complete diagonalization is currently possible only for $N \leq 10$ [51]. For $N > 10$ other numerical methods such as QMC or DMRG are needed. In this chapter we use DMRG and DDMRG to calculate static and dynamical properties of (antiferromagnetic) spin rings and focus on the molecule Fe_{18} [9] ($N = 18$, $s = 5/2$). Variants of the rotational band approximation are also often applied to antiferromagnetic spin rings [10,67,68,190] and some studies indicate that spin-wave theory (SWT) is a good approximation for some excitations of these systems (see Refs. [37, 38, 192]). We compare our DMRG results with these approximations.

This chapter is organized as follows. In the next two subsections (5.1.1 and 5.1.2), the spin models for antiferromagnetic ring molecules are introduced and spin-wave theory and the rotational band model, are briefly described. In Sec. 5.2, the results of (D)DMRG calculations for uniform Heisenberg rings with different lengths and spin quantum numbers are presented. The DMRG results are compared with the predictions of SWT and the rotational band approximation. In Sec. 5.3, the Fe_{18} molecule and results of INS measurements [25,193] are described. These INS data are compared with our DDMRG simulations. Furthermore, simulated zero-temperature (local and total) magnetization curves are presented for this molecule.

5.1.1. Spin model for antiferromagnetic spin rings

Many magnetic properties of antiferromagnetic ring molecules can be described very well by the Hamiltonian [10, 38, 39, 68]

$$H = H_{\text{Heisenberg}} + H_{\text{single-ion}} + H_{\text{Zeeman}} \,, \tag{5.1}$$

with

$$H_{\text{Heisenberg}} = \sum_{i=1}^{N} J_{i,i+1} \vec{s}_i \cdot \vec{s}_{i+1} \,, \quad N+1 \equiv 1 \,, \tag{5.2}$$

$$H_{\text{single-ion}} = D \sum_{i=1}^{N} (s_i^z)^2 \,, \tag{5.3}$$

and

$$H_{\text{Zeeman}} = g\mu_B \vec{B} \cdot \vec{S} \,. \tag{5.4}$$

For many systems, $J_{i,i+1} = J$ (giving a uniform model) and $|D/J| \ll 1$ [10,38,39,68], so that D can be neglected in some calculations. In the first part of this chapter we focus on the uniform Heisenberg Hamiltonian with only one exchange constant and also neglect the anisotropy.

5.1.2. Rotational band approximation and spin-wave theory

We briefly recall here the basic results of the rotational band approximation and spin-wave theory [194]. The rotational band approximation has already been described in a previous chapter (see section 2.2.3). It has been used with some success in the past, with high accuracy for small bipartite systems such as Fe_{12} [67]. Since spin-wave theory and effective Hamiltonians based on the rotational band approximation are much easier to handle than the full N-spin Hamiltonian, it is of fundamental interest to test the applicability and accuracy of these approximations.

The basic idea of a rotational band approximation for isotropic antiferromagnetic spin rings is to use the states $|S_A S_B S M\rangle$ as approximations of the true energy eigenstates. S_A and S_B are the sublattice spin quantum numbers. In the subspace with $S_A = S_B = Ns/2$ the full Heisenberg Hamiltonian is equivalent to the two-spin Hamiltonian

$$H_{AB}^{\text{Heisenberg}} = a_1 J \vec{S}_A \cdot \vec{S}_B \,, \tag{5.5}$$

with $a_1 = 4/N$. The energies of this Hamiltonian are then given by

$$E_{AB}(S) = \frac{2J}{N} \left(S(S+1) - \frac{Ns}{2}(Ns+2) \right) . \tag{5.6}$$

This approximation (of the low-energy spectrum) was shown to be accurate for large s values and small system sizes [37]. Better results can be obtained if one uses a "renormalized" a_1, which can be found by comparing the low-energy spectrum of the full Heisenberg Hamiltonian with the spectrum of $H_{AB}^{\text{Heisenberg}}$ [68]. It is also possible to include a uniaxial single-ion anisotropy of the form $H_{\text{single-ion}}$ (see Eq. (5.3)). This leads to an additional term

$$H_{AB}^{\text{single-ion}} = b_1 D \left((S_A^z)^2 + (S_B^z)^2 \right) , \tag{5.7}$$

where b_1 can be calculated either numerically or using first-order perturbation theory [68]. The Hamiltonian $H_{AB}^{\text{Heisenberg}} + H_{AB}^{\text{single-ion}}$ operates in a Hilbert space with the dimension $(Ns+1)^2$. For $N > 2$, the dimension is much smaller than the Hilbert space dimension associated with the full Hamiltonian, which is $(2s+1)^N$, so that the effective two-spin Hamiltonian is much easier to handle.

If one also uses the approximation with states $|S_A S_B SM\rangle$ where S_A and S_B are not coupled to their maximum values, the following analytical results can be derived for the isotropic model in this approximation (see Secs. 2.2.3, 2.3.2 and Ref. [37]). The dynamical correlation functions $S_j^z(\omega) = \sum_n |\langle 0|s_j^z|n\rangle|^2 \delta(\omega - E_n + E_0)$, which are related to the simulation of INS measurements, show only two peaks: an excitation within the lowest rotational band, i.e., from the $S = 0$ ($S_A = S_B = Ns/2$) ground state to the lowest $S = 1$ ($S_A = S_B = Ns/2$) state, and an excitation to the next-higher (energetically degenerate) $S = 1$ states ($S_A = Ns/2 - 1$, $S_B = Ns/2$ or $S_A = Ns/2$, $S_B = Ns/2 - 1$). The excitation energies are $\Delta E_1^{AB} = 4J/N$ and $\Delta E_2^{AB} = (\frac{4}{N} + 2s)J$. The corresponding transition matrix elements $W_n \equiv |\langle 0|s_j^z|n\rangle|^2$, i.e., the heights of the peaks of the dynamical correlation function, are given by

$$W_1^{AB} = \frac{1}{3} s \left(s + \frac{2}{N} \right) , \quad W_2^{AB} = \frac{1}{3} s \left(1 - \frac{2}{N} \right) . \tag{5.8}$$

Here, a summation over the matrix elements of transitions from the ground state to energetically degenerate excited states $|n\rangle_{AB}$[1] is assumed, i.e.,

$$W_2^{AB} = \sum_{n:\ E_n^{AB} = E_2^{AB}} |\, {}_{AB}\langle 0|s_j^z|n\rangle_{AB} \,|^2 . \tag{5.9}$$

It must be noted here that the large degeneracy which exists in the rotational band approximation cannot be expected for the real eigenvalues (cf. Refs. [12, 37]). This simple picture is a useful approximation only for the lowest states in the S subspaces and for $N \leq 6$. The higher-lying $S = 1$ energy levels of the full N-spin Hamiltonian, i.e., the $S = 1$ excitations above the lowest triplet, have a much richer structure and are better describable in terms of spin waves for $N > 6$ [12, 37, 192]. In the linear

[1] $|n\rangle_{AB}$ denotes a state of the rotational band approximation, i.e., a state of the form $|S_A S_B SM\rangle$.

spin-wave theory, which starts from the assumption of an ordered ground state, the excitation energies $\omega = E - E_0$ of the lowest $S = 1$ states are given by [37, 194, 195]

$$\omega_{\mathrm{LSWT}}(N, s, k) = 2sJ \left| \sin\left(\frac{2\pi k}{N}\right) \right| , \tag{5.10}$$

where $k = 0, 1, \ldots, N-1$ denotes the shift quantum number. However, this approach neglects the singlet-triplet gap which is present in the spectrum of any finite ring and disappears for half-integer s only in the thermodynamic limit. In Ref. [37] it was proposed to correct equation (5.10) using the singlet-triplet gap $\Delta_{AB} \equiv E_{AB}(S = 1) - E_{AB}(S = 0) = 4J/N$ predicted by the simple rotational band model:

$$\omega_{\mathrm{LSWT+RB}}(N, s, k) \equiv \omega_{\mathrm{LSWT}}(N, s, k) + \Delta_{AB} . \tag{5.11}$$

It is furthermore possible to include higher-order effects that are neglected in the linear spin-wave theory via the Oguchi correction factor $(1 + r/s)$ with $r = 1/2 - 1/\pi$ [196, 197]:

$$\omega_{\mathrm{RSWT+RB}}(N, s, k) \equiv \left(1 + \frac{r}{s}\right) \omega_{\mathrm{LSWT}}(N, s, k) + \Delta_{AB} . \tag{5.12}$$

Linear spin-wave theory also allows for a calculation of the dynamical correlation function $S^z(k, \omega) = \sum_n |\langle 0|S^z(k)|n\rangle|^2 \delta(\omega - E_n + E_0)$ (also called dynamical structure factor), with $S^z(k) = \sum_j \exp(2\pi i j k/N) s_j^z$ [195]:

$$S^z_{\mathrm{LSWT}}(k, \omega) = \frac{Ns}{3} \left| \tan\left(\frac{\pi k}{N}\right) \right| \delta(\omega - \omega_{\mathrm{LSWT}}(N, s, k)) . \tag{5.13}$$

In the following section we calculate energy levels and transition matrix elements of uniform antiferromagnetic Heisenberg rings using DMRG and analyze the accuracy of the rotational band approximation and the spin-wave theory results described above. We particularly focus on the case $N = 18$ and $s = 5/2$, which is relevant for Fe_{18}.

5.2. DMRG calculations for uniform antiferromagnetic Heisenberg rings

5.2.1. Accuracy of the rotational band approximation for spin rings

Using DMRG, we have calculated the energies of the ground state and the first excited state, and the corresponding transition matrix elements of antiferromagnetic Heisenberg rings for several lengths N and spin quantum numbers s. The results are summarized in Tab. 5.1.

			N			
s	6	12	18	24	30	
	-2.803	-5.387	-8.023	-10.670	-13.322	E_0/J
1/2	0.685	0.356	0.241	0.183	0.147	$\Delta E/J$
	0.491	0.276	0.194	0.150	0.123	norm. weight
	-8.617	-16.870	-25.242	-33.641	-42.046	E_0/J
1	0.721	0.484	0.432	0.417	0.413	$\Delta E/J$
	0.614	0.406	0.298	0.231	0.187	norm. weight
	-17.393	-34.131	-51.031	-67.968	-84.919	E_0/J
3/2	0.705	0.407	0.300	0.242	0.205	$\Delta E/J$
	0.691	0.520	0.430	0.371	0.328	norm. weight
	-29.165	-57.408	-85.873	-114.390	-142.927	E_0/J
2	0.697	0.391	0.284	0.229	0.195	$\Delta E/J$
	0.742	0.598	0.519	0.465	0.425	norm. weight
	-43.935	-86.679	-129.703	-172.793	-215.909	E_0/J
5/2	0.692	0.378	0.268	0.211	0.176	$\Delta E/J$
	0.779	0.654	0.585	0.538	0.503	norm. weight
	-61.704	-121.948	-182.532	-243.197	-303.893	E_0/J
3	0.688	0.370	0.259	0.202	0.167	$\Delta E/J$
	0.807	0.697	0.636	0.594	0.564	norm. weight
	-82.473	-163.217	-244.361	-325.601	-406.877	E_0/J
7/2	0.685	0.364	0.253	0.196	0.161	$\Delta E/J$
	0.828	0.730	0.676	0.638	0.611	norm. weight
	-106.241	-210.486				E_0/J
4	0.683	0.360				$\Delta E/J$
	0.846	0.757				norm. weight
	-133.010	-263.754				E_0/J
9/2	0.681	0.357				$\Delta E/J$
	0.860	0.779				norm. weight
	-162.778					E_0/J
5	0.679					$\Delta E/J$
	0.871					norm. weight

Table 5.1.: Ground state energy E_0, energy gap to the first excited state ΔE, and normalized weight of the transition from the ground state to this state, i.e., $|\langle 0|s_j^z|1\rangle|^2/\frac{1}{3}s(s+1)$ as calculated using standard DMRG. The two lowest eigenstates in the $M = 0$ subspace were targeted for these calculations. Up to 2500 density matrix eigenstates were kept so that the discarded weight is at most of the order of 10^{-7}. For the calculations on chains with $s > 5/2$ and $N > 12$ less density matrix eigenstates (around 1500) were kept (otherwise, the calculations would have taken too much computing time). For this reason, the truncated weight is of the order of 10^{-6} so that probably not all digits that are shown in the table are accurate for these parameters.

The investigations in this subsection are very similar to those in Refs. [37,191,198]. The gaps were already calculated (quasi-exactly) in Ref. [198] with QMC. Some of the gaps were also calculated in Ref. [37] using exact diagonalization. In Ref. [191], the overlap of the rotational band wave functions and the exact wave functions was calculated. However, in Refs. [37, 191] only rather small systems were investigated using exact diagonalization whereas Ref. [198] focuses on gaps only (calculated with QMC) and no transition matrix elements were calculated.

The DMRG results shown in Tab. 5.1 are compared with the predictions of the rotational band model in the following. Fig. 5.1 shows the relative difference between the rotational band prediction for the singlet-triplet gap, which is $\Delta_{AB} = 4J/N$, and the DMRG result Δ_{DMRG} for the full N-spin Heisenberg Hamiltonian.

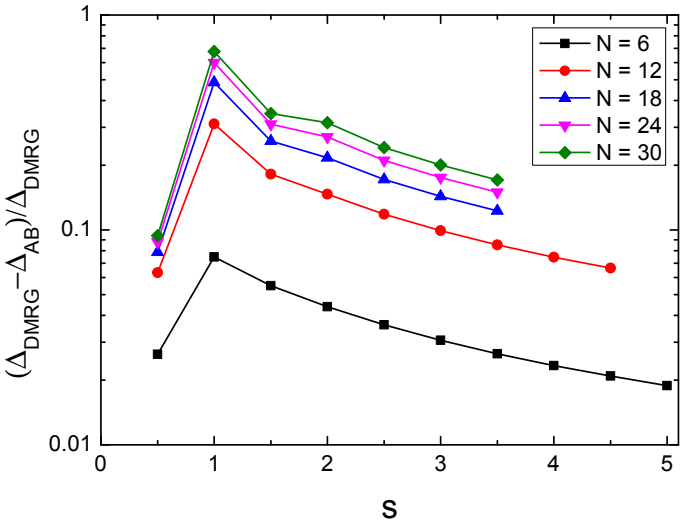

Figure 5.1.: Relative difference of the singlet-triplet gap as predicted by the simple rotational band approximation ($\Delta_{AB} = 4J/N$) and the quasi-exact gap as obtained from DMRG calculations (Δ_{DMRG}) as a function of the single-spin quantum number s. The calculations were performed for several ring lengths N. The parameters which were used for the DMRG calculations are described in the caption of Tab 5.1. The lines are a guide to the eye.

It can be seen for $s > 1/2$ that the smaller the system size and the larger the spin quantum number, the better is the rotational band approximation. For $N = 4$ the rotational band approximation is exact. These results reproduce the findings of Refs. [37, 198]. In most cases, the DMRG results can be considered as quasi-exact with the errors being smaller than the symbol size. For $s = 1$, the rotational band approximation is particularly inaccurate. This behavior is a consequence of the Haldane gap [143, 144], i.e., the finite spin gap of the $s = 1$ spin ring in the

thermodynamic limit (cf. Sec. 3.8.1). In the rotational band approximation, the gap always goes to zero in the thermodynamic limit.

In Ref. [198], the approximation $\Delta \approx \Omega N^{-\alpha}$ was proposed for the singlet-triplet gap of half-integer spin chains as a function of the number of spins. This formula was found to give a very good approximation for large system sizes N and half-integer $s > 1/2$. For small N, deviations from this behavior occurred. Ω and α are functions of the spin quantum number s ($\Omega = 2.73J$ and $\alpha = 0.781$ for $s = 5/2$). The simple rotational band approximation predicts $\Omega = 4J$ and $\alpha = 1$.

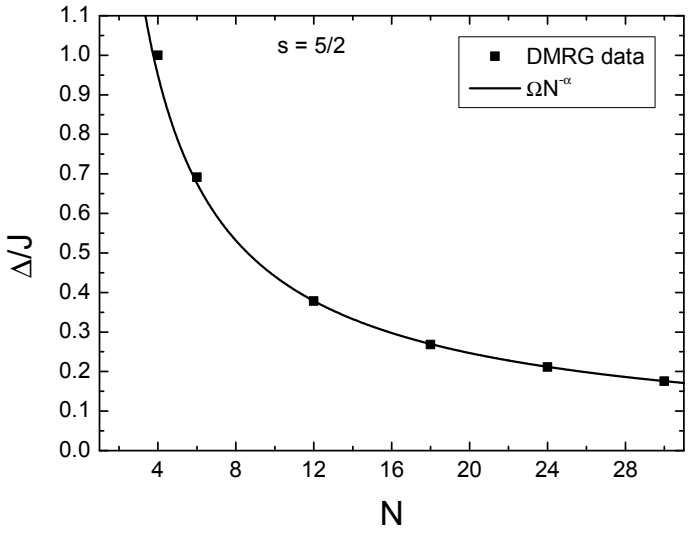

Figure 5.2.: Singlet-triplet gap as obtained by DMRG calculations for $s = 5/2$ as a function of the number of spins N. The line shows the function $\Delta(N) = \Omega N^{-\alpha}$ with $\Omega = 2.73\,J$ and $\alpha = 0.781$ that was proposed in Ref. [198] to describe the behavior of the gap as a function of the chain length. The parameters which were used for the DMRG calculations are described in the caption of Tab 5.1.

In Fig. 5.2 we compare our results for $s = 5/2$, the case that is relevant for Fe^{III} spin rings, with the function $\Delta(N) = \Omega N^{-\alpha}$ that was proposed in Ref. [198]. For $N > 10$, the results nearly perfectly coincide. This can be expected since both DMRG and QMC are very accurate numerical methods for spin rings with an even N.

As a next step we test predictions of the rotational band approximation for the squared transition matrix element $W_1 = |\langle 0|s_j^z|1\rangle|^2$, see Eq. (5.8). Here, $|1\rangle$ denotes the first excited state, i.e., the lowest triplet state. The results are shown in Fig. 5.3 As for the singlet-triplet gaps, the rotational band approximation yields better results for small system sizes and large spin quantum numbers. For $s = 5/2$ and

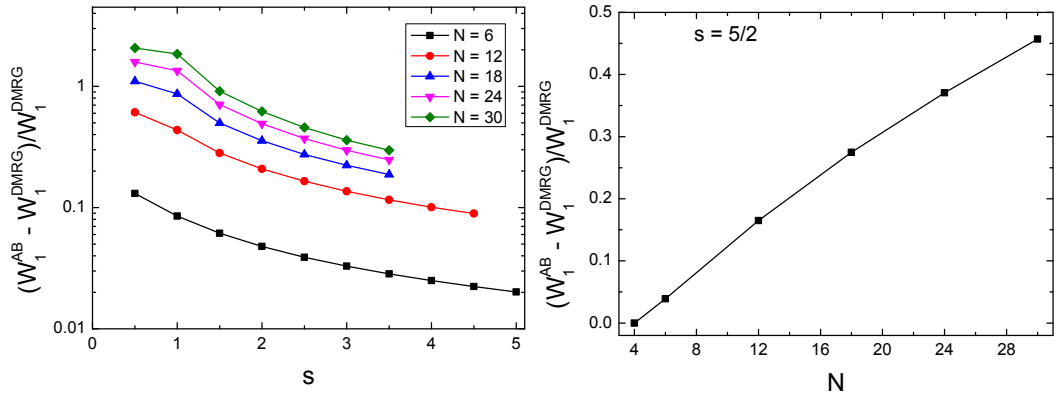

Figure 5.3.: Relative deviation of the squared transition matrix elements $W_1 = |\langle 0|s_j^z|1\rangle|^2$ predicted by the simple rotational band model (W_1^{AB}) from the DMRG results (W_1^{DMRG}). The left part of the figure shows the relative error as a function of s for different chain lengths. The right part shows the relative deviation as a function of N for fixed $s = 5/2$. For the parameters used for the DMRG calculations, see the caption of Tab 5.1. The lines are a guide to the eye.

$N = 18$, the relative deviation of W_1^{AB} (i.e., the rotational band model result) from the (quasi-exact) DMRG result is 27 %. In Ref. [191] it was shown for spin rings that the overlap between the exact wave functions and those of the rotational band approximation is already smaller than 0.7 for $s = 5/2$ and $N = 8$ and decreases with increasing N, so that for $N = 18$ and $s = 5/2$ accurate results cannot be expected anymore. For the singlet-triplet gaps the rotational band approximation yields better results than for the transition matrix elements, but the deviation is still 17 % for $N = 18$ and $s = 5/2$. However, the rotational band approximation can be modified to give more accurate results for the gap (see Refs. [10, 68] and the introductory section of this chapter).

5.2.2. Calculation of the low-energy spectrum using standard and dynamical DMRG

In this subsection we first describe the procedure we have used to calculate the $S = 1$ low-energy spectrum (which can be probed with INS) and to infer the quantum numbers of the energy levels of the (uniform and antiferromagnetic) spin ring with $s = 5/2$ and $N = 18$ using DMRG and DDMRG. We then compare our results with spin-wave theory. We focus exclusively on the case $s = 5/2$ and $N = 18$, but everything that follows is also transferable to spin rings with other spin quantum numbers or lengths. In the previous subsection only the lowest two energy eigenvalues were calculated using standard DMRG. In this subsection we calculate further

(higher-lying) energy levels. Dynamical DMRG (DDMRG) allows for the calculation of dynamical correlation functions also in the higher-energy regime using only four target states (cf. chapter 3), but with a separate run for every ω. On the other hand, standard DMRG allows for the direct calculation of low-lying energy levels and the corresponding wave functions, but the states for all energy eigenvalues up to the desired one have to be simultaneously targeted unless they lie in different symmetry sectors and the DMRG algorithm employs these symmetries. The DMRG algorithm developed for this thesis and the ALPS DMRG program [154] both use only M as a good quantum number. This has the consequence that standard DMRG can (at least for the $s = 5/2$, $N = 18$ system) only be used for the calculation of very few of the energetically lowest $S = 1$ excitations (cf. Fig. 5.4). The more states are simultaneously targeted, the more density matrix eigenstates have to be kept (which increases the computing time) in order to obtain sufficiently accurate results.

Before we proceed, we describe some properties of spin rings and the dynamical correlation functions that are considered in the following. Many of these properties were already described in the previous chapters (cf. Secs. 2.2.3 and 3.8.5). Besides S and M, the shift quantum number k is also a good quantum number of spin rings. The mirror symmetry enforces a $k \leftrightarrow N - k$ symmetry for $k \neq 0, N/2$ [37]. For the (D)DMRG calculations, we consider the following dynamical correlation functions (at zero temperature):

$$S_j^z(\omega) = \sum_n |\langle 0|s_j^z|n\rangle|^2 \delta(\omega + E_0 - E_n) \tag{5.14}$$

and

$$S^z(k,\omega) = \sum_n |\langle 0|S^z(k)|n\rangle|^2 \delta(\omega + E_0 - E_n)\,, \tag{5.15}$$

where

$$S^z(k) = \sum_j e^{\frac{2\pi i k j}{N}} s_j^z\,. \tag{5.16}$$

$|n\rangle$ denotes the energy eigenstate belonging to the eigenvalue E_n. The nondegenerate ground state $|0\rangle$ of an antiferromagnetic Heisenberg spin ring with $N = 18$ and $s = 5/2$ has $S = 0$ and $k_0 = N/2 = 9$ [69]. For the matrix element $\langle 0|S^z(k)|n\rangle$, the following selection rules hold [75]:

$$\Delta k = k + Nz\,,\ z \in \mathbb{Z}\,, \tag{5.17}$$

$$\Delta S = 1\,, \tag{5.18}$$

where $\Delta k = k_n - k_0$. k_n denotes the shift quantum number of energy eigenstate $|n\rangle$. For the matrix elements $\langle 0|s_j^z|n\rangle$ only the second selection rule holds. Additionally

we have the selection rule $\Delta M = 0$ since we use (sums of) s^z operators as the transition operators. Therefore, each peak of the dynamical correlation functions $S_j^z(\omega)$ and $S^z(k,\omega)$ corresponds to a transition from the ground state to an $S = 1$ state, and the excitation energies and the transition matrix elements can be inferred from the peak positions and heights. $|\langle 0|s_j^z|n\rangle|^2$ and $|\langle 0|S^z(k)|n\rangle|^2$ are related via[2]

$$|\langle 0|S^z(k)|n\rangle|^2 = N^2|\langle 0|s_j^z|n\rangle|^2\,, \tag{5.19}$$

if $k_n - k_0 = k + Nz$, $z \in \mathbb{Z}$, so that

$$S_j^z(\omega) = \frac{1}{N^2}\sum_k S^z(k,\omega)\,. \tag{5.20}$$

Furthermore, the following sum rules hold, cf. [37, 75]:

$$\int_{-\infty}^{+\infty} d\omega\, S_j^z(\omega) = \sum_n |\langle 0|s_j^z|n\rangle|^2 = \frac{1}{3}s(s+1) = \frac{35}{12} \tag{5.21}$$

and

$$\sum_k \int_{-\infty}^{+\infty} d\omega\, S^z(k,\omega) = \frac{N^2}{3}s(s+1) = 945\,. \tag{5.22}$$

These sum rules also hold if the delta functions are replaced by Lorentzians with a finite broadening η, as will be done in the following, since in DDMRG calculation a finite broadening is always imposed.

In order to test the accuracy of our results in the low-energy sector, we compare the dynamical correlation functions as obtained from standard DMRG and DDMRG calculations (as already done in chapter 3 for a numerically much less demanding $s = 1/2$ chain). We use the standard DMRG method for the calculation of the lowest excitation energies and the transition matrix elements $|\langle 0|s_j^z|n\rangle|^2$ and $|\langle 0|S^z(k)|n\rangle|^2$ in the $M = 0$ subspace. We also calculate the lowest energy eigenstates in the $M = 1$ and $M = 2$ subspaces. Although we do not use S or k as a good quantum number, it is possible to infer these quantum numbers for the excited states due to the knowledge of the ground state quantum numbers, the selection rules, and the degeneracies of the eigenvalues.

The S quantum numbers of the energy levels shown in Fig. 5.4 can be deduced from the degeneracies of the energy levels with respect to the M quantum numbers. An energy eigenstate with the quantum number S appears in all M subspaces with $|M| \leq S$. Furthermore, the transition matrix elements indicate which energy levels are $S = 1$ states.

[2] This relation can be derived using Eq. (4) of Ref. [37].

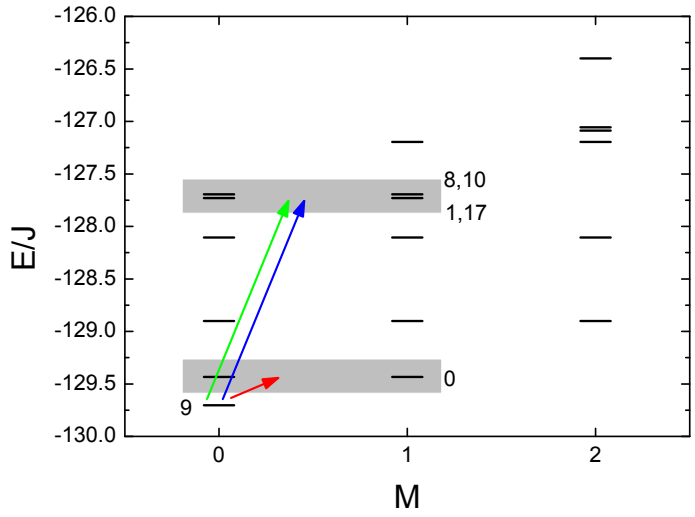

Figure 5.4.: The low-energy spectrum of an antiferromagnetic spin ring with $N = 18$ and $s = 5/2$ as obtained by DMRG calculations. We have used both the ALPS DMRG and our self-written program for these calculations. The lowest 8 energy eigenvalues were calculated in the $M = 0, 1, 2$ subspaces. The arrows indicate the transitions from the ground state to the lowest $S = 1$ states, and the gray boxes mark the lowest $S = 1$ triplets. For these calculations up to $m = 3000$ density matrix eigenstates were kept and the truncated weight is of the order of 10^{-8}. The numbers next to the energy levels denote the shift quantum numbers of the states.

k	ω/J	W
9	0.2683	553.08
8,10	1.9718	77.08
1,17	2.0083	2.07

Table 5.2.: Transition matrix elements $W \equiv |\langle 0|S^z(k)|n\rangle|^2$ and energy differences $\omega \equiv E_n - E_0$ between the ground state and the lowest $S = 1$ states. 8 energy eigenstates had to be simultaneously targeted in the $M = 0$ subspace to get these results (cf. Fig. 5.4). $k = (k_n - k_0 + 18) \bmod 18$ is the shift quantum number relative to the ground state. k_0 denotes the shift quantum numbers of the ground state and k_n the shift quantum numbers of the excited states.

If the transition matrix elements are known, the dynamical correlation functions can be calculated according to their definitions (see Eqs. (5.14) and (5.15)), with the delta functions replaced by Lorentzians with finite width η. We can then compare these results with the results of DDMRG calculations. The DDMRG method directly

calculates the value of a dynamical correlation function with finite broadening for a fixed value of ω. Fig. 5.5 shows the dynamical correlation functions $S^z(k,\omega)$ for $k = 1, 8, 9$ resulting from standard and dynamical DMRG calculations.

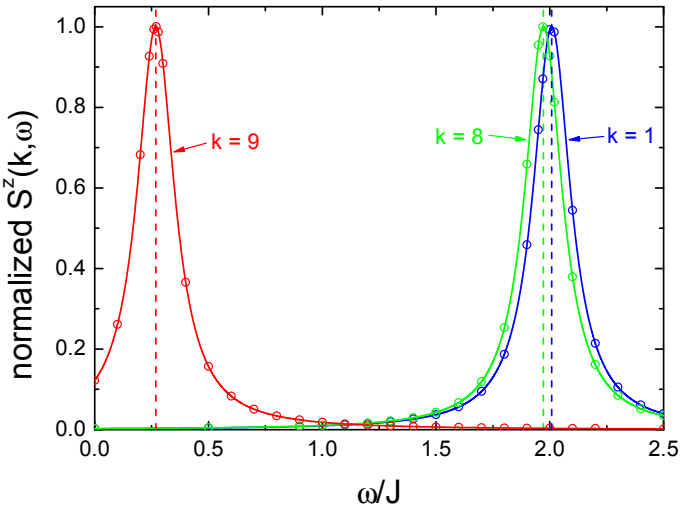

Figure 5.5.: Dynamical correlation functions $S^z(k,\omega)$ (see Eq. (5.15)) for the $N = 18$, $s = 5/2$ spin ring as calculated using standard DMRG (solid lines) and DDMRG (symbols) with a Lorentzian broadening $\eta = 0.1J$. For clarity, the results are normalized to their respective maximum value. The dashed lines indicate the energies as obtained from standard DMRG. The standard DMRG curves are based on the results shown in Tab 5.2. In the DDMRG calculations, 800 density matrix eigenstates have been kept and the truncated weight is at most of the order of 10^{-5}.

The correlation functions are normalized to one since otherwise their heights would differ by several orders of magnitude. One can see a nearly perfect agreement between the two approaches. The DDMRG method has the great advantage that one can also gain information about higher-lying $S = 1$ excitations. The standard DMRG method is limited to low-lying excitations because otherwise too many states would have to be simultaneously targeted.

As a next step the DDMRG method was used to calculate the dynamical correlation functions $S^z(k,\omega)$ for the other relevant k values and several ω values with the goal to extract the excitation energies and the corresponding transition matrix elements. The results are shown in Fig. 5.6. The DDMRG data points were then fitted with Lorentzians of the form

$$f_{\eta,x_0,W}(x) = \frac{W}{\pi}\frac{\eta}{(x-x_0)^2+\eta^2} \tag{5.23}$$

to obtain the transition matrix elements and the positions, i.e., the excitation ener-

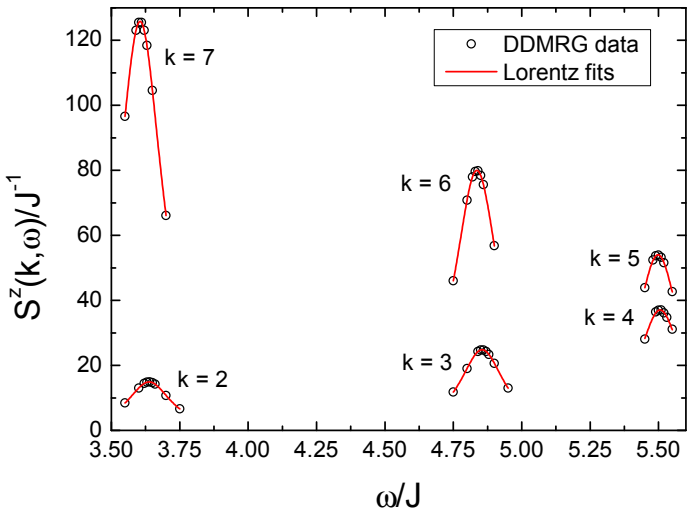

Figure 5.6.: The symbols show $S^z(k,\omega)$ which was calculated for several ω values and several shift quantum numbers k using DDMRG for the $N = 18$, $s = 5/2$ spin ring. The lines show Lorentzians with a fixed width $\eta = 0.1J$ (see Eq. (5.23)) that were used to fit the DDMRG data. These fits yield the excitation energies and the squared transition matrix elements. Note that in Fig. 5.5 the lines were the result of a separate standard DMRG calculation and not the result of a fit. For the DDMRG calculations, up to $m = 800$ density matrix eigenstates were kept and six complete sweeps per frequency point were carried out.

gies. However, this procedure yields reliable results only if the spectrum is not too dense, i.e., if there is only one significant excitation for a specific k or a large enough gap to the next excitation. It turns out that this is the case for the system that we investigate here. Otherwise, it would be necessary to use fits with more than one Lorentzian.

Another possibility to calculate $S^z(k,\omega)$ using DDMRG is to calculate the Fourier transformation of the dynamical correlation functions

$$S^{zz}_{jj'}(\omega) = \sum_n \langle 0|s^z_j|n\rangle\langle n|s^z_{j'}|0\rangle\delta(\omega - E_n + E_0) \tag{5.24}$$

for all j and j', since

$$S^z(k,\omega) = \sum_{j,j'} e^{\frac{2\pi i(j-j')k}{N}} S^{zz}_{jj'}(\omega)\,. \tag{5.25}$$

This approach (i.e., calculating $S^{zz}_{jj'}(\omega)$ and Fourier transforming the data) has the advantage that one only needs to consider a fixed j and can obtain the values of

the dynamical correlation functions (for fixed ω) for all j' in a single DDMRG calculation. For a uniform ring, only one j needs to be considered. When $S^z(k)$ is used as the transition operator, a separate calculation is needed for every k. However, we expect the approach with $S^z(k)$ as the transition operator to be more accurate. We have compared both approaches to validate the results for the energy levels of the spin ring as a function of k. The relative deviation between both approaches was smaller than 6 % for the transition matrix elements and smaller than 0.5 % for the excitation energies.

We note here that using DDMRG to obtain the energy spectrum can only uncover excitations for which the transition matrix elements from the ground state are nonzero and which are not hidden by other transitions with larger weight. However, only those excitations with nonzero weight are relevant for INS simulations. For the calculation of, e.g., the heat capacity one would need all energy eigenvalues.

The results of the fitting procedure are summarized in Tab. 5.3. As before, the k quantum numbers shown in that table are not the absolute quantum numbers of the excited states, but the quantum numbers relative to the ground state.

k	ω/J	W
2,16	3.64	4.68
3,15	4.86	7.79
4,14	5.51	11.64
5,13	5.50	16.98
6,12	4.84	25.13
7,11	3.60	39.53

Table 5.3.: Relative k quantum numbers, excitation energies $\omega = E - E_0$ and squared transition matrix elements W (for the transitions from the ground state) for the uniform $N = 18$, $s = 5/2$ spin ring as obtained by DDMRG calculations. The table summarizes the results of the fitting procedure shown in Fig. 5.6. The errors are difficult to estimate. The results are of course not numerically exact, but we estimate the relative errors of the energies to be much smaller than 1 % and the relative errors of the weights to be smaller than 10 %. These estimates are based on a comparison of the two DDMRG approaches described in the text and calculations with different m values.

Summing up all weights shown in Tabs. 5.2 and 5.3 gives $\sum_k W(k) \approx 923$. Comparing this with the sum rule, Eq. (5.22), shows that approximately 98 % of all weight is captured by the excitations shown in these two tables. However, the estimation of the error of this quantity resulting from the (D)DMRG approach is rather difficult.

The excitation energies as function of the (relative) shift quantum number are

shown in Fig. 5.7. We have found additional excitations resulting in more than one peak for a fixed k, but these excitations have much smaller weights, i.e., much smaller transition matrix elements with respect to the ground state. We will come back to these features in the next subsection.

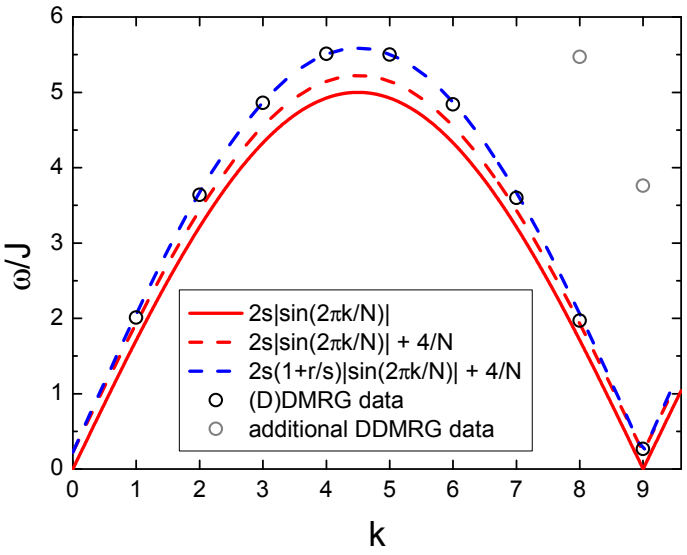

Figure 5.7.: $S = 1$ excitation energies of the uniform $N = 18$, $s = 5/2$ antiferromagnetic spin ring as a function of the shift quantum number (relative to the ground state) as obtained by standard and dynamical DMRG calculations (symbols). The lines show some simple spin-wave theory results (see subsection 5.1.2). The gray symbols denote excitations of the system that cannot be described by the simple spin-wave approaches presented in Sec. 5.1.2.

In Fig. 5.7, we also show the predictions of the different spin-wave approaches described in subsection 5.1.2. The best agreement is obtained if the Oguchi correction and the singlet-triplet gap as predicted by the simple rotational band model are taken into account [25].

The comparison of the weights (the squared transition matrix elements) with the linear spin-wave theory result is shown in Fig. 5.8. Apart from the divergence at $k = 9$, an excellent qualitative agreement can be seen. We can conclude that the $S = 1$ excitations in the uniform spin chain with $N = 18$ and $s = 5/2$ show many features of spin waves [25]. These results are in full agreement with the findings of Ref. [37], where the following general structure of the spectrum of antiferromagnetic spin rings was proposed:

- The energetically lowest states in the S subspaces are well described by the

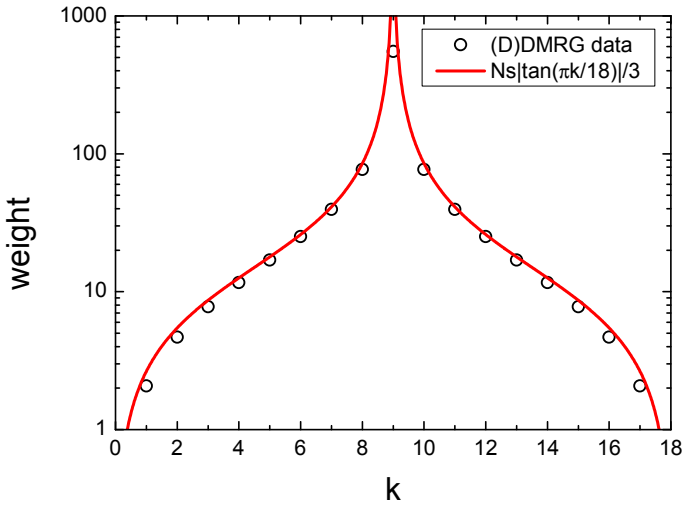

Figure 5.8.: Squared transition matrix elements for the transitions from the ground state to the lowest $S = 1$ states as obtained by standard and dynamical DMRG calculations (symbols). The line shows the result from linear spin-wave theory [195].

rotational band approximation. They have the quantum numbers $k = 0$ or $k = N/2$.

- The $N - 2$ energetically next-higher states in the $S = 1, 2, \ldots$ subspaces with quantum numbers $k = 1, 2, \ldots, N/2 - 1$ (and the corresponding $N - k$ states) are well described by spin-wave theory.

- The states which lie energetically above the spin-wave states are not relevant for low-temperature INS spectra since the squared transition matrix elements are much smaller than for the rotational band or spin-wave states.

Fig. 5.9 shows a comparison of the dynamical correlation function $S^z_j(\omega)$ as calculated by DDMRG with a result from a combination of SWT and the rotational band model. Since $N^2 S^z_j(\omega) = \sum_k S^z(k, \omega)$, we use the following approach:

$$\begin{aligned} S^z_j(\omega) \quad &\approx \quad A\,\delta\left(\omega - \Delta_{AB}\right) \\ &\quad + \sum_{k:\, k\neq 0\, N/2} \frac{s}{3N} \left|\tan\left(\frac{\pi k}{N}\right)\right| \delta(\omega - \omega_{\mathrm{RSWT+RB}}(k))\,, \end{aligned} \tag{5.26}$$

where A is chosen such that the sum rule (5.21) is obeyed and $N = 18$, $s = 5/2$. This ansatz can be explained as follows. The energy of the lowest $S = 1$ excitation is approximated by the simple rotational band model ($\Delta_{AB} = 4J/N$). For the other

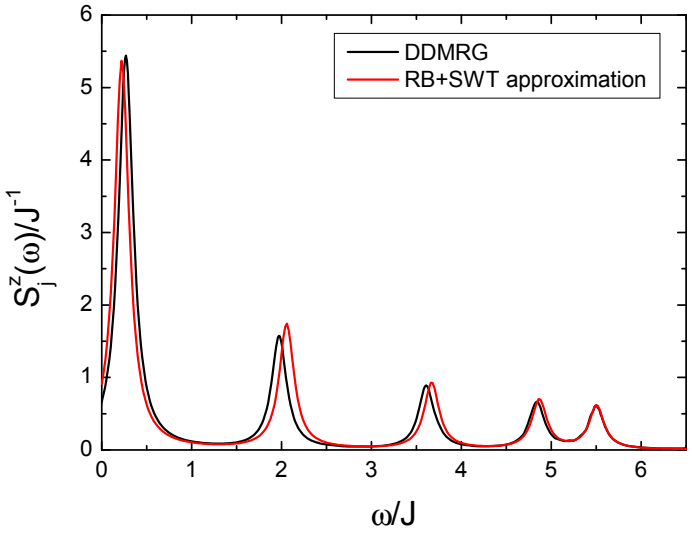

Figure 5.9.: Comparison of the dynamical correlation function $S^z_j(\omega)$ for the $s = 5/2$, $N = 18$ spin ring as calculated using DDMRG (black) and as obtained using a combination of spin-wave theory and rotational band approximation (red), see text for more details about this approximation. For the DDMRG calculations up to $m = 850$ density matrix eigenstates were kept (depending on ω) and the broadening is $\eta = 0.1J$.

excitations (with $k \neq 0, N/2$) we use the spin-wave theory result, Eq. (5.13), with $\omega_{\mathrm{RSWT+RB}}$ (see Eq. (5.12)) instead of ω_{LSWT}.

The agreement of the DDMRG results based on the full Hamiltonian and the approximate dynamical correlation function as proposed above is not perfect but nonetheless very good. This good agreement suggests that an approach that combines the rotational band model and spin-wave theory is well suited for large spin rings.

5.2.3. Additional excitations

A detailed analysis of the dynamical correlation functions $S^z(k, \omega)$ for the $s = 5/2$, $N = 18$ spin ring reveals additional peaks, i.e., small peaks that appear in addition to the large peaks that are well described by the simple spin-wave approaches. However, it is difficult to distinguish between numerical artifacts and "real" excitations. Fig. 5.10 shows two additional peaks that are found for $k = 8$ and $k = 9$ and clearly not numerical artifacts.

A fit with a sum of two Lorentzians yields $\omega = 5.47J$, $W = 1.93$ for $k = 8$ and $\omega = 3.76J$, $W = 3.91$ for $k = 9$. These excitations have much less weight than

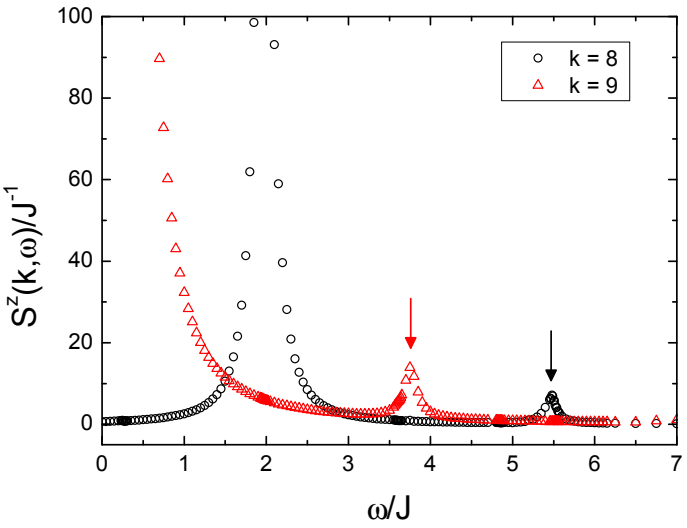

Figure 5.10.: Details of the dynamical correlation function $S^z(k,\omega)$ for $k = 8$ and $k = 9$. The dynamical correlation functions were obtained by Fourier transforming the $S^{zz}_{jj'}(\omega)$ data. For the DDMRG calculations up to 850 density matrix eigenstates were retained. The arrows indicate the additional peaks that cannot be described by the spin-wave theory results described in the text.

the main $k = 8$ and $k = 9$ excitations for which the weights are 77.08 and 553.08. Adding these weights to the sum of the weights of all previously found excitations (see Tabs. 5.2 and 5.3) leads to $\sum_k W(k) \approx 935$. The sum rule predicts a value of 945, so that approximately 99 % of all excitations that have nonzero weight have been found using the procedure described in this and the previous subsection.[3]

5.2.4. Dynamical correlation function for an excited reference state ($S = 2$ excitations)

Up to now we have calculated the dynamical correlation function for the $s = 5/2$, $N = 15$ spin ring at zero temperature, i.e., with the ground state $|0\rangle$ as the "reference state". "Reference state" means that only transitions from this state are accounted for in the dynamical correlation functions. Since the ground state of spin-s antiferromagnetic Heisenberg rings with an even number of spins has $S = 0$, only transitions to states with $S = 1$ and $M = 0$ contribute to the dynamical correlation functions $S^z_j(\omega)$ and $S^z(k,\omega)$. To gain information about excitations from states other than the ground state, we use an excited state as the reference state. Such excitations are

[3]This value is based on the assumption that the (D)DMRG results are exact. The error of the results is, however, difficult to estimate.

relevant for dynamical correlation functions at temperatures $T > 0$. We consider the $M = 0$ and $M = 1$ components of the lowest $S = 1$ energy eigenstate for this purpose and employ the DDMRG technique to calculate

$$S_j^{z,r}(\omega) = \sum_n |\langle r|s_j^z|n\rangle|^2 \delta(\omega - E_n + E_r)\,, \tag{5.27}$$

where $|r\rangle$ denotes the reference state with the energy E_r. As in all previous calculations, a finite broadening is introduced. Choosing the $M = 0$ component of the energetically lowest $S = 1$ state as the reference state yields different results than choosing the $M = 1$ component as the following calculations show. Let the reference state $|r\rangle$ have the quantum numbers S and M. We denote a state with these quantum numbers $|SM\rangle$. Using the Wigner-Eckart theorem, we can calculate for which S' and M' the matrix elements $\langle SM|s_j^z|S'M'\rangle$ are zero.

The Wigner-Eckart theorem tells us that [73]

$$\langle SM|s_j^z|S'M'\rangle = (-1)^{S-M} \begin{pmatrix} S & 1 & S' \\ -M & 0 & M' \end{pmatrix} \langle S||s_j^z||S'\rangle\,, \tag{5.28}$$

where $\langle S||s_j^z||S'\rangle$ denotes a reduced matrix element (which is independent of M and M') and $\begin{pmatrix} S & 1 & S' \\ -M & 0 & M' \end{pmatrix}$ is a $3j$ symbol. If we now consider the case $S = S' = 1$, $M = M' = 0$ and calculate the $3j$ symbol explicitly, we find that it is zero. Furthermore, only transitions with $\Delta M = 0$ are possible. This has the following consequences: If we use an energy eigenstate $|S = 1, M = 0\rangle$ as the reference state, we only probe transitions to states from the $S = 0$ and $S = 2$ subspaces (i.e., $\Delta S = \pm 1$). Transitions to $S = 0$ states are not possible for a $S = 1$, $M = 1$ reference state. Transitions to $S = 2$ states are possible for both reference states. We can calculate the ratio of the squared transition matrix elements for transition from the two reference states to the same $S = 2$ multiplet:

$$\frac{|\langle S = 1, M = 0|s_j^z|S' = 2, M' = 0\rangle|^2}{|\langle S = 1, M = 1|s_j^z|S' = 2, M' = 1\rangle|^2} = \frac{4}{3}\,. \tag{5.29}$$

Using the $S = 1$, $M = 0$ state as the reference state requires the DDMRG program to be slightly modified. One needs to simultaneously target both the ground state and the first excited state in the $M = 0$ subspace. In our calculations, both energy eigenstates are targeted with equal weight. The first excited state is then used for the calculation of the state $s_j^z|r\rangle$ and of the correction vector. The results of the DDMRG calculations are shown in Fig. 5.11.

It was found in Ref. [37] for smaller spin rings that the $S > 1$ energy levels have virtually the same structure as the $S = 1$ energy levels. Fig. 5.11 also contains

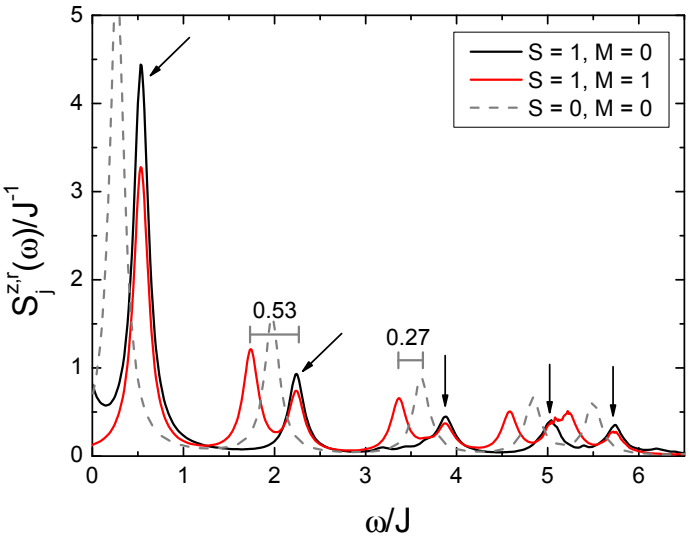

Figure 5.11.: Dynamical correlation functions of the $N = 18$, $s = 5/2$ spin ring for different "reference states" (see text). The arrows indicate transitions to $S = 2$ states. That these peaks of the correlation function for the $S = 1, M = 0$ reference state have more weight than those of the function with the $S = 1, M = 1$ reference state can be explained using Eq. (5.29). For the assignment of the other peaks, see text and Fig. 5.12. The gray dashed curve is the same as the black curve in Fig. 5.9.

the dynamical correlation function with the ($S = 0$) ground state as the reference state. One can see that for every peak of this function (corresponding to an $S = 0 \to S' = 1$ transition), the dynamical correlation function with the reference state with $S = 1$, $M = 1$ has one peak on the left and one on the right. The peaks on the left correspond to transitions from the energetically lowest $S = 1$ state to other $S = 1$ states, since the peaks are approximately shifted by the value of the singlet-triplet gap, which is $\Delta_{0\to1} = 0.2683$. The peaks shifted to the right correspond to transitions from the lowest $S = 1$ state to $S = 2$ states. The gap between the energetically lowest $S = 1$ and $S = 2$ states is $\Delta_{1\to2} = 0.5339$. This value can easily be calculated using DMRG and is approximately twice as large as the singlet-triplet gap. Based on these results the spectrum can be deduced, which is shown in Fig. 5.12.

We mention that the dynamical correlation functions show some very small additional features, e.g., around $\omega = 3.3J$, for which it is not clear whether they correspond to real excitations or are numerical artifacts. Here, more extensive numerical calculations would be needed to clarify this question. However, these features are extremely small and would thus not be relevant for the simulation of INS spectra.

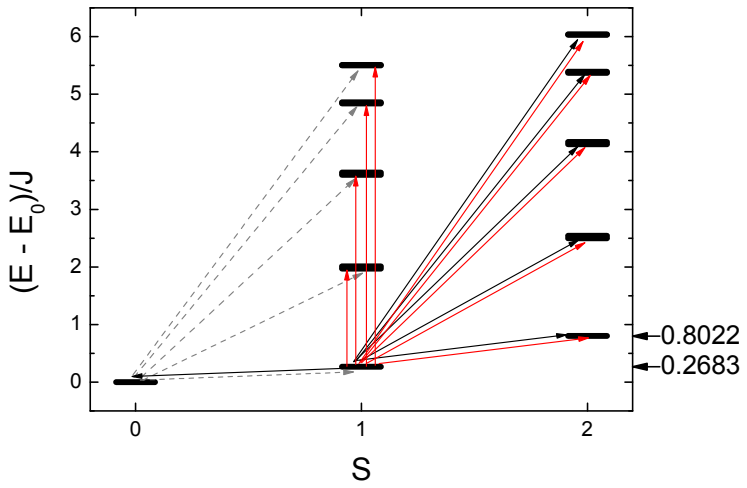

Figure 5.12.: Schematic low-energy spectrum of the uniform antiferromagnetic Heisenberg ring with $N = 18$ and $s = 5/2$. The arrows indicate the possible transitions from the ground state (dashed gray arrows), the lowest $S = 1$, $M = 1$ energy eigenstate (red), and the lowest $S = 1$, $M = 0$ state (black).

5.3. Fe_{18}

In this section, we focus on the molecule $[Fe_{18}(pdH)_{12}(O_2CEt)_6(NO_3)_6]$ (in short Fe_{18}, see Fig. 5.13) [9], which is the largest iron spin ring synthesized to date. Since it consists of $N = 18$ spins with $s = 5/2$, the Hilbert space dimension is about 10^{14} and thus much too large for exact diagonalization methods on present-day computers. In Ref. [10] the effective two-spin Hamiltonian $H_{AB}^{\text{Heisenberg}} + H_{AB}^{\text{single-ion}}$ (see Eqs. (5.5) and (5.7)) was used to calculate magnetic properties of this system in the low-energy regime. Ref. [10] focused on an investigation of the lowest rotational band, i.e., on the energetically lowest states in the total spin (S) subspaces. In contrast, the experimental INS results [25, 193] that are shown in the next subsection focus on higher-lying excitations. We use standard and dynamical DMRG methods (applied to the full 18-spin Hamiltonian) to calculate the part of the energy spectrum that is relevant for the simulation of INS experiments. The calculated energy spectra and INS intensities are then compared with the experimental data. It turns out that a uniform model as discussed in the previous section cannot explain the experimental results. However, using a more general model with two different coupling constants, we find a single set of parameters that leads to an excellent reproduction of the experimental data [25]. All experimental data that are shown in this section were provided by J. Nehrkorn from the "Molecular Nanomagnets" group of O. Waldmann, Universität Freiburg.

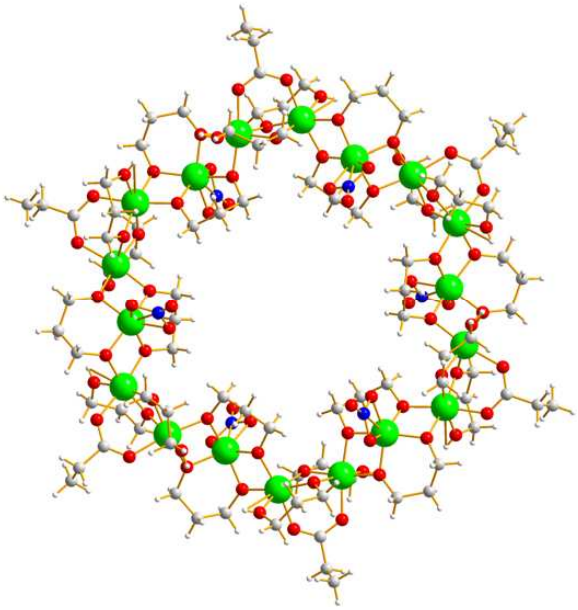

Figure 5.13.: Depiction of the molecule $[Fe_{18}(pdH)_{12}(O_2CEt)_6(NO_3)_6]$, in short Fe_{18} (Fe: green, O: red, N: blue, C: gray, and H: white) [9, 25]. It consists of $N = 18$ antiferromagnetically coupled Fe^{III} ions ($s = 5/2$). This molecule exhibits crystallographic C_6 symmetry.

5.3.1. Experimental results

The Fe_{18} compound that is investigated in this chapter was first reported in Ref. [9] and a singlet ground state was deduced based on susceptibility measurements. Further experimental and theoretical investigations on this compound were carried out in Ref. [10], where among other things the low-temperature magnetization curve, the position of the magnetization steps, and low-energy INS data were measured and analyzed. The low-energy INS spectrum shows two cold peaks, i.e., peaks which result from transitions from the ground state to excited states. The peaks are located at 0.3 meV (called "peak Ia" in the following) and 1.0 meV ("peak Ib") and correspond to transitions from the $S = 0$ ground state to the anisotropy-split lowest $S = 1$ state. If anisotropic terms are present, S is not a good quantum number anymore, of course. However, for small anisotropy D it is possible to approximately assign a total spin quantum number S to a state.

Very recently, new high-energy INS and susceptibility measurements were performed on Fe_{18} powder samples [25]. The high-energy INS data were measured at the direct time-of-flight spectrometer FOCUS [199] at the Paul Scherrer Institut (Villigen, Switzerland) with fixed incoming neutron wavelengths $\lambda = 3.2$ Å and

2.26 Å. The experimental resolution is 0.43 meV for $\lambda = 3.2$ Å and 1.1 meV for $\lambda = 2.26$ Å. The INS data are shown in Fig. 5.14.

An analysis yields cold peaks that are located approximately at 3.0 meV (II), 8.5 meV (III), and 12.0 meV (IV) [25]. The small feature at 6 meV is probably a spurion or a phonon excitation. The background due to phonon scattering was estimated using the so-called Bose correction which has already been successfully applied to other magnetic molecules [192, 200].

Effective two-spin Hamiltonian: As already noted in the introduction of this section, the effective two-spin Hamiltonian $H_{AB}^{\text{Heisenberg}} + H_{AB}^{\text{single-ion}}$ was used in Ref. [10] for Fe_{18} to simulate low-energy INS data (peaks Ia and Ib) and the low-temperature magnetization curve. The parameters found in Ref. [10] are $a_1 J \approx 0.44$ meV and $b_1 D \approx 0.0018$ meV. These values can be related to the parameters J and D of the uniform ring Hamiltonian $H_{\text{Heisenberg}} + H_{\text{single-ion}}$ (with $N = 18$ and $s = 5/2$, see Eqs. (5.2) and (5.3)). Using DMRG we have tried to find "optimal" parameters a_1 and b_1, such that the low-energy spectra of $H_{AB}^{\text{Heisenberg}} + H_{AB}^{\text{single-ion}}$ and the 18-spin Hamiltonian $H_{\text{Heisenberg}} + H_{\text{single-ion}}$ coincide.

For these calculations the ALPS DMRG and exact diagonalization codes [154,155] were used. We have proceeded in two steps: a_1 is determined by simply taking the value of the singlet-triplet gap of the full Heisenberg Hamiltonian (without anisotropy) with $J = 1$. For the estimation of b_1, we directly compare (for fixed a_1) the spectra of the dimer Hamiltonian $H_{AB}^{\text{Heisenberg}} + H_{AB}^{\text{single-ion}}$ and the full Hamiltonian (with anisotropy) for several values of b_1 and D. We obtain $a_1 = 0.26826$, calculated with up to $m = 3000$ density matrix eigenstates per block so that the truncated weight is smaller than 10^{-9}. Fig. 5.15 shows the results of calculations for $J = 1$ and three different D values. ($D = 0.016$ corresponds to the $|D/J|$ ratio which was estimated for Fe_{18} in Ref. [10].) In the plot, the gaps between the ground state and the two lowest excited states ($\Delta E_1 = E_1 - E_0$ and $\Delta E_2 = E_2 - E_0$) of the full Hamiltonian and of the effective two-spin Hamiltonian are compared.

It can be seen that for $b_1 \approx 0.063$ (rounded to two significant digits) a very good agreement with absolute errors smaller than 0.005 is obtained. A perfect agreement cannot be obtained for $D \neq 0$ since a_1 has been fixed. As expected, however, the agreement becomes better for smaller values of D. Our final results are $a_1 = 0.26826$ and $b_1 = 0.063$. (The simple rotational band approximation would give $a_1 = 2/9 \approx 0.22222$.)

Using the optimal values for a_1 and b_1, the parameters $a_1 J \approx 0.44$ meV and $b_1 D \approx 0.0018$ meV, which were found in Ref. [10], correspond to $J \approx 1.64$ meV, $D \approx 0.029$ meV for the uniform Heisenberg model with additional anisotropy. However, as turns out in the next subsection, a uniform model cannot explain the high-energy INS data.

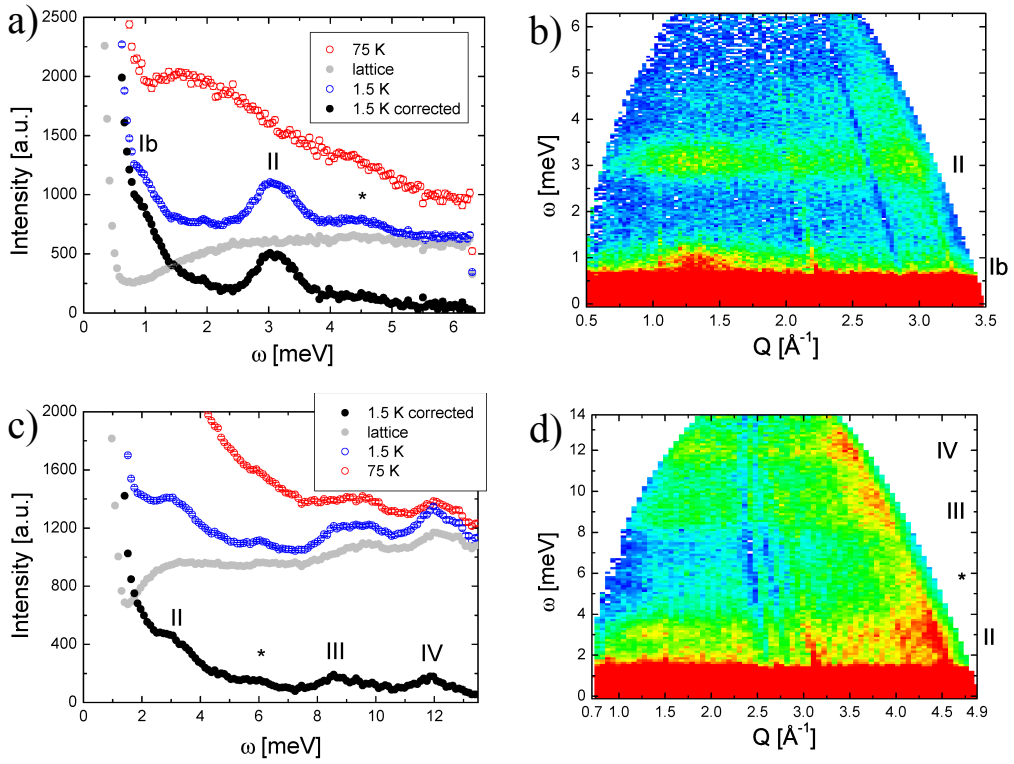

Figure 5.14.: a) Experimental INS spectra with incoming neutron wavelength $\lambda = 3.2$ Å recorded at temperatures of 1.5 (blue symbols) and 75 K (red symbols). The data were summed over all detector banks. The 75 K data are used to estimate lattice scattering at 1.5 K (gray symbols) which is subtracted from the 1.5 K data to obtain lattice-corrected data (black symbols). The "II" marks an observed transition and the asterisk a feature that is probably a spurion or a lattice feature. b) Experimental INS intensity of the (uncorrected) 1.5 K data shown in a) as a function of momentum and energy transfer. Blue indicates low intensity and red high intensity. c) Experimental INS spectra with incoming neutron wavelength $\lambda = 2.26$ Å recorded at temperatures of 1.5 (blue symbols) and 75 K (red symbols). The data were again summed over all detector banks. The 75 K data is used to estimate lattice scattering at 1.5 K (gray symbols) which is subtracted from the 1.5 K data to obtain lattice-corrected data (black symbols). d) Experimental INS intensity of the (uncorrected) 1.5 K data shown in c) as a function of momentum and energy transfer. The labels ("II", "III", and "IV") indicate the observed transitions and the asterisk a feature that is probably a spurion or a lattice feature. [25, 193]

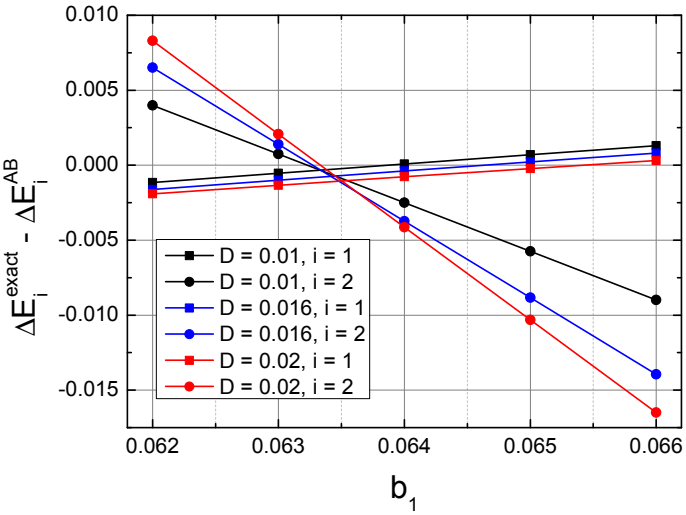

Figure 5.15.: Difference between the energy gaps resulting from the dimer Hamiltonian $H_{AB}^{\text{Heisenberg}} + H_{AB}^{\text{single-ion}}$ (see Eqs. (5.5) and (5.7)), which follows from the refined rotational band model, and the energy gaps as obtained by DMRG calculations for the full 18-spin Hamiltonian $H_{\text{Heisenberg}} + H_{\text{single-ion}}$ (see Eqs. (5.2) and (5.3)). ΔE_1 denotes the gap between the $M = 0$ ground state and the energetically lowest $M = 1$ state, and ΔE_2 denotes the energy gap between the ground state and the next-higher $M = 1$ state. For the calculations using the two-spin Hamiltonian exact diagonalization was used. The lines are a guide to the eye.

5.3.2. Simulation of the high-energy INS data

In the following, we try to fit the experimental high-energy INS data obtained for $\lambda = 2.26$ Å. A formula for the simulation of time-of-flight INS data [78] was given earlier in this thesis in Sec. 2.3.2. That formula required an integration of the scattering function over the momentum with the integration limits depending on the minimum and maximum scattering angles and the energy transfer ω. For the FOCUS spectrometer the minimum scattering angle is 10°, and the maximum angle is 130° [199]. We approximate the integral by a sum and use the following simplified formula for the theoretical simulation of the INS intensity $I(\omega)$ [79, 80]:

$$I(\omega) \approx \sum_i{}' F^2(Q_i) S^{zz}(Q_i, \omega)\,, \tag{5.30}$$

where the Q_i are equally distributed with a constant step width $\Delta Q = Q_{i+1} - Q_i$ in the interval $[Q_{\min}(\omega), Q_{\max}(\omega)]$. $F(Q)$ denotes the form factor of an Fe^{III} ion [80]. DDMRG was used to calculate the functions $S^{zz}_{jj'}(\omega)$ for all j, j', which can then be used to calculate $S^{zz}(Q, \omega)$ (see Eq. (2.35)). The symmetries of the model can be

exploited so that – depending on the ansatz for the Hamiltonian – not all j need to be considered. For example, for the uniform ansatz it suffices to consider one fixed j. We consider only $T = 0$ in our calculations and furthermore neglect the anisotropy. As will be shown later, these approximations are justified.

As a first ansatz we use the uniform Heisenberg model (see Eq. (5.2)), i.e., with only a single exchange constant $J = 1.64$ meV, as has been proposed in Ref. [10]. However, a direct comparison of the theoretical with the experimental results (see Fig. 5.16) shows large discrepancies as regards the high-energy excitations. The peaks of the simulated curve occur approximately at $0.27J$, $2.0J$, $3.6J$, $4.8J$, and $5.5J$ (cf. the previous section). Therefore it is not possible to find a single J for which more than two INS peaks can be reasonably reproduced.

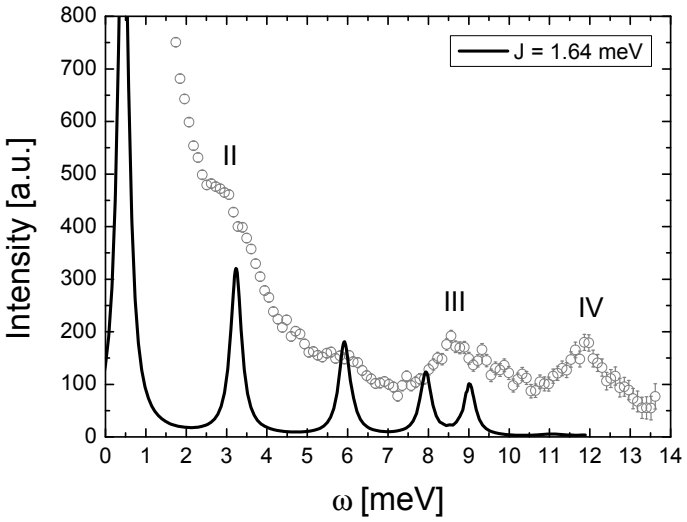

Figure 5.16.: Comparison of the experimental lattice-corrected high-energy INS data [25, 193] (symbols), which were obtained at $T = 1.5$ K, with the theoretical (zero-temperature) INS intensity (black line) calculated on the basis of the uniform Heisenberg model with $J = 1.64$ meV. Equation (5.30) was used for the calculation. The broadening parameter of the theoretical curve is $\eta = 0.1J$ and thus not adapted to the experimental resolution. The calculation was performed for excitation energies up to 12 meV since the analysis of the previous section indicates that all major peaks lie below 12 meV.

The peaks as calculated using DDMRG are at different positions than the experimentally obtained features. Also, the DDMRG results show no sign of a large peak at 12 meV. Furthermore, QMC simulations of the susceptibility were performed by J. Schnack (see Ref. [25]). These calculations also indicate that a "single-J" Heisenberg model is not sufficient, since it cannot explain the experimental susceptibility

and the high-energy INS data.

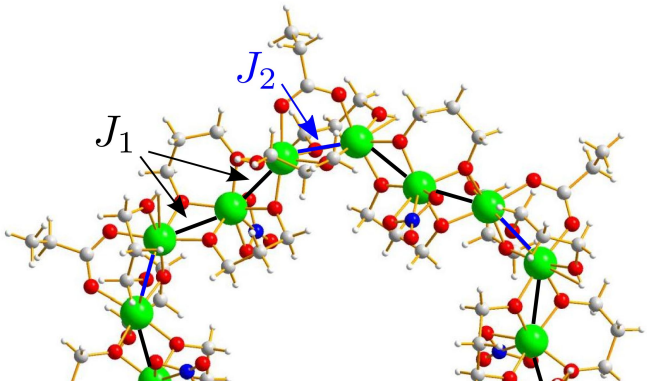

Figure 5.17.: Part of the Fe_{18} molecule [25] and illustration of the "two-J model" (see Eq. (5.31)). The thick blue and black lines shall illustrate the antiferromagnetic couplings between the Fe^{III} ions, i.e., the $s = 5/2$ spins. Two coupling constants are used in this model: J_1 (black lines) and J_2 (blue lines).

As a next step we have considered a more general Heisenberg model with two different coupling constants J_1 and J_2:

$$H_{\mathrm{two}-J} = \sum_{i=1}^{6} \{J_1 \vec{s}_{3i} \cdot \vec{s}_{3i+1} + J_1 \vec{s}_{3i+1} \cdot \vec{s}_{3i+2} + J_2 \vec{s}_{3i+2} \cdot \vec{s}_{3i+3}\} \ . \tag{5.31}$$

This more general model is probably more appropriate for the molecule Fe_{18}, which has C_6 symmetry [25], cf. Fig. 5.13. The coupling constants follow the sequence $J_1 - J_1 - J_2$ in this model, which has already been successfully used for an Fe_{18} molecule [184] different from the one that is investigated in this work. However, in Ref. [184], only the results of susceptibility measurements were analyzed.

Spin-wave theory calculations were performed for this model by N. Ivanov with the goal of finding parameters for which the experimental peak positions match the spin-wave excitation energies [25]. In the previous section, we have shown that a combination of spin-wave theory (SWT) and the rotational band model can approximate the excitations of the uniform model very well. However, it is a priori not clear how accurate spin-wave theory is for the "two-J" model. The SWT calculations yielded two equally good parameter sets, one with $J_1/J_2 \approx 0.3$ and one with $J_1/J_2 \approx 3$ [25]. These ratios were used as a starting point for the DDMRG calculations in which several parameter sets were tested. However, since the DDMRG calculations are extremely time-consuming and the calculations have to be performed separately for each ω, we have, as a first step, calculated the INS intensity with a rather large broadening $\eta = 0.5$ meV and only for some ω values in the regions around the peak

positions as found in the experiments. The broadening corresponds to a FWHM (full width at half maximum) of 1 meV and thus approximately to the experimental resolution (1.1 meV). Unfortunately, an automized fitting routine could not be employed due to the complexity of the calculations. We have always tried to fit the position of peak II very accurately and tested the influence of small parameter variations from that starting point (and based on the SWT input). We discuss the influence first for the case $J_1 > J_2$. A small variation of J_2 affects the complete spectrum and all peak positions depend approximately linearly on the variation, whereas a variation of J_1 mainly influences the peak positions of the high-energy spectrum. The low-energy part is nearly unaffected. For the case $J_1 < J_2$ the results are very similar with J_1 and J_2 simply interchanged in the discussion above.

For some parameter sets we have performed large-scale calculations for enough ω values to get a nearly continuous curve. In the case $J_1/J_2 \approx 0.3$, only a rather rough qualitative agreement can be obtained (see left part of Fig. 5.18). The position of peak II is matched, but the DDMRG spectrum shows an additional feature between the experimental peaks III and IV. This "three-peak" structure of the high-energy part of the theoretical spectrum is almost unaffected by small parameter variations. The best-fit result for the model with $J_1 < J_2$ is $J_1 = 1.42$ meV and $J_2 = 4.57$ meV. As already noted above, these parameters are not the result of an automized fitting procedure, but were determined "by hand".

The agreement is much better for the case $J_1/J_2 \approx 3$ (see Fig. 5.18). We obtain a very good quantitative agreement for the parameter set $J_1 = 2.88$ meV and $J_2 = 1.02$ meV.

Based on the results of parameter variations in the DDMRG calculations, our error estimate is about 0.15 meV for J_1 and about 0.05 meV for J_2. The position of the simulated peak II is mainly determined by J_2 (for the case $J_1 > J_2$) so that the smaller error for J_2 results from the more precisely measured position of experimental peak II compared to the positions of peaks III and IV (cf. Fig. 5.14). Within these error bounds, the positions of all experimental high-energy peaks can be matched in the DDMRG simulation. The magnetic susceptibility is also reproduced excellently using these exchange parameters [25]. However, the susceptibility is equally well reproduced with the parameters $J_1 = 1.42$ meV and $J_2 = 4.57$ meV, so that on the basis of the susceptibility measurements alone it would not be possible to prefer one parameter set over the other.

All theoretical spectra that are shown in this section are zero-temperature excitation spectra. However, the high-energy INS experiments were carried out at a temperature of 1.5 K. The gap between the ground state and the first excited state was obtained as 0.3 meV in the experiments (peak Ia). For a temperature of 1.5 K we estimate the ground state population to be larger than 90 %. A finite temperature leads to the appearance of additional peaks which result from transitions from excited states. However, the positions of the peaks resulting from transitions from

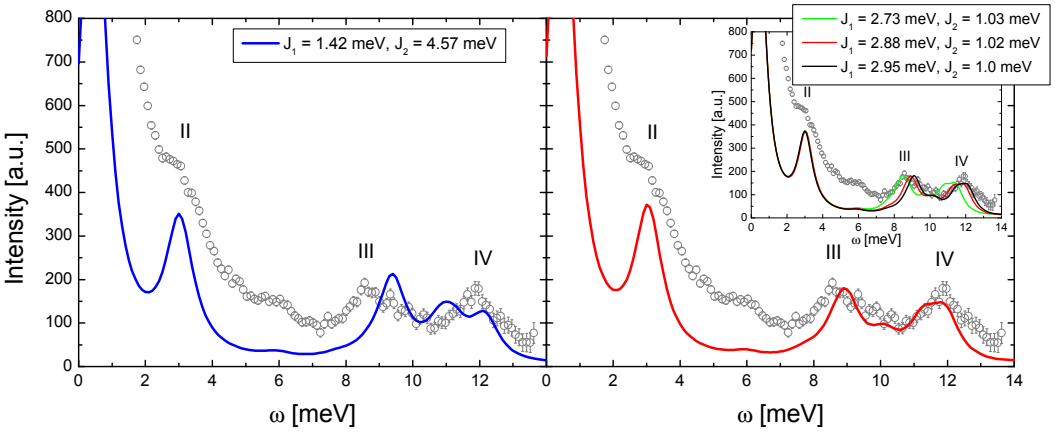

Figure 5.18.: Comparison of the experimental lattice-corrected high-energy INS data [25, 193] (symbols), which were obtained at $T = 1.5$ K, with the theoretical (zero-temperature) INS intensity (lines) calculated for the two-J model, see Eq. (5.31). Eq. (5.30) was used for the calculation of the INS intensities. Two corresponding $S^{zz}(Q,\omega)$ plots are shown in appendix A.2. The broadening of the theoretical curves is $\eta = 0.5$ meV, which results in a FWHM of 1 meV and thus approximately corresponds to the experimental resolution (1.1 meV). The best-fit results are shown, as well as the influence of small parameter variations (inset). For the DDMRG calculations, $m = 600$ states were kept.

the ground state are not affected, only their heights. With such a large ground state population, transitions from the ground state should clearly dominate and the comparison of the zero-temperature DDMRG results with the 1.5 K experimental data is justified.

Besides the finite temperature, we have so far also neglected the single-ion anisotropy in our calculations. It was shown in Ref. [192] for a ring molecule with $N = 8$ and $s = 5/2$ that the anisotropy mainly influences the lowest $S = 1$ multiplet and that the influence on the higher-lying excitations is only very weak. The importance of anisotropy in Fe_{18} is investigated in the next subsection.

5.3.3. Influence of the uniaxial anisotropy

Up to now no anisotropy was considered and the DDMRG calculations were performed for an isotropic model. In this subsection, we calculate the low-energy spectrum of $H_{\text{two}-J}+H_{\text{single-ion}}$ (for our best-fit result $J_1 = 2.88$ meV and $J_2 = 1.02$ meV) for several values of D using the ALPS DMRG program.

To test the influence and find the correct value of D, we first calculate the gaps between the energies of the ground state and the two next-higher-lying states ($\Delta E_1 =$

$E_1 - E_0$ and $\Delta E_2 = E_2 - E_0$). In the INS experiments the corresponding peaks were observed at 0.3 meV (peak Ia) and 1.0 meV (peak Ib) [10]. Now, a value of D has to be found such that $\Delta E_1 \approx 0.3$ meV and $\Delta E_2 \approx 1.0$ meV.

D [meV]	ΔE_1 [meV]	ΔE_2 [meV]	χ^2 [(meV)^2]
0.029	0.29944	0.98401	$2.56083 \cdot 10^{-4}$
0.030	0.29736	1.00321	$1.72479 \cdot 10^{-5}$
0.031	0.29537	1.02233	$5.20005 \cdot 10^{-4}$

Table 5.4.: The excitations from the ground state to the next $M = 0$ state and the lowest $M = 1$ state as calculated using DMRG for $J_1 = 2.88$ meV, $J_2 = 1.02$ meV, and several D values (using $H_{\text{two}-J} + H_{\text{single-ion}}$). The excitations are compared with the experimentally obtained position of peaks Ia and Ib (see Ref. [10]). The measure of deviation is defined as $\chi^2 \equiv (\Delta E_1 - 0.3 \text{ meV})^2 + (\Delta E_2 - 1.0 \text{ meV})^2$.

Clearly, the best result is obtained for $D = 0.030$ meV (see Tab. 5.4), which is very close to the D value that has been obtained in the previous Fe_{18} study [10] on the basis of the simplified two-spin Hamiltonian ($D = 0.029$, see also the end of Sec. 5.3.1).

Next, we compare the spectra of the two-J Hamiltonian with $D = 0$ and $D = 0.03$ meV to estimate the influence of the anisotropy on the higher-lying excitations. The comparison is shown in Fig. 5.19. The main S contributions to the energy eigenstates in the case $D > 0$ were deduced from the degeneracies of the levels and their behavior for different M and D values. This procedure is, however, only possible if the D value is sufficiently small so that the spin multiplets can be identified in the spectra. For $D = 0.030$ meV this is definitely the case.

It can be seen that the splitting of the lowest $S = 1$ state is 0.7 meV for $D = 0.03$ meV. This value is much larger than the splitting of the next two, nearly degenerate $S = 1$ states, which is approximately 0.3 meV and thus smaller than the experimental resolution. The experimental resolution was 0.43 meV and 1.1 meV, respectively (see subsection 5.3.1). This result is a clear indication that for Fe_{18} the influence of D on higher-lying states can be neglected in an analysis of high-energy INS data and in accordance with the findings of Ref. [192] (where an iron spin ring with $N = 8$ spin was investigated).

5.3.4. Magnetization curves

We have seen that the different models which have been considered so far – $(J_1, J_2) =$ (1.64 meV, 1.64 meV), (1.42 meV, 4.57 meV), and (2.88 meV, 1.02 meV) – led to very different results for the high-energy spectrum. However, the low-energy spectrum (which is relevant for the peaks Ia, Ib, and II) is very similar for all three models.

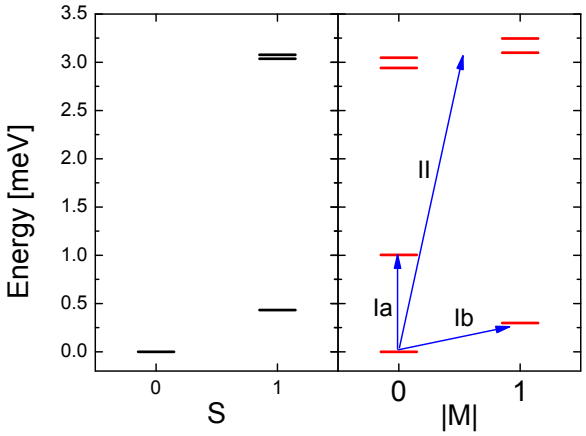

Figure 5.19.: The ground state and the energetically lowest $S = 1$ triplets of the two-J Hamiltonian with $J_1 = 2.88$ meV and $J_2 = 1.02$ meV as calculated using standard DMRG. The black bars show the spectrum for $D = 0$ and the red bars for $D = 0.03$ meV. For $D > 0$, S is no longer a good quantum number and the multiplets are split into the $M = 0, \pm 1$ components. The arrows indicate the experimentally observed transitions. The transitions to the states around 3 meV appear as one peak in the experimental INS spectra.

In this subsection we calculate the zero-temperature magnetization curves for the three models mentioned above. We again neglect the anisotropy in this subsection since it probably only affects the positions of the first magnetization steps. Fig. 5.20 shows the resulting zero-temperature curves for all three models.

The results are very interesting. The magnetization curves are virtually identical up to 25 Tesla. The step widths of the single-J magnetization curve are approximately the same for all steps (apart from the very last steps), as would also be the case for the rotational band approximation. The magnetization curves for the other two models deviate from this behavior. Up to approximately 100 T, the two models with $J_1 \neq J_2$ give very similar magnetization curves and considerable differences appear only at even higher fields. The magnetization curve for $J_1 = 1.42$ meV and $J_2 = 4.57$ meV shows two magnetization plateaus at higher fields. Plateaus in zero-temperature magnetization curves usually emerge in geometrically frustrated spin systems [201]. This system is, however, not geometrically frustrated so that the emergence of a plateau is an interesting effect.

We have also calculated the local magnetizations for the two models with $J_1 \neq J_2$. Local moments in spin rings can, e.g., be probed with NMR [202]. The local magnetizations for the $J_1 = J_2$ model would simply be proportional to the total magnetization curve. The results are shown in Fig. 5.21.

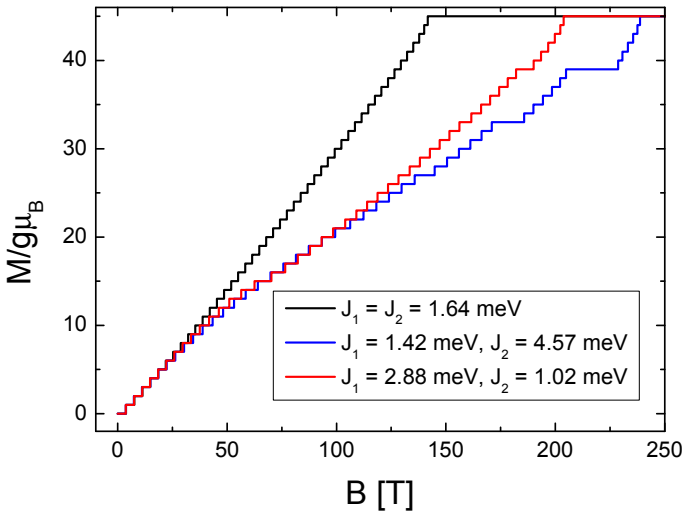

Figure 5.20.: Comparison of the zero-temperature magnetization curves for three different parameter sets as obtained by standard DMRG calculations for the $N = 18$, $s = 5/2$ spin ring (see Eq. (5.31)). We have set $D = 0$ in all cases. We have kept up to 3000 density matrix eigenstates for the $J_1 = J_2$ model and up to 1200 for the $J_1 \neq J_2$ models. The truncated weights are smaller than 10^{-8}.

In both cases, the local responses strongly depend on the position of the spin, i.e., whether the spin has two J_1 couplings ("symmetric position") or a J_1 and a J_2 coupling ("asymmetric position"), cf. Fig 5.17. For the model with $J_1 = 2.88$ meV and $J_2 = 1.02$ meV, the magnetic field leads (for $B < 75$ T) to a "up-up-down" magnetization profile, i.e., a kind of staggered magnetization profile. For the other model, the local magnetizations point all in the same direction, but also with a position dependence. To summarize, the local and total responses to an external magnetic field lead to some interesting results. While the total magnetization shows differences only for very high fields, the local responses are already very different for small fields for the three models considered here. Measuring the local magnetization of the Fe_{18} molecule could thus further support our conclusion (which was mainly based on the analysis of the high-energy INS data) that the model with $J_1 = 2.88$ meV and $J_2 = 1.02$ meV is best suited for this system. However, we have not considered the anisotropy in this subsection. A finite anisotropy could slightly affect the local magnetizations.

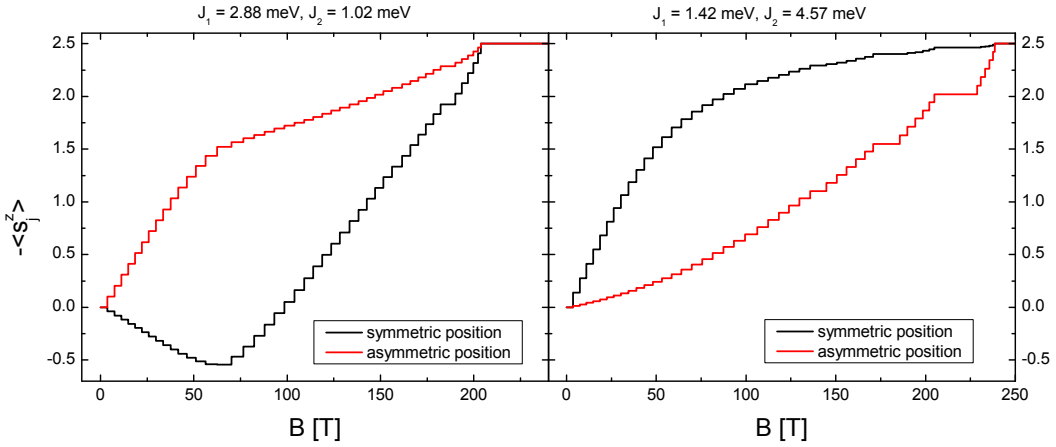

Figure 5.21.: Dependence of the z-component of the local magnetization (which is proportional to $-\langle s_j^z \rangle$) for two different parameter sets as a function of an external magnetic field $\vec{B} = B\vec{e}_z$. The results were obtained using standard DMRG for $D = 0$ and $T = 0$. The result for the uniform model is not shown because for this model the local moments are simply proportional to the magnetization curve presented in Fig. 5.20. "Symmetric position" denotes the local magnetization for a spin between two J_1 couplings. Accordingly, "asymmetric position" denotes a spin position between a J_1 and a J_2 coupling.

6. Summary and conclusion

The aim of this work was to apply standard and dynamical DMRG to very large magnetic molecules which are too large to be treated with exact diagonalization methods such as the Lanczos algorithm. Implementing the DMRG and DDMRG programs is conceptually and technically very involved, and consequently, a large part of this thesis (chapter 3) deals with the description of the algorithm and the application to some test systems for which analytical or numerically exact results are available.

We have then applied DMRG and DDMRG to some very large antiferromagnetic molecules: icosidodecahedral molecules ($N = 30$) with single spin quantum numbers up to $s = 5/2$ ($Mo_{72}Fe_{30}$, Hilbert space dimension of the order of 10^{23}), and the ferric wheel Fe_{18} ($N = 18$, $s = 5/2$, Hilbert space dimension of the order of 10^{14}). These calculations are the most advanced of its kind for magnetic molecules and yield low-energy results with unprecedented accuracy for these systems.

For the icosidodecahedral systems (see chapter 4), we have calculated the energies $E_{\min}(M)$ and zero-temperature magnetization curves for several single-spin quantum numbers s with DMRG. We have modeled the systems using a Heisenberg model with one exchange constant. The comparison with the predictions of the rotational band model shows that the minimal energies in the subspaces of total magnetic quantum number M are rather well described by this model. However, the magnetization curves have features (plateaus and jumps) that cannot be explained by this simple model. Moreover, we have shown that the magnetization plateau, which is a characteristic feature of geometrically frustrated systems, seems to be very robust as a function of s and is still clearly visible for the $s = 5/2$ system. It is evident that the DMRG technique is at its limits for this system and does not deliver quasi-exact results. The truncated weights are very large and also the convergence behavior for increasing m values indicates that it is extremely difficult to obtain accurate and converged results. However, the comparison with previous results for the $s = 5/2$ system obtained by DMRG [121] and so-called correlator product states [170] shows that our DMRG results are more accurate than the other available numerical results.

Using DDMRG, we have furthermore calculated the dynamical correlation function $S^z_j(\omega)$ for the $s = 1/2$ icosidodecahedron. The function displays a rather sharp peak, but exhibits apart from that no clear features and only a very broad excitation spectrum. This behavior is different from the predictions of the rotational band approximation. The calculation of dynamical correlation functions for systems

with $s > 1/2$ was not possible with the program that was developed for this thesis. To this end, further optimizations (e.g., improved parallelization) of the extremely time-consuming calculations would be needed.

In chapter 5 we have presented our DMRG and DDMRG results for the ring-like molecule Fe_{18} which consists of $N = 18$ spins with $s = 5/2$. This molecule was investigated earlier by O. Waldmann et al. in 2009 [10], but the theoretical analysis relied on an effective two-spin Hamiltonian that is related to the rotational band approximation. In contrast, we have performed our calculations for the full 18-spin Hamiltonian. As a first step, we have tested the accuracy of the rotational band approximation as well as some simple spin-wave theory results for uniform antiferromagnetic spin rings as a function of s and the number of spins N. The investigations show that the rotational band approximation becomes more accurate for larger s and smaller N, and that the $s = 5/2$, $N = 18$ uniform spin ring can be well described by a combination of the rotational band approximation with spin-wave theory [25]. This is in accordance with earlier findings on smaller spin rings [37,192].

In chapter 5 we have furthermore simulated the results of recent high-energy INS measurements on Fe_{18} [25, 193]. The experimental INS results show several cold magnetic transitions, i.e., excitations from the ground state. The DDMRG technique was used for the simulation of INS spectra. It turns out that a simple uniform Heisenberg model with only one coupling constant J cannot properly describe the experimental data so that the use of a more general model with two different coupling constants was necessary. Using this so-called "two-J" model, it was possible to fit the high-energy INS data very well. We have used the results of spin-wave theory calculations [25] as an input for our search of the optimal parameters. Whereas spin-wave theory predicts two equally good parameter sets, our DDMRG calculations reveal significant differences for the INS intensities between the two possible parameter sets, with one parameter set leading to better results than the other. Furthermore, the influence and magnitude of the single-ion anisotropy were investigated, and we have found a single set of parameters that describes all experimental data very well. Lastly, we have calculated and compared local (i.e., for a specific spin) and total $T = 0$ magnetization curves for some parameter sets, including our best-fit result of the high-energy INS results. The magnetization curves display interesting features such as magnetization plateaus and an "up-up-down" local magnetization profile for one parameter set.

In conclusion, our results show that DMRG is a very powerful numerical method for the investigation of very large magnetic molecules. It allows to calculate energy spectra, dynamical correlation functions, and magnetization curves of giant magnetic molecules and thus to gain insight that is not accessible by methods such as exact diagonalization which are typically applied to magnetic molecules.

A. Appendix

A.1. Supplement to chapter 2

Here we show how to evaluate the matrix elements $\langle S_A S_B S M | s_j^z | S'_A S'_B S' M' \rangle$ which are needed for the calculation of the dynamical correlation function $S_j^z(\omega)$ in the rotational band approximation (see Chap. 2.3.2). This calculation is rather straightforward with the help of irreducible tensor operators and the Wigner-Eckart theorem. The components of a spin operator $\vec{s}$ and an irreducible tensor operator $\mathbf{s}_q^{(1)}$ of rank 1 are related via [203]

$$\mathbf{s}_0^{(1)} = s^z \,, \quad \mathbf{s}_{\pm 1}^{(1)} \mp \sqrt{\frac{1}{2}} (s^x \pm i s^y) \,. \tag{A.1}$$

In the rotational band approximation (which is exact for the Heisenberg square) the ground state has $S = 0$ and $S_A = S_B = Ns/2$. N denotes the number of spins which is assumed to be even. Only two different transitions (apart from degeneracies) from the $S = 0$ ground state contribute to the dynamical correlation function in the rotational band approximation [37, 42]:

1. $\Delta S = 1$, $\Delta S_A = \Delta S_B = 0$ (within the first rotational band)
2. $\Delta S = 1$, $\Delta S_A = 0$ and $\Delta S_B = -1$, or $\Delta S_A = -1$ and $\Delta S_B = 0$.

The weight of the first transition can easily be calculated. The weight of the other transitions can then be calculated with the help of the sum rule. For the first transitions we need to calculate

$$\langle S_A = \frac{Ns}{2}, S_B = \frac{Ns}{2}, S = 1, M = 0 | \mathbf{s}_0^{(1)}(j) | S'_A = \frac{Ns}{2}, S'_B = \frac{Ns}{2}, S' = 0, M' = 0 \rangle \,, \tag{A.2}$$

with $\mathbf{s}_0^{(1)}(j) \equiv s_j^z$. Since $\mathcal{T}^2 | \frac{Ns}{2} \frac{Ns}{2} SM \rangle = | \frac{Ns}{2} \frac{Ns}{2} SM \rangle$ [37] and $\mathcal{T}^2 \mathbf{s}_0^{(1)}(j) = \mathbf{s}_0^{(1)}(j-2)\mathcal{T}^2$ ($\mathcal{T}$ is the shift operator), we can conclude that

$$\langle SM | \mathbf{s}_0^{(1)}(j) | S'M' \rangle = \langle SM | \mathbf{s}_0^{(1)}(j+2) | S'M' \rangle \,. \tag{A.3}$$

We have omitted the intermediate quantum numbers $S_A = Ns/2$ and $S_B = Ns/2$ here. We now define $\mathbf{s}_0^{(1)}(A) \equiv \sum_{\text{even } j} \mathbf{s}_0^{(1)}(j)$ and $\mathbf{s}_0^{(1)}(B) \equiv \sum_{\text{odd } j} \mathbf{s}_0^{(1)}(j)$. If

the sublattice spins are in each case coupled to there maximum value $Ns/2$ (i.e., $S_A = S_B = Ns/2$), $\mathbf{s}_0^{(1)}(A)$ and $\mathbf{s}_0^{(1)}(B)$ are simply spin-$Ns/2$ operators, so that

$$\langle SM|\mathbf{s}_0^{(1)}(j)|S'M'\rangle = \frac{2}{N}\langle SM|\mathbf{s}_0^{(1)}(A)|S'M'\rangle \text{ (even } j) \tag{A.4}$$

and

$$\langle SM|\mathbf{s}_0^{(1)}(j)|S'M'\rangle = \frac{2}{N}\langle SM|\mathbf{s}_0^{(1)}(B)|S'M'\rangle \text{ (odd } j) \tag{A.5}$$

are simply the transition matrix elements for a dimer. Using the Wigner-Eckart theorem, we can at first "eliminate" the magnetic quantum number [73]:

$$\langle SM|\mathbf{s}_0^1(j)|S'M'\rangle = (-1)^{S-M}\begin{pmatrix} S & 1 & S' \\ -M & 0 & M' \end{pmatrix}\langle S||\mathbf{s}^1(i)||S'\rangle\,. \tag{A.6}$$

Here, $\langle S||\mathbf{s}^1(j)||S'\rangle$ is the reduced matrix element, and $\begin{pmatrix} S & 1 & S' \\ -M & 0 & M' \end{pmatrix}$ a $3j$-symbol. For $S = 1$, $S' = M = M' = 0$, the value of the prefactor is

$$(-1)^{1-0}\begin{pmatrix} 1 & 1 & 0 \\ 0 & 0 & 0 \end{pmatrix} = \frac{1}{\sqrt{3}}\,. \tag{A.7}$$

The result for the reduced matrix element can be found in textbooks, e.g., Ref. [73]:

$$\begin{aligned}\langle S||\mathbf{s}^1(A)||S'\rangle &= (-1)^{Ns+S'+1}\sqrt{(2S+1)(2S'+1)}\sqrt{\frac{Ns}{2}\left(\frac{Ns}{2}+1\right)} \\ &\quad\times\begin{Bmatrix} S & S' & 1 \\ \frac{Ns}{2} & \frac{Ns}{2} & \frac{Ns}{2} \end{Bmatrix}, \end{aligned}\tag{A.8}$$

$$\langle S||\mathbf{s}^1(B)||S'\rangle = (-1)^{S'-S}\langle S||\mathbf{s}^1(A)||S'\rangle\,. \tag{A.9}$$

Here, $\begin{Bmatrix} S & S' & 1 \\ \frac{Ns}{2} & \frac{Ns}{2} & \frac{Ns}{2} \end{Bmatrix}$ denotes a $6j$-symbol. For $S = 1$, $S' = 0$ we get the following results:

$$\begin{aligned}\langle 1||\mathbf{s}^1(A)||0\rangle &= \frac{1}{2}\sqrt{Ns(Ns+1)}\,, \\ \langle 1||\mathbf{s}^1(B)||0\rangle &= -\frac{1}{2}\sqrt{Ns(Ns+1)}\,,\end{aligned}\tag{A.10}$$

so that we can conclude:

$$|\langle Ns/2, Ns/2, S=1, M=0|s_j^z|Ns/2, Ns/2, S'=0, M'=0\rangle|^2 = \frac{1}{3}s\left(s+\frac{2}{N}\right), \tag{A.11}$$

which is, as it should be, independent of j.

A.2. Supplement to chapter 5

The following plots display the functions $S^{zz}(Q,\omega)$ (see Eq. (2.35)) for the "two-J" Hamiltonian (5.31) which was used to model the magnetic properties of the molecule Fe_{18}. The results were obtained using DDMRG (with $m = 600$ kept density matrix eigenstates and $\eta = 0.5$ meV), and two different parameter sets are shown. These data were used for calculation of the INS intensities, see Fig. 5.18.

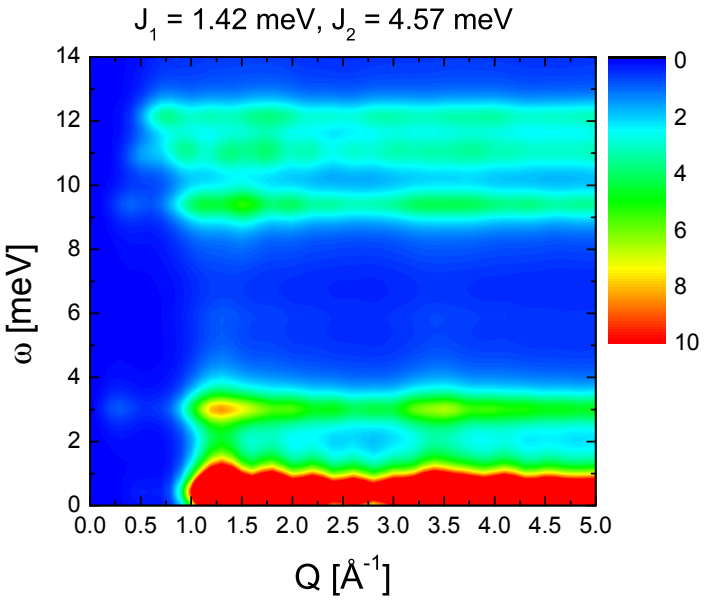

Figure A.1.: $S^{zz}(Q,\omega)$ for the "two-J" Hamiltonian (5.31) as obtained using DDMRG for the parameters $J_1 = 1.42$ meV, $J_2 = 4.57$ meV.

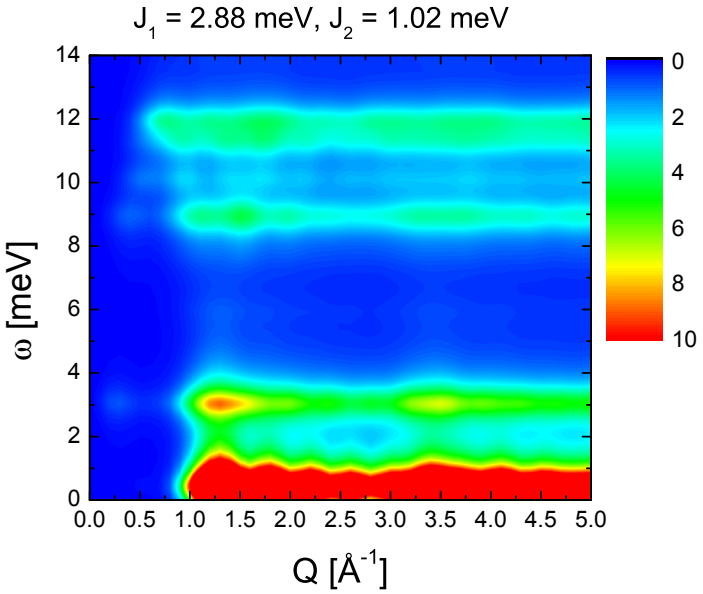

Figure A.2.: $S^{zz}(Q,\omega)$ for the "two-J" Hamiltonian (5.31) as obtained using DDMRG for the parameters $J_1 = 2.88$ meV, $J_2 = 1.02$ meV.

Bibliography

[1] R. Sessoli, D. Gatteschi, A. Caneschi, and Novak M. A. Magnetic bistability in a metal-ion cluster. *Nature*, 365:141, 1993.

[2] D. Gatteschi, A. Cornia, M. Mannini, and R. Sessoli. Organizing and Addressing Magnetic Molecules. *Inorg. Chem.*, 48:3408, 2009.

[3] D. Gatteschi, R. Sessoli, and J. Villain. *Molecular Nanomagnets*. Oxford University Press, Oxford, 2011.

[4] A. Müller, M. Luban, C. Schröder, R. Modler, P. Kögerler, M. Axenovich, J. Schnack, P. Canfield, S. Bud'ko, and N. Harrison. Classical and Quantum Magnetism in Giant Keplerate Magnetic Molecules. *ChemPhysChem*, 2:517, 2001.

[5] S. R. White. Density matrix formulation for quantum renormalization groups. *Phys. Rev. Lett.*, 69:2863, 1992.

[6] U. Schollwöck. The density-matrix renormalization group. *Rev. Mod. Phys.*, 77:259, 2005.

[7] T. D. Kühner and S. R. White. Dynamical correlation functions using the density matrix renormalization group. *Phys. Rev. B*, 60:335, 1999.

[8] E. Jeckelmann. Dynamical density-matrix renormalization-group method. *Phys. Rev. B*, 66:045114, 2002.

[9] P. King, T. C. Stamatatos, K. A. Abboud, and G. Christou. Reversible Size Modification of Iron and Gallium Molecular Wheels: A Ga_{10} "Gallic Wheel" and Large Ga_{18} and Fe_{18} Wheels. *Angew. Chem. Int. Ed.*, 45:7379, 2006.

[10] O. Waldmann, T. C. Stamatatos, G. Christou, H. U. Güdel, I. Sheikin, and H. Mutka. Quantum Phase Interference and Néel-Vector Tunneling in Antiferromagnetic Molecular Wheels. *Phys. Rev. Lett.*, 102:157202, 2009.

[11] O. Cépas and T. Ziman. Modified Spin-Wave Theory for Nanomagnets: Application to the Keplerate Molecule $Mo_{72}Fe_{30}$. *Prog. Theor. Phys. Suppl.*, 159:280, 2005.

[12] O. Waldmann. E-band excitations in the magnetic Keplerate molecule Fe_{30}. *Phys. Rev. B*, 75:012415, 2007.

[13] C. Schröder, H. Nojiri, J. Schnack, P. Hage, M. Luban, and P. Kögerler. Competing Spin Phases in Geometrically Frustrated Magnetic Molecules. *Phys. Rev. Lett.*, 94:017205, 2005.

[14] C. Schröder, R. Prozorov, P. Kögerler, M. D. Vannette, X. Fang, M. Luban, A. Matsuo, K. Kindo, A. Müller, and A. M. Todea. Multiple nearest-neighbor exchange model for the frustrated magnetic molecules $\{Mo_{72}Fe_{30}\}$ and $\{Mo_{72}Cr_{30}\}$. *Phys. Rev. B*, 77:224409, 2008.

[15] A. M. Todea, A. Merca, H. Bögge, T. Glaser, J. M. Pigga, M. L. K. Langston, T. Liu, R. Prozorov, Marshall Luban, C. Schröder, William. H. Casey, and A. Müller. Porous Capsules $\{(M)M_5\}_{12}Fe^{III}_{30}$ ($M = Mo^{VI}$, W^{VI}): Sphere Surface Supramolecular Chemistry with 20 Ammonium Ions, Related Solution Properties, and Tuning of Magnetic Exchange Interactions. *Angew. Chem. Int. Ed.*, 49:514, 2010.

[16] J. Schnack, M. Luban, and R. Modler. Quantum rotational band model for the Heisenberg molecular magnet $\{Mo_{72}Fe_{30}\}$. *EPL (Europhysics Letters)*, 56:863, 2001.

[17] V. O. Garlea, S. E. Nagler, J. L. Zarestky, C. Stassis, D. Vaknin, P. Kögerler, D. F. McMorrow, C. Niedermayer, D. A. Tennant, B. Lake, Y. Qiu, M. Exler, J. Schnack, and M. Luban. Probing spin frustration in high-symmetry magnetic nanomolecules by inelastic neutron scattering. *Phys. Rev. B*, 73:024414, 2006.

[18] Z.-D. Fu, P. Kögerler, U. Rücker, Y. Su, R. Mittal, and T. Brückel. An approach to the magnetic ground state of the molecular magnet $Mo_{72}Fe_{30}$. *New J. Phys.*, 12:083044, 2010.

[19] R. Schmidt, J. Richter, and J. Schnack. Frustration effects in magnetic molecules. *J. Magn. Magn. Mater.*, 295:164, 2005.

[20] I. Rousochatzakis, A. M. Läuchli, and F. Mila. Highly frustrated magnetic clusters: The kagomé on a sphere. *Phys. Rev. B*, 77:094420, 2008.

[21] N. Kunisada, S. Takemura, and Y. Fukumoto. Theoretical study of quantum spin icosidodecahedron ($S = 1/2$) with next-nearest neighbor interactions and analysis of experimental susceptibility for $Mo_{72}V_{30}$. *J. Phys.: Conf. Ser.*, 145:012083, 2009.

[22] J. Schnack and O. Wendland. Properties of highly frustrated magnetic molecules studied by the finite-temperature Lanczos method. *Eur. Phys. J. B*, 78:535, 2010.

[23] A. M. Todea, A. Merca, Hartmut Bögge, J. van Slageren, M. Dressel, L. Engelhardt, M. Luban, T. Glaser, M. Henry, and A. Müller. Extending the $\{(Mo)Mo_5\}_{12}M_{30}$ Capsule Keplerate Sequence: A $\{Cr_{30}\}$ Cluster of $S = 3/2$ Metal Centers with a $\{Na(H_2O)_{12}\}$ Encapsulate. *Angew. Chem. Int. Ed.*, 46:6106, 2007.

[24] A. M. Todea, A. Merca, H. Boegge, T. Glaser, L. Engelhardt, R. Prozorov, M. Luban, and A. Müller. Polyoxotungstates now also with pentagonal units: supramoleuclar chemistry and tuning of magnetic exchange in $\{(M)M_5\}_{12}V_{30}$ Keplerates (M = Mo, W). *Chem. Commun.*, 40:3351, 2009.

[25] J. Ummethum, J. Nehrkorn, S. Mukherjee, N. B. Ivanov, S. Stuiber, Th. Strässle, P. L. W. Tregenna-Pigott, H. Mutka, G. Christou, O. Waldmann, and J. Schnack. Discrete antiferromagnetic spin-wave excitations in the giant ferric wheel Fe_{18}. submitted to Phys. Rev. B, see also arXiv:cond-mat/1206.6203, 2012.

[26] J. Schnack. Effects of frustration on magnetic molecules: a survey from Olivier Kahn until today. *Dalton Trans.*, 39:4677, 2010.

[27] A. J. Tasiopoulos, A. Vinslava, W. Wernsdorfer, K. A. Abboud, and G. Christou. Giant Single-Molecule Magnets: A Mn_{84} Torus and Its Supramolecular Nanotubes. *Angew. Chem. Int. Ed.*, 43:2117, 2004.

[28] J. Schnack. Molecular magnetism. In U. Schollwöck, J. Richter, D. J. J. Farnell, and R. F. Bishop, editors, *Quantum Magnetism*, volume 645 of *Lecture Notes in Physics*. Springer-Verlag, Berlin, Heidelberg, 2004.

[29] A. K. Boudalis, J.-M. Clemente-Juan, F. Dahan, and J.-P. Tuchagues. New Poly-Iron(II) Complexes of N_4O Dinucleating Schiff Bases and Pseudohalides: Syntheses, Structures, and Magnetic and Mössbauer Properties. *Inorg. Chem.*, 43:1574, 2004.

[30] K. L. Taft, C. D. Delfs, G. C. Papaefthymiou, S. Foner, D. Gatteschi, and S. J. Lippard. $[Fe(OMe)_2(O_2CCH_2Cl)]_{10}$, a Molecular Ferric Wheel. *J. Am. Chem. Soc.*, 116:823, 1994.

[31] J. Schnack, M. Brüger, M. Luban, P. Kögerler, E. Morosan, R. Fuchs, R. Modler, H. Nojiri, R. C. Rai, J. Cao, J. L. Musfeldt, and X. Wei. Observation of field-dependent magnetic parameters in the magnetic molecule Ni_4Mo_{12}. *Phys. Rev. B*, 73:094401, 2006.

[32] D. Gatteschi and R. Sessoli. Quantum Tunneling of Magnetization and Related Phenomena in Molecular Materials. *Angew. Chem. Int. Ed.*, 42:268, 2003.

[33] W. Wernsdorfer, N. E. Chakov, and G. Christou. Quantum Phase Interference and Spin-Parity in Mn_{12} Single-Molecule Magnets. *Phys. Rev. Lett.*, 95:037203, 2005.

[34] M. N. Leuenberger and D. Loss. Quantum computing in molecular magnets. *Nature*, 410:789, 2001.

[35] M. Affronte, A. Ghirri, S. Carretta, G. Amoretti, S. Piligkos, G. A. Timco, and R. E. P. Winpenny. Engineering molecular rings for magnetocaloric effect. *Appl. Phys. Lett.*, 84:3468, 2004.

[36] J. Schnack, R. Schmidt, and J. Richter. Enhanced magnetocaloric effect in frustrated magnetic molecules with icosahedral symmetry. *Phys. Rev. B*, 76:054413, 2007.

[37] O. Waldmann. Spin dynamics of finite antiferromagnetic Heisenberg spin rings. *Phys. Rev. B*, 65:024424, 2001.

[38] O. Waldmann, T. Guidi, S. Carretta, C. Mondelli, and A. L. Dearden. Elementary Excitations in the Cyclic Molecular Nanomagnet Cr_8. *Phys. Rev. Lett.*, 91:237202, 2003.

[39] O. Waldmann. Magnetic molecular wheels and grids – the need for novel concepts in "zero-dimensional" magnetism. *Coord. Chem. Rev.*, 249:2550, 2005.

[40] R. Boča. *Theoretical Foundations of Molecular Magnetism*. Elsevier, Amsterdam, 1999.

[41] R. Schnalle. *Symmetry assisted exact and approximate determination of the energy spectra of magnetic molecules using irreducible tensor operators*. PhD thesis, Universität Osnabrück, 2009.

[42] H. U. Güdel, U. Hauser, and A. Furrer. Electronic Ground-State Properties of Tetranuclear Hexa-μ-hydroxo-bis(tetraamminechromium(III))bis(diamminechromium(III)) Chloride. A Spectroscopic and Magnetochemical Study. *Inorg. Chem.*, 18:2730, 1979.

[43] E. Ruiz, A. Rodríguez-Fortea, J. Cano, S. Alvarez, and P. Alemany. About the calculation of exchange coupling constants in polynuclear transition metal complexes. *Journal of Computational Chemistry*, 24:982, 2003.

[44] F. Neese. Importance of Direct Spin-Spin Coupling and Spin-Flip Excitations for the Zero-Field Splittings of Transition Metal Complexes: A Case Study. *J. Am. Chem. Soc.*, 128:10213, 2006.

[45] O. Ciftja, M. Luban, M. Auslender, and J. H. Luscombe. Equation of state and spin-correlation functions of ultrasmall classical Heisenberg magnets. *Phys. Rev. B*, 60:10122, 1999.

[46] L. Engelhardt, M. Luban, and C. Schröder. Finite quantum Heisenberg spin models and their approach to the classical limit. *Phys. Rev. B*, 74:054413, 2006.

[47] D. Mentrup, J. Schnack, and M. Luban. Spin dynamics of quantum and classical Heisenberg dimers. *Physica A*, 272:153, 1999.

[48] J. Richter, J. Schulenburg, and A. Honecker. Quantum magnetism in two dimensions: From semi-classical néel order to magnetic disorder. In U. Schollwöck, J. Richter, D. J. J. Farnell, and R. F. Bishop, editors, *Quantum Magnetism*, volume 645 of *Lecture Notes in Physics*, pages 85–153. Springer, Berlin, Heidelberg, 2004.

[49] J. T. Chalker. Geometrically Frustrated Antiferromagnets: Statistical Mechanics and Dynamics. In C. Lacroix, P. Mendels, and F. Mila, editors, *Introduction to Frustrated Magnetism*, volume 164 of *Springer Series in Solid-State Sciences*, pages 3–22. Springer, Berlin, Heidelberg, 2011.

[50] L. E. Ballentine. *Quantum Mechanics – A Modern Development*. World Scientific Publishing, Singapore, 2006.

[51] R. Schnalle and J. Schnack. Calculating the energy spectra of magnetic molecules: application of real- and spin-space symmetries. *Int. Rev. Phys. Chem.*, 29:403, 2010.

[52] E. Lieb and D. Mattis. Ordering Energy Levels of Interacting Spin Systems. *J. Math. Phys.*, 3:749, 1962.

[53] I. P. McCulloch and M. Gulácsi. The non-Abelian density matrix renormalization group algorithm. *EPL (Europhysics Letters)*, 57:852, 2002.

[54] G. Alvarez. Implementation of the SU(2) Hamiltonian Symmetry for the DMRG Algorithm. *Comp. Phys. Comm.*, 183:2226, 2012. see also arXiv:cond-mat/1003.1919v1.

[55] A. M. Läuchli. Numerical simulations of frustrated systems. In C. Lacroix, P. Mendels, and F. Mila, editors, *Introduction to Frustrated Magnetism*, volume 164 of *Springer Series in Solid-State Sciences*, pages 481–511. Springer, Berlin, Heidelberg, 2011.

[56] O. Derzhko, A. Honecker, and J. Richter. Low-temperature thermodynamics for a flat-band ferromagnet: Rigorous versus numerical results. *Phys. Rev. B*, 76:220402, 2007.

[57] A. W. Sandvik. Computational studies of quantum spin systems. *AIP Conf. Proc.*, 1297:135, 2010.

[58] A. W. Sandvik and O. F. Syljuåsen. The Directed-Loop Algorithm. *AIP Conf. Proc.*, 690:299, 2003.

[59] A. Müller, A. M. Todea, J. van Slageren, M. Dressel, H. Bögge, M. Schmidtmann, M. Luban, L. Engelhardt, and M. Rusu. Triangular Geometrical and Magnetic Motifs Uniquely Linked on a Spherical Capsule Surface. *Angew. Chem. Int. Ed.*, 44:3857, 2005.

[60] B. Bernu, C. Lhuillier, and L. Pierre. Signature of Néel order in exact spectra of quantum antiferromagnets on finite lattices. *Phys. Rev. Lett.*, 69:2590, 1992.

[61] B. Bernu, P. Lecheminant, C. Lhuillier, and L. Pierre. Exact spectra, spin susceptibilities, and order parameter of the quantum Heisenberg antiferromagnet on the triangular lattice. *Phys. Rev. B*, 50:10048, 1994.

[62] J. Richter, N. B. Ivanov, A. Voigt, and K. Retzlaff. Ground-state phase relationships and level ordering for frustrated quantum antiferromagnets. *J. Low Temp. Phys.*, 99:363, 1995.

[63] A. Caneschi, A. Cornia, A. C. Fabretti, S. Foner, D. Gatteschi, R. Grandi, and L. Schenetti. Synthesis, Crystal Structure, Magnetism, and Magnetic Anisotropy of Cyclic Clusters Comprising six Iron(III) Ions and Entrapping Alkaline Ions. *Chem. Eur. J.*, 2:1379, 1996.

[64] J. Schnack and M. Luban. Rotational modes in molecular magnets with antiferromagnetic Heisenberg exchange. *Phys. Rev. B*, 63:014418, 2000.

[65] P. Sindzingre and C. Lhuillier. Low-energy excitations of the kagomé antiferromagnet and the spin-gap issue. *EPL (Europhysics Letters)*, 88:27009, 2009.

[66] H.-J. Schmidt and M. Luban. Classical ground states of symmetric Heisenberg spin systems. *J. Phys. A: Math. Gen.*, 36:6351, 2003.

[67] G. L. Abbati, A. Caneschi, A. Cornia, A. C. Fabretti, and D. Gatteschi. $[Fe(OCH_3)_2(dbm)]_{12}$: synthesis, solid-state characterization and reactivity of a new molecular ferric wheel. *Inorganica Chimica Acta*, 297:291, 2000.

[68] O. Waldmann. Quantum tunneling in molecular ferric wheels. *EPL (Europhysics Letters)*, 60:302, 2003.

[69] K. Bärwinkel, H.-J. Schmidt, and J. Schnack. Structure and relevant dimension of the Heisenberg model and applications to spin rings. *J. Magn. Magn. Mater.*, 212:240, 2000.

[70] K. Bärwinkel, P. Hage, H.-J. Schmidt, and J. Schnack. Quantum numbers for relative ground states of antiferromagnetic Heisenberg spin rings. *Phys. Rev. B*, 68:054422, 2003.

[71] T. Mayer-Kuckuck. *Atomphysik*. Teubner, Stuttgart, 1997.

[72] J. Schnack. private communication, 2012.

[73] A. Furrer, J. Mesot, and T. Strässle. *Neutron Scattering in Condensed Matter Physics*, volume 4 of *Series on Neutron Techniques and Applications*. World Scientific, Singapore, 2009.

[74] G. L. Squires. *Introduction to the Theory of Thermal Neutron Scattering*. Cambridge University Press, Cambridge, 1978.

[75] G. Müller, H. Thomas, H. Beck, and J. C. Bonner. Quantum spin dynamics of the antiferromagnetic linear chain in zero and nonzero magnetic field. *Phys. Rev. B*, 24:1429, 1981.

[76] O. Waldmann. Q dependence of the inelastic neutron scattering cross section for molecular spin clusters with high molecular symmetry. *Phys. Rev. B*, 68:174406, 2003.

[77] C. Broholm, G. Aeppli, G. P. Espinosa, and A. S. Cooper. Antiferromagnetic fluctuations and short-range order in a Kagomé lattice. *Phys. Rev. Lett.*, 65:3173, 1990.

[78] O. Waldmann and H. U. Güdel. Many-spin effects in inelastic neutron scattering and electron paramagnetic resonance of molecular nanomagnets. *Phys. Rev. B*, 72:094422, 2005.

[79] O. Waldmann. private communication, 2011.

[80] J. Nehrkorn. private communication, 2011.

[81] K. G. Wilson. The renormalization group: Critical phenomena and the Kondo problem. *Rev. Mod. Phys.*, 47:773, 1975.

[82] R. Bulla, T. A. Costi, and T. Pruschke. Numerical renormalization group method for quantum impurity systems. *Rev. Mod. Phys.*, 80:395, 2008.

[83] S. R. White and R. M. Noack. Real-space quantum renormalization groups. *Phys. Rev. Lett.*, 68:3487, 1992.

[84] I. Peschel, X. Wang, M. Kaulke, and K. Hallberg, editors. *Density-Matrix Renormalization - A New Numerical Method in Physics*, volume 528 of *Lecture Notes in Physics*. Springer-Verlag Berlin Heidelberg, 1999.

[85] M. Troyer and U.-J. Wiese. Computational Complexity and Fundamental Limitations to Fermionic Quantum Monte Carlo Simulations. *Phys. Rev. Lett.*, 94:170201, 2005.

[86] S. R. White. Density-matrix algorithms for quantum renormalization groups. *Phys. Rev. B*, 48:10345, 1993.

[87] H.-P. Breuer and F. Petruccione. *The Theory of Open Quantum Systems*. Oxford University Press, Oxford, 2007.

[88] K. Blum. *Density Matrix Theory and Applications*. Plenum Press, New York, 1981.

[89] Ö. Legeza and G. Fáth. Accuracy of the density-matrix renormalization-group method. *Phys. Rev. B*, 53:14349, 1996.

[90] M. A. Nielsen and I. L. Chuang. *Quantum Computation and Quantum Information*. Cambridge University Press, Cambridge, 2000.

[91] Ph. Blanchard and E. Brüning. Remarks on the structure of states of composite quantum systems and envariance. *Phys. Lett. A*, 355:180, 2006.

[92] C. H. Bennett, D. P. DiVincenzo, J. A. Smolin, and W. K. Wootters. Mixed-state entanglement and quantum error correction. *Phys. Rev. A*, 54:3824, 1996.

[93] P. Schmitteckert and G. Schneider. Signal transport and finite bias conductance in and through correlated nanostructures. In W. E. Nagel, W. Jäger, and M. Resch, editors, *High Performance Computing in Science and Engineering '06*, pages 113–126. Springer, Berlin, Heidelberg, 2007.

[94] Ö. Legeza, , Noack R. M., J. Sólyom, and L. Tincani. Applications of Quantum Information in the Density-Matrix Renormalization Group. In H. Fehske, R. Schneider, and A. Weiße, editors, *Computational Many-Particle Physics*, volume 739 of *Lect. Notes Phys.*, pages 653–664. Springer-Verlag, Berlin, Heidelberg, 2008.

[95] T. Küchel. *Dynamics of one-dimensional electron systems.* PhD thesis, Karlsruhe Institute of Technology, 2009.

[96] E. Jeckelmann. *Dynamical Density-Matrix Renormalization Group.* Habilitation, Philipps-Universität Marburg, 2003.

[97] J. Dukelsky, M. A. Martín-Delgado, T. Nishino, and G. Sierra. Equivalence of the variational matrix product method and the density matrix renormalization group applied to spin chains. *EPL (Europhysics Letters)*, 43:457, 1998.

[98] S. R. White. Density matrix renormalization group algorithms with a single center site. *Phys. Rev. B*, 72:180403, 2005.

[99] I. P. McCulloch. *Collective Phenomena in Strongly Correlated Electron Systems.* PhD thesis, Australian National University, 2001.

[100] B. Stroustrup. *The C++ Programming Language.* Addison-Wesley, Reading, Massachusetts, 2000.

[101] S. Ramasesha, S. K. Pati, H. R. Krishnamurthy, Z. Shuai, and J. L. Brédas. Symmetrized density-matrix renormalization-group method for excited states of Hubbard models. *Phys. Rev. B*, 54:7598, 1996.

[102] Y. Saad. *Iterative Methods for Sparse Linear Systems.* PWS Publishing Company, Boston, 1996.

[103] J. R. Shewchuck. An Introduction to the Conjugate Gradient Method Without the Agonizing Pain. `http://www.cs.cmu.edu/~quake-papers/painless-conjugate-gradient.pdf`, August 1994.

[104] LAPACK `http://netlib.org/lapack/`.

[105] Reinhard M. Noack and Salvatore R. Manmana. Diagonalization- and numerical renormalization-group-based methods for interacting quantum systems. *AIP Conf. Proc.*, 789:93, 2005.

[106] A. L. Malvezzi. An introduction to numerical methods in low-dimensional quantum systems. *Braz. J. Phys.*, 33:55, 2003.

[107] B. N. Parlett. *The Symmetric Eigenvalue Problem*. Prentice Hall, Inc., Englewood Cliffs, 1980.

[108] A. M. Läuchli, 2009. private communication.

[109] G. Hager, E. Jeckelmann, H. Fehske, and G. Wellein. Parallelization strategies for density matrix renormalization group algorithms on shared-memory systems. *Journal of Computational Physics*, 194:795, 2004.

[110] BLAS `http://netlib.org/blas/`.

[111] Steven R. White. Spin Gaps in a Frustrated Heisenberg Model for CaV_4O_9. *Phys. Rev. Lett.*, 77:3633, 1996.

[112] U. Schollwöck. The density-matrix renormalization group in the age of matrix product states. *Annals of Physics*, 326:96, 2011.

[113] S. Östlund and S. Rommer. Thermodynamic Limit of Density Matrix Renormalization. *Phys. Rev. Lett.*, 75:3537, 1995.

[114] G. K.-L. Chan and M. Head-Gordon. Highly correlated calculations with a polynomial cost algorithm: A study of the density matrix renormalization group. *J. Chem. Phys.*, 116:4462, 2002.

[115] W. Münder, A. Weichselbaum, A. Holzner, J. von Delft, and C. L. Henley. Correlation density matrices for one-dimensional quantum chains based on the density matrix renormalization group. *New J. Phys.*, 12:075027, 2010.

[116] I. P. McCulloch and M. Gulácsi. Comment on "Equivalence of the variational matrix product method and the density matrix renormalization group applied to spin chains" by J. Dukelsky et al. *EPL (Europhysics Letters)*, 61:138, 2003.

[117] J. C. Xavier. A simple way to avoid metastable configurations in the density-matrix renormalization-group algorithms. *Braz. J. Phys.*, 39:596, 2009.

[118] A. Friedrich. *Time-dependent Properties of one-dimensional Spin-Systems: a DMRG-Study*. PhD thesis, Rheinisch-Westfälische Technische Hochschule Aachen, 2006.

[119] A. Friedrich, A. K. Kolezhuk, I. P. McCulloch, and U. Schollwöck. Edge singularities in high-energy spectra of gapped one-dimensional magnets in strong magnetic fields. *Phys. Rev. B*, 75:094414, 2007.

[120] I. P. McCulloch. From density-matrix renormalization group to matrix product states. *J. Stat. Mech.*, 2007:P10014, 2007.

[121] M. Exler and J. Schnack. Evaluation of the low-lying energy spectrum of magnetic Keplerate molecules using the density-matrix renormalization group technique. *Phys. Rev. B*, 67:094440, 2003.

[122] T. Xiang, J. Lou, and Z. Su. Two-dimensional algorithm of the density-matrix renormalization group. *Phys. Rev. B*, 64:104414, 2001.

[123] S. Moukouri and L. G. Caron. Renormalization group method for quasi-one-dimensional quantum hamiltonians. *Phys. Rev. B*, 67:092405, 2003.

[124] D. J. J. Farnell. Density matrix renormalization group calculations for two-dimensional lattices: Application to the spin-half and spin-one square-lattice Heisenberg models. *Phys. Rev. B*, 68:134419, 2003.

[125] A. Weichselbaum and S. R. White. Incommensurate correlations in the anisotropic triangular heisenberg lattice. *Phys. Rev. B*, 84:245130, 2011.

[126] E. M. Stoudenmire and S. R. White. Studying Two-Dimensional Systems with the Density Matrix Renormalization Group. *Ann. Rev. Cond. Mat. Phys.*, 3:111, 2012.

[127] S. Liang and H. Pang. Approximate diagonalization using the density matrix renormalization-group method: A two-dimensional-systems perspective. *Phys. Rev. B*, 49:9214, 1994.

[128] G. Hager, G. Wellein, E. Jeckelmann, and H. Fehske. DMRG Investigation of Stripe Formation in Doped Hubbard Ladders. In S. Wagner, W. Hanke, A. Bode, and F. Durst, editors, *High Performance Computing in Science and Engineering, Munich 2004*, pages 339–361, Berlin, Heidelberg, 2004. Springer.

[129] F. Verstraete and J. I. Cirac. Renormalization algorithms for Quantum-Many Body Systems in two and higher dimensions. arXiv:cond-mat/0407066v1, 2004.

[130] F. Verstraete, D. Porras, and J. I. Cirac. Density matrix renormalization group and periodic boundary conditions: A quantum information perspective. *Phys. Rev. Lett.*, 93:227205, 2004.

[131] H. J. Changlani, J. M. Kinder, C. J. Umrigar, and G. K.-L. Chan. Approximating strongly correlated wave functions with correlator product states. *Phys. Rev. B*, 80:245116, 2009.

[132] F. Mezzacapo, N. Schuch, M. Boninsegni, and J. I. Cirac. Ground-state properties of quantum many-body systems: entangled-plaquette states and variational Monte Carlo. *New J. Phys.*, 11:083026, 2009.

[133] E. R. Gagliano and C. A. Balseiro. Dynamical Properties of Quantum Many-Body Systems at Zero Temperature. *Phys. Rev. Lett.*, 59:2999, 1987.

[134] Karen A. Hallberg. Density-matrix algorithm for the calculation of dynamical properties of low-dimensional systems. *Phys. Rev. B*, 52:R9827, 1995.

[135] S. Ramasesha, S. K. Pati, H. R. Krishnamurthy, Z. Shuai, and J. L. Brédas. Low-lying electronic excitations and nonlinear optic properties of polymers via symmetrized density matrix renormalization group method. *Synth. Met.*, 85:1019, 1997.

[136] I. Schneider, A. Struck, M. Bortz, and S. Eggert. Local Density of States for Individual Energy Levels in Finite Quantum Wires. *Phys. Rev. Lett.*, 101:206401, 2008.

[137] A. Honecker, S. Hu, R. Peters, and J. Richter. Dynamic and thermodynamic properties of the generalized diamond chain model for azurite. *J. Phys.: Condens. Matter*, 23:164211, 2011.

[138] Daoqi Yang. *C++ and Object-oriented Numeric Computing for Scientists and Engineers*. Springer Verlag, New York, Berlin, Heidelberg, 2000.

[139] E. Jeckelmann, F. Gebhard, and F. H. L. Essler. Optical Conductivity of the Half-Filled Hubbard Chain. *Phys. Rev. Lett.*, 85:3910, 2000.

[140] C. Raas. *Dynamic Density-Matrix Renormalization for the Symmetric Single Impurity Anderson Model*. PhD thesis, Universität zu Köln, 2005.

[141] S. Smerat. *Ground state and dynamical properties of the infnite Kondo lattice model and transport through carbon based nanodevices – a numerical study*. PhD thesis, Ludwig-Maximilians-Universität München, 2011.

[142] A. Meister. *Numerik linearer Gleichungssysteme*. Vieweg+Teubner, Wiesbaden, 2011.

[143] F. D. M. Haldane. Continuum dynamics of the 1-D Heisenberg antiferromagnet: Identification with the O(3) nonlinear sigma model. *Phys. Lett. A*, 93:464, 1983.

[144] F. D. M. Haldane. Nonlinear Field Theory of Large-Spin Heisenberg Antiferromagnets: Semiclassically Quantized Solitons of the One-Dimensional Easy-Axis Néel State. *Phys. Rev. Lett.*, 50:1153, 1983.

[145] T. Kennedy. Exact diagonalisations of open spin-1 chains. *J. Phys.: Condens. Matter*, 2:5737, 1990.

[146] S. R. White and D. A. Huse. Numerical renormalization-group study of low-lying eigenstates of the antiferromagnetic S=1 Heisenberg chain. *Phys. Rev. B*, 48:3844, 1993.

[147] T. K. Ng. Schwinger-boson mean-field theory for S=1 open spin chains. *Phys. Rev. B*, 45:8181, 1992.

[148] S. Qin, T.-K. Ng, and Z.-B. Su. Edge states in open antiferromagnetic Heisenberg chains. *Phys. Rev. B*, 52:12844, 1995.

[149] H. Bethe. Zur Theorie der Metalle. *Z. Phys.*, 71:205, 1931.

[150] L. Hulthén. Über das Austauschproblem eines Kristalls. *Ark. Mat. Astron. Fysik*, 26A:1, 1938.

[151] F. Woynarovich and H.-P. Eckle. Finite-size corrections and numerical calculations for long spin-1/2 Heisenberg chains in the critical region. *J. Phys. A: Math. Gen.*, 20:L97, 1987.

[152] I. Affleck, D. Gepner, H. J. Schulz, and T. Ziman. Critical behaviour of spin-s Heisenberg antiferromagnetic chains: analytic and numerical results. *J. Phys. A: Math. Gen.*, 22:511, 1989.

[153] A. Moreo. Ground-state properties of Heisenberg spin chains. *Phys. Rev. B*, 35:8562, 1987.

[154] A. F. Albuquerque, F. Alet, P. Corboz, P. Dayal, A. Feiguin, S. Fuchs, L. Gamper, E. Gull, S. Gürtler, A. Honecker, R. Igarashi, M. Körner, A. Kozhevnikov, A. Läuchli, S. R. Manmana, M. Matsumoto, I. P. McCulloch, F. Michel, R. M. Noack, G. Pawlowski, L. Pollet, T. Pruschke, U. Schollwöck, S. Todo, S. Trebst, M. Troyer, P. Werner, and S. Wessel. The ALPS project release 1.3: Open-source software for strongly correlated systems. *J. Magn. Magn. Mater.*, 310:1187, 2007. (ALPS collaboration) see also `http://alps.comp-phys.org`.

[155] M. Troyer. Are generic parallel algorithms feasible for quantum lattice models? *Lecture Notes in Computer Science*, 1732:164, 1999.

[156] H. Benthien. *Dynamical Properties of Quasi One-Dimensional Correlated Electron Systems*. PhD thesis, Universität Marburg, 2005.

[157] J. Schnack. private communication, 2011.

[158] E. Jeckelmann and H. Benthien. Dynamical density-matrix renormalization group. In H. Fehske, R. Schneider, and A. Weiße, editors, *Computational Many Particle Physics*, volume 739 of *Lecture Notes in Physics*, pages 621–635. Springer, Berlin, Heidelberg, 2008.

[159] Wikipedia, the free encyclopedia. Icosidodecahedron, 2012. `http://en.wikipedia.org/wiki/Icosidodecahedron`.

[160] B. Botar, P. Kögerler, and C. L. Hill. $[\{(Mo)Mo_5O_{21}(H_2O)_3(SO_4)\}_{12}(VO)_{30}(H_2O)_{20}]^{36-}$: A molecular quantum spin icosidodecahedron. *Chem. Commun.*, page 3138, 2005.

[161] M. Axenovich and M. Luban. Exact ground state properties of the classical Heisenberg model for giant magnetic molecules. *Phys. Rev. B*, 63:100407, 2001.

[162] J. K. Jung, D. Procissi, R. Vincent, B. J. Suh, F. Borsa, P. Kögerler, C. Schröder, and M. Luban. Proton NMR in the giant paramagnetic molecule $\{Mo_{72}Fe_{30}\}$. *J. Appl. Phys.*, 91:7388, 2002.

[163] E. Micotti, D. Procissi, A. Lascialfari, P. Carretta, P. Kögerler, F. Borsa, M. Luban, and C. Baines. NMR and μSR investigation of spin dynamics in $\{Mo_{72}Fe_{30}\}$ molecular clusters. *J. Magn. Magn. Mater.*, 272-276, Part 2:1099, 2004.

[164] M. Hasegawa and H. Shiba. Magnetic Frustration and Anisotropy Effects in Giant Magnetic Molecule $Mo_{72}Fe_{30}$. *J. Phys. Soc. Jpn.*, 73:2543, 2004.

[165] J. Lago, E. Micotti, M. Corti, A. Lascialfari, A. Bianchi, S. Carretta, P. Santini, D. Procissi, S. H. Baek, P. Kögerler, C. Baines, and A. Amato. Low-energy spin dynamics in the giant keplerate molecule $\{Mo_{72}Fe_{30}\}$: A muon spin relaxation and ^1H NMR investigation. *Phys. Rev. B*, 76:064432, 2007.

[166] U. Kortz, A. Müller, J. van Slageren, J. Schnack, N. S. Dalal, and M. Dressel. Polyoxometalates: Fascinating structures, unique magnetic properties. *Coord. Chem. Rev.*, 253:2315, 2009.

[167] J. Schnack. Quasi-exact evaluation of the magnetic properties of a giant Keplerate molecule. arXiv:cond-mat/1012.4980v1, 2010.

[168] J. Schnack, H.-J. Schmidt, J. Richter, and J. Schulenburg. Independent magnon states on magnetic polytopes. *Eur. Phys. J. B*, 24:475, 2001.

[169] S. Torbrügge and J. Schnack. Sampling the two-dimensional density of states $g(E, M)$ of a giant magnetic molecule using the Wang-Landau method. *Phys. Rev. B*, 75:054403, 2007.

[170] E. Neuscamman and G. K.-L. Chan. A correlator product state study of molecular magnetism in the giant Keplerate $Mo_{72}Fe_{30}$. arXiv:cond-mat/1203.6883v1, 2012.

[171] J. Schulenburg, A. Honecker, J. Schnack, J. Richter, and H.-J. Schmidt. Macroscopic Magnetization Jumps due to Independent Magnons in Frustrated Quantum Spin Lattices. *Phys. Rev. Lett.*, 88:167207, 2002.

[172] G. Moritz, B. A. Hess, and M. Reiher. Convergence behavior of the density-matrix renormalization group algorithm for optimized orbital orderings. *J. Chem. Phys.*, 122:024107, 2005.

[173] A. O. Mitrushenkov, R. Linguerri, P. Palmieri, and G. Fano. Quantum chemistry using the density matrix renormalization group II. *J. Chem. Phys.*, 119:4148, 2003.

[174] Ö. Legeza and J. Sólyom. Optimizing the density-matrix renormalization group method using quantum information entropy. *Phys. Rev. B*, 68:195116, 2003.

[175] J. Rissler, R. M. Noack, and S. R. White. Measuring orbital interaction using quantum information theory. *Chemical Physics*, 323:519, 2006.

[176] E. Cuthill and J. McKee. Reducing the bandwidth of sparse symmetric matrices. In *Proceedings of the 1969 24th national conference*, ACM '69, pages 157–172, New York, NY, USA, 1969. ACM.

[177] W. M. Chan and A. George. A linear time implementation of the reverse Cuthill-McKee algorithm. *BIT Numerical Mathematics*, 20:8, 1980.

[178] S. W. Sloan. A FORTRAN program for profile and wavefront reduction. *International Journal for Numerical Methods in Engineering*, 28:2651, 1989.

[179] Wolfram Mathematica Documentation Center. Graph utilities package tutorial, 2012. `http://reference.wolfram.com/mathematica/GraphUtilities/tutorial/GraphUtilities.html`.

[180] J. Schnack. private communication, 2010.

[181] A. Läuchli. private communication, 2012.

[182] E. Jeckelmann. private communication, 2010.

[183] R. W. Saalfrank, I. Bernt, E. Uller, and F. Hampel. Template-Mediated Self Assembly of Six- and Eight-Membered Iron Coronates. *Angew. Chem. Int. Ed.*, 36:2482, 1997.

[184] S. P. Watton, P. Fuhrmann, L. E. Pence, S. J. Lippard, A. Caneschi, A. Cornia, and G. L. Abbati. A Cyclic Octadecairon(III) Complex, the Molecular 18-Wheeler. *Angew. Chem. Int. Ed.*, 36:2774, 1997.

[185] D. Gatteschi, A. Caneschi, L. Pardi, and R. Sessoli. Large Clusters of Metal Ions: The Transition from Molecular to Bulk Magnets. *Science*, 265:1054, 1994.

[186] B. Normand, X. Wang, X. Zotos, and Daniel Loss. Magnetization in molecular iron rings. *Phys. Rev. B*, 63:184409, 2001.

[187] A. Honecker, F. Meier, D. Loss, and B. Normand. Spin dynamics and coherent tunnelling in the molecular magnetic rings Fe_6 and Fe_8. *Eur. Phys. J. B*, 27:487, 2002.

[188] S. Carretta, J. van Slageren, T. Guidi, E. Liviotti, C. Mondelli, D. Rovai, A. Cornia, A. L. Dearden, F. Carsughi, M. Affronte, C. D. Frost, R. E. P. Winpenny, D. Gatteschi, G. Amoretti, and R. Caciuffo. Microscopic spin Hamiltonian of a Cr_8 antiferromagnetic ring from inelastic neutron scattering. *Phys. Rev. B*, 67:094405, 2003.

[189] P. Santini, S. Carretta, G. Amoretti, T. Guidi, R. Caciuffo, A. Caneschi, D. Rovai, Y. Qiu, and J. R. D. Copley. Spin dynamics and tunneling of the Néel vector in the Fe_{10} magnetic wheel. *Phys. Rev. B*, 71:184405, 2005.

[190] O. Waldmann, C. Dobe, H. U. Güdel, and H. Mutka. Quantum dynamics of the Néel vector in the antiferromagnetic molecular wheel $CsFe_8$. *Phys. Rev. B*, 74:054429, 2006.

[191] N. P. Konstantinidis, A. Sundt, J. Nehrkorn, A. Machens, and O. Waldmann. Magnetism on a Mesoscopic Scale: Molecular Nanomagnets Bridging Quantum and Classical Physics. *J. Phys.: Conf. Ser.*, 303:012003, 2011.

[192] J. Dreiser, O. Waldmann, C. Dobe, G. Carver, S. T. Ochsenbein, A. Sieber, H. U. Güdel, J. van Duijn, J. Taylor, and A. Podlesnyak. Quantized antiferromagnetic spin waves in the molecular Heisenberg ring $CsFe_8$. *Phys. Rev. B*, 81:024408, 2010.

[193] J. Nehrkorn. private communication, 2012.

[194] P. W. Anderson. An Approximate Quantum Theory of the Antiferromagnetic Ground State. *Phys. Rev.*, 86:694, 1952.

[195] Gerhard Müller. Sum rules in the dynamics of quantum spin chains. *Phys. Rev. B*, 26:1311, 1982.

[196] T. Oguchi. Theory of Spin-Wave Interactions in Ferro- and Antiferromagnetism. *Phys. Rev.*, 117:117, 1960.

[197] N. Ivanov and D. Sen. Spin Wave Analysis of Heisenberg Magnets in Restricted Geometries. In U. Schollwöck, J. Richter, D. J. J. Farnell, and R. Bishop, editors, *Quantum Magnetism*, volume 645 of *Lecture Notes in Physics*, pages 195–226. Springer, Berlin, Heidelberg, 2004.

[198] L. Engelhardt and M. Luban. Low-temperature magnetization and the excitation spectrum of antiferromagnetic Heisenberg spin rings. *Phys. Rev. B*, 73:054430, 2006.

[199] Neutron Spectroscopy Group Paul Scherrer Institute. FOCUS description of the instrument, 2012. `http://spectroscopy.web.psi.ch/focus/focus_description.html`.

[200] S. T. Ochsenbein, F. Tuna, M. Rancan, R. S. G. Davies, C. A. Muryn, O. Waldmann, R. Bircher, A. Sieber, G. Carver, H. Mutka, F. Fernandez-Alonso, A. Podlesnyak, L. P. Engelhardt, G. A. Timco, H. U. Güdel, and R. E. P. Winpenny. Studies of Finite Molecular Chains: Synthesis,Structural, Magnetic and Inelastic Neutron Scattering Studies of Hexa- and Heptanuclear Chromium Horseshoes. *Chem. Eur. J.*, 14:5144, 2008.

[201] A. Honecker, J. Schulenburg, and J. Richter. Magnetization plateaus in frustrated antiferromagnetic quantum spin models. *J. Phys.: Condens. Matter*, 16:S749, 2004.

[202] E. Micotti, Y. Furukawa, K. Kumagai, S. Carretta, A. Lascialfari, F. Borsa, G. A. Timco, and R. E. P. Winpenny. Local spin moment distribution in antiferromagnetic molecular rings probed by NMR. *Phys. Rev. Lett.*, 97:267204, 2006.

[203] B. S. Tsukerblat. *Group Theory in Chemistry and Spectroscopy – A Simple Guide to Advanced Usage*. Dover Publications, Mineola, New York, 2006.

Danksagung

An erster Stelle danke ich Prof. Dr. Jürgen Schnack für die schlichtweg perfekte Betreuung und insbesondere dafür, dass er stets ein offenes Ohr für Fragen hatte.

Prof. Dr. Reimann danke ich dafür, dass er sich bereit erklärt hat, die Arbeit zu begutachten.

Für die sehr gute und ertragreiche Zusammenarbeit zum Thema Fe_{18} möchte ich mich bei Joscha Nehrkorn und Prof. Dr. Oliver Waldmann aus der Arbeitsgruppe "Molecular Nanomagnets" in Freiburg sowie bei Prof. Dr. Nedko Ivanov bedanken. Die vielen Diskussionen haben entscheidend zum Gelingen der Arbeit beigetragen. Weiterhin möchte ich mich bei der gesamten Arbeitsgruppe "Molecular Nanomagnets" für den sehr netten Aufenthalt im schönen Freiburg bedanken.

Für hilfreiche Diskussionen zur DMRG-Technik und zum Ikosidodekaeder danke ich Prof. Dr. Andreas Läuchli, Prof. Dr. Eric Jeckelmann, Peter Schmitteckert, Piet Dargel und Stephan Langer.

Für das gründliche Korrekturlesen der Arbeit und viele wichtige Verbesserungsvorschläge danke ich Martin Höck und Joscha Nehrkorn. Zudem danke ich Sebastian Getfert und Jens Ummethum für das Korrekturlesen von Einleitung und Zusammenfassung.

Christian Karlewski danke ich für das Bereitstellen der Vorlage zu Abbildung 4.1.

Hanne Litschewsky danke ich für die Hilfe in allen organisatorischen Dingen.

Weiterhin danke ich allen Arbeitsgruppenmitgliedern von E5 und insbesondere meinen langjährigen Weggefährten Martin Höck, Sebastian Getfert, Stefan Leiding, Oliver Wendland, Roman Schnalle und Thomas Englisch für die Hilfsbereitschaft und die stets sehr angenehme Atmosphäre.

Zuletzt und im Besonderen danke ich meiner Familie und insbesondere meinen Eltern dafür, dass sie mich stets unterstützt haben.

Erklärung

Hiermit versichere ich, dass ich die vorliegende Arbeit selbstständig und ohne unerlaubte Hilfe erstellt und außer den angegebenen Quellen keine weiteren Hilfsmittel verwendet habe.

Jörg Ummethum